Optimal control simulations of human hand grasping

Optimalsteuerungsimulationen des Greifens der menschlichen Hand

Der Technischen Fakultät der Friedrich-Alexander-Universität Erlangen-Nürnberg

zur

Erlangung des Doktorgrades Dr.-Ing. vorgelegt von

Uday Phutane

aus Mumbai, Indien

Als Dissertation genehmigt von der Technischen Fakultät der Friedrich-Alexander-Universität Erlangen-Nürnberg

Tag der mündlichen Prüfung: 20.11.2023

Gutachter/in: Prof. Dr.-Ing. habil. Sigrid Leyendecker Prof. Dr.-Ing. Robert Seifried

Herausgeber

Prof. Dr.-Ing. habil. Sigrid Leyendecker Lehrstuhl für Technische Dynamik Friedrich-Alexander-Universität Erlangen-Nürnberg Immerwahrstraße 1 91058 Erlangen

© Copyright 2023 by Uday Phutane

Alle Rechte vorbehalten. Ohne ausdrückliche Erlaubnis des Autors ist es nicht erlaubt die Arbeit vollständig oder auszugsweise nachzudrucken, wiederzugeben, in Datenverarbeitungsanlagen zu speichern oder zu übersetzen.

All rights reserved. Without explicit permission of the author it is not allowed to copy or translate this publication or parts of it, neither by photocopy nor in electronic media.

Optimal control simulations of human hand grasping

Optimalsteuerungsimulationen des Greifens der menschlichen Hand

Uday Phutane

Schriftenreihe Technische Dynamik Band 8 2023 Herausgeber: Prof. Dr.-Ing. habil. Sigrid Leyendecker

Acknowledgements

The research presented in this thesis was conducted during my tenure as a research associate at the Institute of Technical Dynamics (Lehrstuhl für Technische Dynamik, LTD) under the guidance of Prof. Dr.-Ing. habil. Sigrid Leyendecker in the Department of Mechanical Engineering at Friedrich-Alexander-Universität Erlangen-Nürnberg from January 2016 to September 2021

I express my deepest gratitude to Prof. Leyendecker for providing me the opportunity to work with her in the field of multibody systems and human movement sciences. Her continuing guidance, camaraderie, persuasion, and trust played an instrumental role in bringing this thesis to fruition. I aspire to carry forward her teachings, both scientific and otherwise, throughout my life and, if possible, emulate her impact.

Special thanks are extended to Prof. Dr.-Ing. Robert Seifried for graciously agreeing to serve as a co-reviewer, PD Dr. sportwiss. Dr. habil. med. Anna-Maria Liphardt for accepting the role of an additional examiner, and Prof. Dr.-Ing. Nico Hanenkamp for presiding as the Chairperson for my defence committee. Their keen interest in my work and the intellectually stimulating conversations during the oral examination are sincerely appreciated.

The contribution of the project partners at the Fraunhofer Institute of Industrial Mathematics (Fraunhofer-Institut für Techno- und Wirtschaftsmathematik, ITWM) and Fraunhofer Center Chalmers through the MAVO-Project, EMMA-CC (Ergodynamic Moving Manikin with Cognitive Control) is also acknowledged.

This journey would not have been possible without the companionship of my colleagues at LTD, who shared countless ideas, late-night conversations, laughs, food, alcohol, blood, sweat and tears, and moments of challenge and triumph. I extend heartfelt thanks to Ramona Hoffmann, Thomas Leitz, Tobias Gail, and Maik Ringkamp for their mentoring, and to David Holz, Dhananjay Phansalkar, Martina Stavole, Johann Penner and Elisa Fleischmann for the cherished friendships. Special gratitude is also reserved

for Ms. Beate Hegen, whose support went above and beyond expectations.

In closing, I want to express my gratitude to my family and friends who stood by me during the highs and lows. My parents, through their tireless support, enabled me to pursue ambitions beyond my home country. My brothers, Aniket, and Rohit and his wife Priyanka, tirelessly picked up the slack on numerous occasions, and their contribution is immeasurable. Childhood friends, Shreyas and Anurag, provided steadfast companionship. Prof. Vinod Raul, from Sardar Patel College of Engineering, significantly shaped the person I am today, and I owe him immense thanks. Additionally, I acknowledge the pivotal role of my psychologist, Advaita Nigudkar, without whom I might have given up long ago.

Ultimately, my wholehearted appreciation goes to my wife Pooja, whose unwavering support was paramount, especially during the final sprint.

Augsburg, December 2023

Uday Phutane

Zussamenfassung

Ziel dieser Arbeit ist die Entwicklung eines Optimalsteuerungsaufbaus zur Durchführung dynamischer Greifsimulationen mit einer menschlichen Hand. Dies geschieht in erster Linie mit dem Ziel, bestehende digitale Menschmodellierungsumgebungen (Digital Human Modelling, or DHM) wie IMMA (Intelligently Moving Manikin) mit Funktionen auszustatten, die über quasi-statische Simulationen hinausgehen, während sie Montageplanung und ergonomische Studien durchführen. Die Optimalsteuerung findet auch außerhalb der DHM Anwendung, insbesondere in den Bereichen der medizinischen Diagnostik und Rehabilitation. Der Ansatz der Optimalsteuerung ist in der Lage, Sequenzen von Trajektorien und Steuerungen zu liefern, die zur Steuerung biomechanischer Systeme bei der Ausführung einer bestimmten Aufgabe verwendet werden, ohne dass Bewegungserfassungsmessungen erforderlich sind. Eine solche Sequenz wird durch die Minimierung einer Zielfunktion ermittelt. Der spezifische Ansatz zur Optimalsteuerung in dieser Arbeit nutzt strukturerhaltende Zeitschrittverfahren zur Beschreibung der beiden unterschiedlichen Formen der Dynamik eines mechanischen Systems. Die approximierten Lösungen, die mit Hilfe der vorgenannten Schemata erhalten werden, weisen die Eigenschaften des kontinuierlichen Systems auf, zeigen Drehimpulskonsistenz und ein gutes Langzeit-Energieverhalten.

Die Arbeit beginnt mit der Untersuchung des kinematischen Verhaltens des Daumens, das für die Greifkompetenz von Primaten entscheidend ist. Der Schwerpunkt verlagert sich dann auf das Verständnis der Greifgrundlagen, die sich vor allem aus der Sicht von Robotermanipulationsaufgaben ergeben. In diesem Teil legen wir die Grundlagen für unilaterale Mehrpunktkontaktsysteme. Diese werden durch kinematische Modelle erzeugt und charakterisieren die Kraft- und Geschwindigkeitsübertragungseigenschaften zwischen der Hand und dem Objekt durch Greifqualitätsmaße. Die Mehrkörpermodelle der Hand und des Objekts werden zusammen mit den Kontaktmodellen zu Schlüsselkomponenten bei der Entwicklung von Variationszeitintegratoren, die durch ein diskretes Variationsprinzip abgeleitet werden, um die Dynamik

der Hand zu beschreiben, die nach einem Objekt greift und es dann manipuliert. Die diskreten Bewegungsgleichungen, die die Greif- und Manipulationsaktionen darstellen, bilden ein hybrides dynamisches System, um das Optimalsteurungsproblem (OCP) des Greifens aufzustellen, bei dem die Umschaltung aufgrund der Durchsetzung der Kontaktbeschränkungen zu einem unbekannten Zeitpunkt erfolgt.

Das OCP wird als ein endlichdimensionales nichtlineares Optimierungsproblem formuliert, das in Bezug auf ein geeignetes physiologisches oder aufgabenbezogenes Ziel minimiert wird, um drei Griffe zu simulieren. Insgesamt werden vier Ziele aus den Perspektiven der Kontaktpunktpositionen, der Steuermomente, der Kontaktkräfte und der Handhaltung gewählt. Die numerischen Lösungen, die durch die Minimierung dieser Ziele erzielt werden, weisen ein gutes Maß an Unabhängigkeit auf und werden mit Hilfe von Maßzahlen für die Greifqualität bewertet. Die Werte des Maßes für die Uniformity of Transformation zeigen eine gute Variation zwischen den verschiedenen Zielen und Greifvorgängen. Sie können verwendet werden, um Strategien für die Handhaltung über verschiedene Ziele hinweg zu formulieren. Nach Optimalsteuerungsimulationen wird ein Ansatz zur Koordinierung der verschiedenen Gelenke in der Hand mittels eines reduzierten Unterraums eingeführt. Die Vektoren, die diesen Unterraum aufspannen, werden als kinematische Synergien oder Eigengreifer bezeichnet. Deren Effektivität zur Reduzierung des Lösungsraums für die Erzeugung von Handgriffhaltungen durch eine hybride kinematische Formulierung wird vorgestellt.

Abstract

The core objective of this work is to develop an optimal control setup to perform dynamic grasping simulations with a human hand. This is done primarily with a view to provide existing digital human modelling (DHM) environments such as IMMA (Intelligently Moving Manikin) the functionality to move beyond quasi-static simulations while performing assembly planning and ergonomic studies. The optimal control setup also finds applications beyond DHM, particularly in the areas of medical diagnostics and rehabilitation. The optimal control approach is capable to provide sequences of trajectories and controls that are used to drive biomechanical systems while performing a particular task without the need of motion capture measurements. Such a sequence is obtained via the minimisation of an objective function. The specific optimal control approach in this thesis makes use of structure preserving time-stepping schemes in describing the two distinct forms of dynamics of a mechanical system. The approximated solutions obtained by using aforementioned schemes inherit the characteristics of the continuous system, show angular momentum consistency and good long term energy behaviour.

The work begins with examining the kinematic behaviour of the thumb, which is the crucial to the grasping competence of primates. The focus then shifts to the understanding of grasping fundamentals that are mainly an outcome from the view of robotic manipulation tasks. In this part, we lay the foundation of unilateral multi-point contact systems. These are generated through kinematic models and characterize the force and velocity transmission properties between the hand the object through grasp quality measures. The hand and object multibody models along with the contact models become key components in the development of variational time integrators, derived through a discrete variational principle, to describe the dynamics of the hand reaching towards an object and then manipulating it. The discrete equations of motion representing the reaching and manipulation actions constitute a hybrid dynamical system to setup the grasping optimal control problem (OCP), where the switching occurs due to the enforcement of the contact

constraints at an unknown time.

The OCP is formulated as a finite dimensional non-linear optimisation problem which is minimised with respect to an appropriate physiological or task-based objective to simulate three grasps. In all, four objectives from the perspectives of contact point locations, control torques, contact forces and hand posture are chosen. The numerical solutions obtained by minimizing these objectives exhibit a good level of independence and are assessed using grasp quality measures. The values of uniformity of transformation measure shows good variation across the different objectives and grasps. They can be used helps to formulate policies regarding the hand posture across different objectives. Post optimal control simulations, an approach to coordinate the different joints in the hand by way of a reduced subspace is introduced. The vectors that span this subspace are termed as kinematic synergies or eigen grasps. Their effectiveness to reduce the solution space for generating hand grasp postures through a hybrid kinematic formulation is presented.

xii

Contents

1	Intro	oduction	1
	1.1	Robotic and human grasping	3
	1.2	Discrete mechanics and optimal control	5
	1.3	Thesis outline	6
	1.4	Publications	8
2	Thu	mb multibody model	10
	2.1	Multibody model description	11
			13
	2.2	Thumb anatomy	16
	2.3	Thumb multibody models	17
			19
	2.4		20
		2.4.1 RoM volume reduction for grasping	21
	2.5	Conclusions	23
3	Hun	nan grasping	25
	3.1	Grasping Theory	26
			29
		· · · · · · · · · · · · · · · · · · ·	32
			34
			36
			38
			39
	3.2	Grasp quality measures	41

Contents

	6.6	Conclusions	112
	6.5	Hybrid kinematics results	110
	6.4	Hybrid kinematics	107
	6.3	Synergy kinematics results	104
	6.2	Grasp closure objectives	102
	6.1	Synergy actuated hand model	101
6	-	ergy Effectiveness	100
	5.6	Summary	99
	F C	5.5.1 Overall observations	97
	5.5	Palmar pinch	93
	5.4	Lateral pinch	89
	5.3	Tip pinch soft contact model	84
	5.2	Tip pinch hard contact model	80
	5.1	Simulation parameters	78
5		sping optimal control simulations	77
	4.5	Summary	76
		4.4.3 Objective Functions	73
		4.4.2 Additional path constraints	69
		4.4.1 Hybrid dynamical system	65
	4.4	Grasping optimal control problem	64
	4.3	Derivation of discrete Euler-Lagrange equations	55
	4.2	Collision and grasping dynamics	53
	4.1	Continuous Lagrangian formulation	50
4	Gras	sping optimal control setup	49
	3.5	Summary	48
		3.4.2 Cylinder	47
		3.4.1 Box	45
	3.4	Object Models	45
	3.3	Hand Model	42
		3.2.1 Grasp isotropy index	42
			41

List of Symbols

 φ position

 $\{d_I\}_{I=1,2,3}$ orthonormal director frame

 $\{e_I\}_{I=1,2,3}$ inertial frame

 m_{int} number of internal constraints

 $egin{array}{lll} n & ext{time step node} \\ m{u} & ext{kinematic update} \\ m{u}_{m{arphi}_{n+1}} & ext{translation increment} \\ m{ heta}_{n+1} & ext{rotation increment} \\ \end{array}$

 F_d discrete nodal reparameterisation

 $R(\bullet)$ rotation matrix

 $oldsymbol{g}_{ext}^{j}$ holonomic joint constrains

 $\{\varrho^b_I\}_{I=1,2,3} \qquad \text{material point coefficients for body } b \\ \pmb{F}^j_d \qquad \qquad \text{joint-specific nodal reparameterisation}$

n rotation axis

q hand configuration vector

 $oldsymbol{q}^O$ object configuration

a finger digit

T tangential plane u hand twist vector τ joint control torques

P	hand kinematic null-space matrix
\dot{q}	hand configuration velocity
$oldsymbol{f}^{app}$	wrench applied to object through contacts
f^{ext}	external wrench acting on object
${\it G}$	Constraint Jacobian
λ	Lagrange multiplier
F	Friction cone
$oldsymbol{f}^{O,A}$	contact force acting on object at point A
I	Identity matrix
μ	Coefficient of static friction
$oldsymbol{n}^A$	outward normal to the object at point A
$\{\varrho_I^O\}_{I=1,2,3}$	object contact point coefficients
$oldsymbol{R}^a$	contact point frame at point A
$oldsymbol{t}^a,oldsymbol{o}^a$	vectors spanning the tangential plane to the object at point \boldsymbol{A}
$G_ u$	grasp matrix
$H_ u$	Hand Jacobian
$oldsymbol{ u}^C$	contact points
Q_1	Grasp Isotropy Index
Q_2	Uniformity of Transformation Index
Q	configuration manifold
t	time
E	total energy
$\mathcal L$	Lagrangian
\mathcal{T}	kinetic energy
\mathcal{V}	potential energy
l	dimension of the hand configuration

S action integral

 $\tilde{\mathcal{L}}$ augmented Lagrangian

 δW virtual work

f non-conservative external forces

 \tilde{S}_d discrete action sum

 $ilde{S}_{d,1}$ discrete action for reaching phase $ilde{S}_{d,2}$ discrete action for gap closure instant $ilde{S}_{d,3}$ discrete action for manipulation phase

D differential operator B transformation matrix

T time interval

 N_k number of time nodes for reaching phase N_m number of time nodes for grasping phase ϱ vector of contact points for the hand T_k optimal duration for reaching phase T_m optimal duration for grasping phase

 ${f R}^{ba}$ relative rotation matrix between bodies a and b S^a Surface limits for contact points on finger digit a

 S^{O} Surface limits for contact points on object

 d_1, d_2 Cylindrical cross-section of the digit

 $egin{array}{ll} egin{array}{ll} egi$

 $g_f(q_n^O)$ object fix constraints

 J_0 unity function

 J_1 grasp contact polygon centroid objective

Contents

J_2	rate of change of control torques objective
J_3	normal contact force objective
J_4	comfortable joint flexion objective
X	optimisation variables
z	synergy values
S	kinematic synergy matrix

List of Tables

2.1	Ranges of motion for thumb joints, taken from [DIL13]	20
2.2	Volume reduction results for all models	23
3.1	Plane definitions for box	46
5.1	The table provides the information about the problem size for the optimisation to perform tip, lateral and palmar pinch simulations, with n_c contact points. It details the values for the time steps for the reaching N_k and manipulation N_m phases and the number of optimisation variables X , inequality c , and equality c constraints.	79
5.2	The table shows the evaluation of the different objective functions at the different optimal solutions $J_{i,j}$ while performing tip pinch grasp with hard contacts	81
5.3	The table provides the phase durations in seconds for the different objectives while performing tip pinch grasp with hard	00
5.4	The table shows the grasp quality measures for the different objectives while performing tip pinch grasp	82 84
5.5	The table shows the evaluation of the different objective functions at the different optimal solutions $J_{i,j}$ while performing tip pinch grasp with soft contacts	85
5.6	The table provides the phase durations in seconds for the different objectives while performing tip pinch grasp with soft	
	contacts	87

5.7	The table shows the grasp quality measures for the different	90
5.8	objectives while performing tip pinch grasp with soft contacts. The table shows the evaluation of the different objective func-	89
	tions at the different optimal solutions $J_{i,j}$ while performing	0.0
- 0	lateral pinch grasp	90
5.9	The table provides the phase durations in seconds for the	0.1
5.10	different objectives while performing lateral pinch grasp The table shows the grasp quality measures for the different	91
	objectives while performing lateral pinch grasp	93
5.11	The table shows the evaluation of the different objective func-	
	tions at the different optimal solutions $J_{i,j}$ while performing	
	palmar pinch grasp	94
5.12	The table shows the grasp quality measures for the different	
	objectives while performing palmar pinch grasp	95
5.13	The table compares the grasp quality measures for the different	
	objectives while performing palmar pinch grasp	97
6.1	Objective values for synergy actuated model with prismatic	
	2-finger grasp. The $J_1 + J_2$ column shows objective function	
	values by minimising function in Equation (6.7), with J_1 and	
	J_2 columns showing the component values. The column only J_1	
	shows objective function values while minimising Equation (6.6).	107
6.2	Objective values for synergy actuated model with tripod grasp.	
	1	109
6.3	The table provides the information about the problem size	
	for the optimisation variable X to perform either prismatic-2-	
	finger or tripod grasp simulations, with 3 contact points with	
	10 time nodes. The number of contact points and object radius	
	is excluded as it is common in the constraint based, synergy	
	based and hybrid kinematic cases. With these exclusions, we	
	get reduced optimisation vector $X_{\rm red}$	110

List of Figures

2.1	Description of a rigid body in three-dimensional space with respect to an orthonormal inertial frame $\{e_I\}_{I=1,2,3}$	11
2.2	A generic kinematic chain example with two bodies having configurations q^1 and q^2 . Body b^1 is free to move in space and b^2 is connected to b^1 via joint j , described with holonomic constrains $g_{ext}^j\left(q^1,q^2\right)=0$. The bodies b^1 and b^2 are connected to the joint via vectors $\boldsymbol{\varrho}^1$ and $\boldsymbol{\varrho}^2$, respectively	13
2.3	The kinematic pair with non-intersecting and non-orthogonal axes n^1 and n^2 between bodies b^1 and b^2 with configuration vectors \mathbf{q}^1 and \mathbf{q}^2 , respectively. The local vectors \mathbf{q}^1 and \mathbf{q}^2 define the locations of the points P_1 and P_2 for the axes \mathbf{n}^1 and \mathbf{n}^2 , while the vector \mathbf{d} connects these points. $\{\mathbf{e}_I\}_{I=1,2,3}$ is the spatially fixed orthonormal basis	15
2.4	The figure shows thumb anatomy with bone and joint nomen- clature and associated multibody model with anatomically correct locations and orientations for the MCP and the CMC, and IP axes	17
2.5	The CMC adduction-abduction axis, reproduced here from [HBM ⁺ 92], is located in the head of the I MC (above). The orientation of the axis is defined with angles α and β . The location of the axis is defined with two length ratios t/T and l/L. The values are shown in the table (below), taken from [HBM ⁺ 92]	18
	[1112/1VI J2]	10

2.6	The different thumb models used to compare validation results. The base model is created with the mean values from cadaver measurements. The models named as types I, II, III and IV are taken from [SVC06]. The models have differences in the axes locations and orientations. For example, the base, type II and type III models have the MCP add-abd axis proximal with respect to its flex-ext, when compared with type I and type IV models	19
2.7	The point cloud for base model with maximum RoM	21
2.8	α -shapes for all models with maximum (blue) and grasp (red) RoM	22
3.1	An object O with configuration \boldsymbol{q}^O is in contact with a finger digit a with configuration \boldsymbol{q}^a at point A . $\begin{bmatrix} \boldsymbol{n}^A, \ \boldsymbol{t}^A, \ \boldsymbol{o}^A \end{bmatrix}$ forms a orthonormal frame at the contact point with \boldsymbol{n}^A as outward normal to the object surface and $\begin{bmatrix} \boldsymbol{t}^A, \ \boldsymbol{o}^A \end{bmatrix}$ spans the tangential plane T	27
3.2	A two dimensional view of an object O in contact with two digits a and b of a hand at points A and B , respectively	28
3.3	Kinematic representation of a point contact without friction contact model between digit a and object O . The vectors $\varrho^{A,a}$ and $\varrho^{A,O}$ connect the mass centres of the digit and object, respectively, to the contact point A . The dashed lines represent that the contact points may move within areas S^a and S^O on the digit and object, respectively, where the contact is to be maintained	30
3.4	Kinematic representation of a hard contact model between digit a and object O , extending the PwoF model from Figure 3.3. The contact point vectors $\boldsymbol{\varrho}^{A,a}$ and $\boldsymbol{\varrho}^{A,O}$ are fixed, while the orientations between the digit and the object along the directions (represented by dashed lines) in the contact point frame $[n^A, t^A, o^A]$ are free	32
3.5	The representation of the force f^O lying inside a friction cone F at contact point $\varrho^{O,a}$	33

3.6	Kinematic representation of a soft contact model between digit	
	a and object O , extending the PwoF and hard contact models	
	from Figure 3.3 and Figure 3.4, respectively. Along with fixing	
	the contact point vectors $\boldsymbol{\varrho}^{A,a}$ and $\boldsymbol{\varrho}^{A,O}$, the rotation around	
	the normal n^A is constrained	35
3.7	The relationship between the object and hand twist and force/torq	ue
	spaces through the G_{ν} , G_{ν}^{T} , H_{ν} , and H_{ν}^{T} matrices, reproduced	
	from [RS14]	38
3.8	Left: Form closure for a two-dimensional object achieved with	
	four contact points, each modelled with PwoF contact model.	
	Right: Force closure for the similar object possible with two	
	contact points modelled with hard contact model	40
3.9	The two-finger hand model with the joint axes for different	
	joints. The adjoining table shows the joint types	43
3.10	1	
	b with radius r^b and length $2\ell^b$. The directors d_1^b, d_2^b represent	
	the cross-section, while d_3^b represents the axis	44
3.11	The plane definitions on a box along with location of contact	
	$ \varrho^{O} $ and the normal n_{box} at that location	46
3.12	The depiction of contact surface on a cylinder with contact	
	point location $\boldsymbol{\varrho}^O$ and the normal \boldsymbol{n}_{cyl} at that location	47
4.1	The reaching and manipulation phase description in the grasp-	
	ing problem. In the reaching phase, the finger digit, represented	
	by a ball, moves toward the object surface S . After the gap	
	d between them becomes zero, the two move together in the	
	manipulation phase	54
4.2	The grasping OCP setup with the time grid of the reaching	
	and the grasping phase and the contact-related equality and	
	inequality constraints in the two phases describe the hybrid	
	dynamical system. The placeholders $D_u f = D_1 \mathcal{L}_d (q_{n-1}, q_n) + Q_n f$,
	$D_2 \mathcal{L}_d \left(\boldsymbol{q}_n, \boldsymbol{F}_d \left(\boldsymbol{u}_{n+1}, \boldsymbol{q}_n \right) \right) + \boldsymbol{f}_{n-1}^+ + \boldsymbol{f}_n^- \text{ and } D_q^O = D_1 \mathcal{L}_d^O \left(\boldsymbol{q}_{n-1}^O, \boldsymbol{q}_n^O \right)$)+
	$D_2\mathcal{L}_d^O\left(\boldsymbol{q}_n^O,\boldsymbol{q}_{n+1}^O\right)$ are the DEL equations of motion. The addi-	
	tional constraints are catalogued in Section 4.4.2	66
4.3	The angles for the proximal (θ_{PIP}) and distal (θ_{DIP}) interpha-	
	langeal joints in the index finger	73

5.1	The tip, lateral and palmar pinch postures (a) $-$ (c) as taken from [FRS ⁺ 16] and configurations for the simulation with	
	contact points ((\lozenge) for the thumb and (\square) for the index finger)	
	defined on the fingers for the corresponding grasps (d) – (f).	
	The shaded areas are the limits of the surface areas for the	70
- 0	contact points on the different finger digits	78
5.2	Snapshots tip pinch grasping maneuver with hard contacts	
	at different time nodes. Two configurations at different time	
	nodes are superimposed in each of the three pictures. The	
	hand starts from an open posture at $n = 1$ with grasp closure	
	obtained at $n = N_k = 7$. Thereafter, a lifting task is performed	90
- 0	with postures shown for time nodes $n = 11, 22.$	80
5.3	Location of the contact points on the finger digits and the	
	object for the different solutions for tip pinch grasp with hard	99
- 1	contacts, along with the initial guess	82
5.4	Time evolution of the control torques for the different solutions	
	while performing tip pinch grasp with hard contacts, for the	
	thumb CMC joint τ_1^{CMC} (top-left), τ_2^{CMC} (top-right) and the finger MCP joint τ_1^{MCP} (bottom-left), τ_2^{MCP} (bottom-right).	09
		83
5.5	Time evolution for the contact forces applied by the finger digits, thumb (left) and index finger (right) on the object for	
	different objectives while performing tip pinch grasp with hard	
	contacts	84
E 6		04
5.6	Snapshots tip pinch grasping maneuver with soft contacts at different time nodes. Two configurations at different time nodes	
	are superimposed in each of the three pictures. The hand starts	
	from an open posture at $n=1$ with grasp closure obtained	
	at $n = N_k = 7$. Thereafter, a lifting task is performed with	
	postures shown for time nodes $n = 11, 22, \ldots$	85
5.7	Location of the contact points on the finger digits and the object	
0.,	for the different solutions for tip pinch with soft contacts, along	
	with the initial guess	86
5.8	Time evolution of the control torques for the different solutions	
	while performing tip pinch grasp with soft contacts, for the	
	thumb CMC joint τ_1^{CMC} (top-left), τ_2^{CMC} (top-right) and the	
	thumb CMC joint τ_1^{CMC} (top-left), τ_2^{CMC} (top-right) and the finger MCP joint τ_1^{MCP} (bottom-left), τ_2^{MCP} (bottom-right).	87

5.9	Time evolution for the contact forces applied by the finger digits, thumb (left) and index finger (right) on the object for different objectives while performing tip pinch grasp with soft contacts	88
5.10	Snapshots of the lateral pinch grasping maneuver at different time nodes. Two configurations at different time nodes are superimposed in each of the three pictures. The hand starts from an open posture at $n=1$ to hold the sides of the key at $n=N_k=5$. Thereafter, the key is lifted to a predefined height and orientation at $n=13$, after which a clockwise rotation is performed to end the manipulation phase at $n=17$	89
5.11	Location of the contact points on the finger digits and the object for the different solutions for lateral pinch, along with the initial guess	91
5.12	Time evolution of the control torques for the different solutions while performing lateral pinch grasp, for the thumb CMC joint τ_1^{CMC} (top-left), τ_2^{CMC} (top-right) and the finger MCP joint τ_1^{MCP} (bottom-left), τ_2^{MCP} (bottom-right)	92
5.13	Time evolution for the contact forces applied by the finger digits, thumb (left) and index finger (right) on the object for different objectives while performing lateral pinch grasp. For each plot, the force value for solution X_4 is shown with respect to the right-side vertical axis limits	93
5.14	Snapshots for the palmar pinch grasping maneuver at different time nodes. Two configurations at different time nodes are superimposed in each of the three pictures. The task is to pick and place a cube from predefined initial and final positions. The hand starts from an open posture $n=1$ and closes the grasp at $n=N_k=7$. The manipulation phase shows the placing motion with time nodes $n=11,22,\ldots$.	94
5.15	Location of the contact points on the finger digits and the object for the different solutions for palmar pinch, along with	95
	the initial guess	90

5.16	Time evolution of the control torques for the different solutions while performing palmar pinch grasp, for the thumb CMC joint	
	$ au_1^{CMC}$ (top-left), $ au_2^{CMC}$ (top-right) and the finger MCP joint $ au_1^{MCP}$ (bottom-left), $ au_2^{MCP}$ (bottom-right)	96
5.17	Time evolution for the contact forces applied by the finger digits, thumb (left) and index finger (right) on the object for different objectives while performing palmar pinch grasp. For each plot, the force value for solution X_4 is shown with respect	
	to the right-side y-axis limits	97
5.18	The grasp quality measures Q_1 (left) and Q_2 (right) for the different objectives J_1, \ldots, J_4 and the initial guess J_0, \ldots, J_4	98
6.1	The multibody hand model. Left: the modelling of the digits as cylindrical geometries. Right: the tree structure with the number of DoFs in the circles. The one and two DoF joints are modelled as revolute and cardan (fingers) / nino (thumb),	
	respectively.	102
6.2	Left: the contact closure condition expressed in Equation 6.4. Right: the tangential contact condition expressed in Equation	
	6.5	103
6.3	Synergy actuated model ($n_z=15$) with prismatic 2-finger grasp by minimising J_1+J_2 objective. The contact points are	
	shown with (\bullet) symbol	105
6.4	From left to right, we see the grasp posture for prismatic 2-finger grasp with (left) non-synergy actuated model while minimising $J_1 + J_2$ objectives, (middle) synergy actuated model with $n_z = 15$ synergies and only J_1 objective to be minimised and (right) synergy actuated model with $n_z = 5$ synergies while minimising $J_1 + J_2$ objectives. The contact points are	
	shown with (•) symbol	106
6.5	Synergy actuated model with tripod grasp, see [FRS ⁺ 16], with $n_z = 15$ (left) and $n_z = 5$ synergies. The contact points are	100
<i>c c</i>	shown with (•) symbol	108
6.6	Comparison of the grasp postures for Prismatic 2-Finger grasp with the synergy (left) and hybrid (right) kinematic model.	
	Both simulations have been executed with $n_z = 2$ synergies.	111

6.7	Comparison of the grasp postures for tripod grasp with the	
	synergy (left) and hybrid (right) kinematic model. Both simu-	
	lations have been executed with $n_z = 2$ synergies	111



1 Introduction

There is a renewed interest in the recent years concerning the research of digital human modelling (DHM) within the scientific and artistic communities. After the first comprehensive handbook on DHM by Duffy [Duf08], the consolidation of different software tools has been done of late in the book DHM and Posturography [SP19], as well as some review articles such as [Cha08, YSY⁺15, WMW20].

DHM simulations are carried out using multibody models representing the human musculoskeletal system as a kinematic tree with actuators. Across academic and industrial research, the development of DHMs is of high importance in human factor ergonomic and medical studies. The commercial softwares used in industry, such as Jack, or RAMSIS or IMMA, are kinematically or quasi-statically driven solving posture optimisations of human models. The inverse kinematic solutions required in applications such as assembly planning, user envelope rendering or automotive system packaging are obtained through the minimisation of certain comfort functions applied to anthropometric models. The postures obtained are used to determine the possible forces in the human joints for estimating probable health disorders, however, with very low accuracy. On the other hand, DHMs are also used in dynamic simulation to either simulate human responses to external stimuli, such as occupant response in automotive pre-collisions with the help of softwares like MADYMO. However, their major drawbacks are that they does not allow for forward dynamics, which is a critical requirement in contemporary times towards generating predictive motion through optimisation. In this context, we discuss the collaborative MAVO project, EMMA-CC, which expands to Ergo-dynamic Moving Manikin with Cognitve Control¹. The project is constituted with the following objective

"... the development of an enhanced digital human model for ergonomic assessment of dynamic motions by validated simulation

¹https://www.emma-cc.com/en.html

to support the design of healthier and safer work places in future product development and product planning processes."

Another shortcoming with respect to the state-of-the-art DHM applications is the lack of technical development in the space of modelling hand motion realistically. In dynamic and even kinematic simulations, a physically and anatomically correct hand model is necessary to perform interactive motions with surrounding systems. The primary objectives in these simulations are understand contact forces and joint loads during activities of daily living, which are useful to assess work-spaces and design tools to avoid high risk of developing cumulative hand trauma disorders, see [BA92, MK92, LMSB14]. These activities can be in different environments, such as vehicle integration and packaging in assembly planning, reach analysis for household products as well as automotives, and also prototype testing in the digital environment. The primary human activity in these applications is grasping and manipulating different objects. This activity can be broken down into a number of subactivities, namely, but not limited to, object or surrounding cognition, grasp choice and closure through appropriate contact modeling, and task trajectory planning.

With this motivation, within the ambit of the large-scale EMMA-CC project, we formulate the objective of our sub-project as follows,

"Given a digital human model capable of cognitive decision-making and a-priori knowledge of the surroundings, develop an optimal control setup to perform predictive simulations of reaching and manipulation tasks, e.g. moving a known object from point A to point B with a human hand."

The sub-project can be approached via two key methods. On the one hand, it would be possible to choose an existing grasping simulator and incorporate it into an optimal control environment. On the other hand, it would be logical to begin with a tried-and-tested optimal control setup and include the grasping functionality in it. This resembles a "chicken-and-egg" situation. Given the black-box nature of available grasping simulators with their unproven capabilities in handling complete grasping dynamics, it is preferred to go with the second approach, i.e. to formulate an optimal control problem to perform grasping simulations.

In the following sections, we first discuss the state-of-the-art with respect to the grasping research, followed by the current trends in optimal control simulations. Thereafter, we describe the outline of the work carried out in this thesis.

1.1 Robotic and human grasping

A simplified way to sift through the enormous amount of grasping research all would be to break it down into two groups, namely robotic and human grasping. The research in these two areas are driven by different motivations. In particular, human grasping research is directed from the point of view of the biomechanical modeling, classification of the grasp types and its application in ergonomics and medicine. On the other hand, robotic grasping focuses include grasp stability, gripper design with their control and adhesion strategies, as well as environment awareness with concepts such as collision detection and symbolic task planning.

Earliest grasping research contributions shed light on postures and definition of human grips, namely power and precision [Nap56, Lan62], from anatomical and functional points of view. This was followed by investigations into human hand construction from a medical point-of-view [rC77, CLCL81, ACCL79] with tendon structure, hand normative models, and force analysis in fingers and thumbs. This was motivated fundamentally by ergonomics, tool design, and hand function and anthropometry [BA92, BAG92]. For example, [COA76] presented a system of equations to describe the dynamics of power and precision grips while solving for joint and tendon forces. The research followed with further development of 3D-biomechanical models with detailed modeling for the musculo-skeletal structure of the hand, see [VCJT03, SB00, Sac19].

In addition, the kinematic behavior and modelling of the thumb joints played an important role in human grasping. The opposition and circumduction motions of the thumb makes humans (and primates) capable of performing a wide assortment of grasps. These motions are possible due to the rotation of the thumb metacarpal along its longitudinal axis, which is an outcome due to the location and orientation of the two thumb rotation axes which perform the flexion/extension and adduction/abduction motions. Through cadaver measurements [HBM⁺92, HGB⁺95], these axes were determined to be non-intersecting and non-orthogonal, which is in contrast to the many

biomechanical models which model the thumb joint as a universal joint, see [SBML⁺14, JBAM20, WAC⁺09]. Additionally, when compared with physical measurements, a thumb model with universal joints does not produce accurate forces at its tip in different postures, see [VCJT03].

Another aspect of human grasping is the study of coordination between the different joints,while performing reaching motions. These are possible due to the hand actuation system, composed of the musculo-tendon structure and the central nervous system. It was evaluated that number of dimensions to symbolize the degrees of freedom of the hand was considerably smaller than those that were measured [SFS98]. It was possible to establish a linear relationship between the reduced and actual number of degrees of freedom of the hand. This relationship has been exploited in simulators such as Syngrasp [MGS⁺13] and *Graspit!*[MASV05] to reduce problem complexity and improve grasp postured through coordinated hand prehension.

The mathematical formalisation of grasping concepts were set up in concurrence the advent of robotic hands or mechanical manipulators [SC82, LS88, Cut89, MJ85, Cra09, MK16, as well as grasping simulators such as Graspit!, OpenGRASP [LUD⁺10], or Syngrasp. The development of these simulators or manipulators was accompanied with the advancement of concepts of grasp synthesis [FC92, ZW03, Shi96, CLA07, SEKB12], grasp analysis [Bic94, BBPB05, CMFdP05] or grasp posture optimisation [Bic92, PAF94, KOYS01]. Grasp synthesis is the process of obtaining either one or multiple postures with force closure for robotic manipulators with respect to a particular object. These processes may be performed either quasi-statically as in the case of many DHM environments, or in some cases, dynamically, through a number of different algorithms such as rapidly-exploring random trees [VDAD10, AL20] or genetic algorithms [SS21]. The examples of grasp synthesis algorithms strongly related to our work where task and motion planning is done concurrently, has been demonstrated in recent contributions [ZHZ⁺20, IDX⁺20, GHRZ19], with a review in [GCH⁺21]. In particular, [IDX⁺20] focuses on time minimization in the manipulation phase, by performing a pick-and-place action of a garbage bin. Herein, an optimal solution is one which is feasible with the lowest number of discrete time steps, subject to certain kinematic constraints. In [ZHZ⁺20], a multi-level optimisation problem is considered to plan the reaching and manipulation trajectories. The different levels determine the optimal grasping locations, robot poses and

collision-free trajectories, in that order.

Grasp analysis involves the study of form and force closure grasps and pushed for the definition of a 'good' grasp, which were qualified through certain criteria, namely grasp quality measures, see [RS14]. The involve mainly the type of contact models and optimal contact point locations that are used to achieve grasping. Over a period of three decades, the number of such measures has matured encompassing several kinematic and dynamic concepts, such as those derived from the grasp matrix and the hand Jacobian. These measures have found usage as either metrics for ranking grasps or as objective functions in optimisation problems to obtain grasping solutions.

In recent times, we have seen a few examples to include robotics-derived grasping concepts in human biomechanical model driven grasping simulations. [SBML+14] presents an example to perform human grasping simulations with a view to evaluate compare contact forces with measurements by holding objects of different weights and sizes. In this contribution, as also [RSGD19], kinematic input was provided to the model by way of measurements obtained with a Cyberglove® system (Cyberglove, Immersion Corp. San Jose, California, USA). While observing that physiological-based objectives such as the maximisation of muscle endurance [CB81] are inadequate to estimate contact forces correctly, [SBML+14] stressed for the need of including "task-dependent grasp quality measures". Furthermore, in another study [LMSB14] made use of grasp quality measures to characterize 36 hand postures obtained from measuring joint angles while grasping a cylinder in different ways.

1.2 Discrete mechanics and optimal control

The implementation of optimal control methods to perform biomechanical trajectory optimisations has been established through a number of examples in recent years. Some of these include in sports such as cycling [JM20, ZBP+17], golf [BMM20], running [NDH+20], as well as activities of daily living such as gait [BBH11, Koc16] or lifting actions, see [BLL+18, MSM17]. The fundamental objective herein is to find controls, either joint torques or muscle activations, to perform movement of a musculoskeletal system is such a way as to minimise or maximise a certain physiological or task-related criterion. The implementation in the above examples is normally composed of mixing-and-matching of a number of concepts, e.g. choice of

biomechanical modeling, optimal control through direct or indirect methods, use of physiological or task-based objective functions, smooth or non-smooth dynamics, tracking or predictive motion etc., to name a few.

A particular choice is made regarding the time-stepping scheme that is used to numerically solve the equations of motion which describe the dynamics of the system. In case of temporal discretization, which is commonly used to solve the class of problems mentioned above, the accuracy of a numerical solution is a consequence of the discretization technique, the parameters used and the time-step size, while taking into account the computational cost. In this context, we focus on the use of variational integrators that are derived from a discrete variational principle [MW01]. These variational integrators preserve the structure of the dynamical system by inheriting the characteristics of the continuous one. Also, they provide good accuracy and convergence properties, along with symplecticity, momentum-preservation and good long-term energy behaviour.

The discrete equations of motion pertaining to the variational integrator are included in the trajectory optimisation as constraints [JMOB05]. This inclusion imparts the structure preserving characteristics of the variational integrator to the optimal control problem, as shown in the direct transcription method, DMOC (discrete mechanics and optimal control) [OB08]. In [LOBMO10], this method has been extended to include holonomic constraints, named DMOCC (discrete mechanics and optimal control for constrained systems). This is a critical feature to solve non-smooth dynamics systems, such as gait, or more importantly grasping, as the contact between different mechanical systems is expressed via holonomic constraints.

1.3 Thesis outline

In this work, we apply the DMOCC paradigm to transcribe the infinite dimensional OCP into a finite-dimensional non-linear constrained optimisation problem to setup the grasping action. The OCP is modelled as a hybrid dynamical system with two sequential phases having distinct dynamics for a variety of kinematic and dynamic, physiological and grasp-based objectives. The discrete equations of motion describing the different dynamics are derived using a discrete variational principle, extending the non-smooth dynamics derivation by [Joh13, Koc16]. The grasping performance is also compared

through the different solutions for the contact points and forces, and the control torque actuation, as also through grasp quality measures.

Before moving to the actual derivation and the setup of the grasping OCP, we focus two topics concering to the biomechanical model of the hand and the fundamentals of grasping. In Chapter 2 we focus on the crucial component of the human hand with respect to its grasping capabilities, namely the kinematic model of the thumb. The chapter explores the complexity of the thumb joints and discusses a method to understand and compare thumb grasping performance across different models. The differences are present due to the choice of different joint location and orientation parameters which occur due to the variation in human anatomy across people. Chapter 3 gives the reader an overview on the mathematical fundamentals that form the building blocks to understand complex grasping topics. In particular, we discuss the force and velocity transmission between the hand and the object through different contact models and their influence on form and force closure properties for a particular grasp. The chapter concludes with the description of the hand and the object models that are used in the following chapters to perform grasping simulations.

The next block of chapters address the core of this thesis, i.e. the grasping optimal control problem (OCP). In Chapter 4 we discuss the mechanics of deriving the time-continuous equations of motion for a mechanical system with and without non-smooth dynamics. Thereafter, we derive the discrete Euler-Lagrange equations of motions which represent the two phases in the grasping simulation, by making use of the contact models in the previous chapter. Following on, we build the discrete OCP and discuss the hybrid dynamical system driving the grasping maneuver dynamics along with the list of equality and inequality constraints that complete the OCP. Finally, we review the objective functions which are minimised in the nonlinear optimisation problem to generate the different grasping trajectories. With this formulation, we perform the simulations in Chapter 5 with three grasp types and different contact models. The optimisation results are compared for every grasp maneuver across the different objectives with respect to the contact forces and joint torques, among other quantities.

In Chapter 6, we put forth an example for a model reduction technique based on the hand kinematic synergies to decrease the problem size and computational complexity in grasping problems. Finally, in Chapter 7, we review and summarise the conclusions and outlook from the thesis.

1.4 Publications

The thesis builds upon the manuscripts written, along with the development and implementation of the grasping OCP algorithm, completely by the author and published over the course of research performed at the Institute of Applied Dynamics² in joint work with colleagues from Fraunhofer Institute of Industrial Mathematics³ and Fraunhofer-Chalmers-Center⁴, under the supervision of Prof. Dr.-Ing. habil. Sigrid Leyendecker². In particular, excerpts from the following three contributions are used in this thesis, namely,

- [PRB⁺17] Uday Phutane², Michael Roller³, Staffan Björkenstam⁴, Joachim Linn³, and Sigrid Leyendecker². Kinematic validation of a human thumb model. In *ECCOMAS Thematic Conference on Multibody Dynamics*, pages 857–866, 2017.
- $[PRBL20] \qquad \text{Uday Phutane}^2, \text{ Michael Roller}^3, \text{ Anja Boebel}^2, \text{ and Sigrid Leyendecker}^2. \text{ Optimal control of grasping problem using postural synergies. } \textit{DHM2020}, \text{ pages } 206-213. \text{ Volume } 11, 2020.$
- [PRL22] Uday Phutane², Michael Roller³, and Sigrid Leyendecker². Optimal control simulations of two-finger grasps. *Mechanism and Machine Theory*, 167:104508, 2022.

[PRB⁺17] forms the basis of Chapter 2 including the newly developed joint description and accompanying results. [PRBL20] gives the foundation for the use of kinematic synergies in the multibody director formulation and to build towards a hybrid kinematic formulation to perform grasping using synergies in Chapter 6. The article [PRL22] covers the hybrid dynamical formulation, the grasping optimal control problem and simulation results which have been repeated in this thesis across Chapters 3 to 5. In Chapters 3 and 4 the thesis provides the mathematical background and derivations for the equations which build up the grasping optimal control problem while

²https://www.ltd.tf.fau.de

 $^{^3} https://www.itwm.fraunhofer.de/de/abteilungen/mf.html\\$

⁴https://www.fcc.chalmers.se/departments/geo/

Chapter 5 contributes with additional simulation results and discussions. Some parts of the presented literature survey in the previous sections have also been taken from the above listed contributions.

The remaining material is so far not published anywhere.

2 Thumb multibody model

Grasping is a unique function exhibited primarily by primates, through the versatility of motion provided by the thumb and its motions such as opposition and circumduction. The thumb is responsible for over 50% of the hand function, see [Sou01]. Anatomically, the thumb is composed of three bones. From the base in the wrist to the thumb tip, they are the first metacarpal (I MC), the proximal phalanx (PP) and the distal phalanx (DP), see [Kap81]. They are connected in series by three joints with the trapezium bone in the wrist. The carpometacarpal (CMC) joint connects the trapezium and the I MC, the metacarpophalangeal (MCP) joint connects the I MC and the PP, while the interphalangeal (IP) joint connects the PP and the DP. The MCP and the CMC are saddle joints and have two rotational degrees of freedom (DoFs), namely flexion-extension (flex-ext) and adduction-abduction (add-abd), while the IP has a single rotational DoF i.e. flex-ext. The CMC and MCP joints show a third motion of pronation-supination (pro-sup) or internal rotation along their longitudinal axes during the combined motions, which is not an inherent DoF of the thumb joints, rather an outcome, see [CLCL81]. Kindly bear in mind that this chapter is based on [PRB+17] to a large extent.

The kinematic modelling of the thumb in multibody models is dependent on the parameters used to describe the thumb joints. Historically, these are usually extracted from cadaver studies, e.g. [HBM⁺92, HGB⁺95] and are expressed with a mean \pm standard deviation, which does not represent the human variability ideally. A kinematic model created using the mean values can be at best a faux-generic model. In this chapter, we investigate the kinematic behavior of such a generic (base) thumb model and four anatomic variations and describe a validation method to assure proper thumb kinematics. The method involves the comparison of work-space point cloud volumes generated by the thumb tip, which are computed using α -shapes [DIL13]. We compare the grasping performance of the base model with respect to the anatomically variable models.

We first introduce the multibody formulation used to model the thumb, and thereafter the hand, in this thesis in Section 2.1. In the next sections, we comment on the prevalent assumptions in thumb kinematic modeling in Section 2.2 and the thumb multibody models for base and anatomically variable parameters in Section 2.3. Thereafter, we describe the validation methodology with results in Section 2.4, followed by the conclusions in Section 2.5.

2.1 Multibody model description

The multibody description in this work follows a constrained multibody formulation, as described in [BS01, BL06, Ley08]. It avoids the difficulties posed by the rotational parameters, angular velocities and accelerations in the Lagrangian. A rigid body is specified by a time-dependent parameters describing its position $\varphi(t) \in \mathbb{R}^3$ and orientation $\{d_I(t)\}_{I=1,2,3} \in \mathbb{R}^3$ with respect to an inertial frame $\{e_I\}_{I=1,2,3}$, as shown in Figure 2.1. The redundant

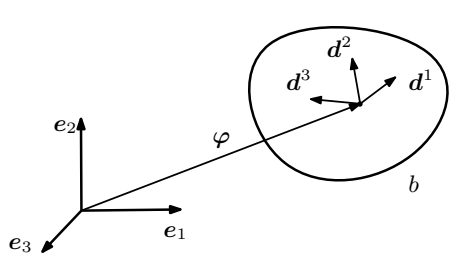


Figure 2.1: Description of a rigid body in three-dimensional space with respect to an orthonormal inertial frame $\{e_I\}_{I=1,2,3}$.

configuration variable for the rigid body is expressed with 12 variables as

$$q(t) = \begin{bmatrix} \varphi \\ d_1 \\ d_2 \\ d_3 \end{bmatrix} \in \mathbb{R}^{12}$$
 (2.1)

The orientation $\{d_I(t)\}_{I=1,2,3}$ consists of a body fixed triad. The body's rigidity causes the directors to stay orthonormal during the motion. These kinematic orthonormality conditions are termed as internal constraints. There are $m_{int}=6$ independent internal constraints for the rigid body, which are specified through

$$\mathbf{g}_{int}\left(\mathbf{q}\right) = \begin{bmatrix} \frac{1}{2} \left(\mathbf{d}_{1}^{T} \cdot \mathbf{d}_{1} - 1\right) \\ \frac{1}{2} \left(\mathbf{d}_{2}^{T} \cdot \mathbf{d}_{2} - 1\right) \\ \frac{1}{2} \left(\mathbf{d}_{3}^{T} \cdot \mathbf{d}_{3} - 1\right) \\ \mathbf{d}_{1}^{T} \cdot \mathbf{d}_{2} \\ \mathbf{d}_{3}^{T} \cdot \mathbf{d}_{1} \\ \mathbf{d}_{2}^{T} \cdot \mathbf{d}_{3} \end{bmatrix} = \mathbf{0} \in \mathbb{R}^{6}.$$
 (2.2)

Thus, overall the rigid body has 12 - 6 = 6 degrees of freedom, i.e. three translations and rotations each. To move the body between two discrete time nodes, say from time node n to n+1, we define incremental generalised coordinates or a kinematic update $\boldsymbol{u} \in \mathbb{R}^6$, $\boldsymbol{u}_{n+1} = \begin{bmatrix} \boldsymbol{u}_{\boldsymbol{\varphi}_{n+1}}, \ \boldsymbol{\theta}_{n+1} \end{bmatrix}$

$$\mathbf{q}_{n+1} = \mathbf{F}_{d} \left(\mathbf{u}_{n+1}, \ \mathbf{q}_{n} \right) = \begin{bmatrix} \varphi_{n} + \mathbf{u}_{\varphi_{n+1}} \\ \mathbf{R} \left(\widehat{\boldsymbol{\theta}_{n+1}} \right) \cdot \mathbf{d}_{1n} \\ \mathbf{R} \left(\widehat{\boldsymbol{\theta}_{n+1}} \right) \cdot \mathbf{d}_{2n} \\ \mathbf{R} \left(\widehat{\boldsymbol{\theta}_{n+1}} \right) \cdot \mathbf{d}_{3n} \end{bmatrix}$$
(2.3)

where $u_{\varphi_{n+1}}$ and θ_{n+1} are the in translation and rotation increments, respectively. Here, F_d is the discrete nodal or local reparameterisation, which satisfies the internal constraints Equation (2.2), see [BL06, Ley08]. In Equation (2.3), $R(\bullet)$ refers to a rotation matrix calculated for an axis-angle formulation, which can either be an exponential operator calculated from the Rodrigues' formula, see [Ley08, Rod40], or a Cayley transformation, see [Cay46].

2.1.1 Kinematic chains

Multiple rigid bodies, also called as links, can be coupled through constraints on the kinematic level to generate multibody chains, see [HD64, Ang13]. The coupling can be through either lower pairs i.e. contacting surfaces or higher pairs such as line or point contacts. Here, we present the general idea with respect to the expression for the chain configuration, the constraint vector and the kinematic update. The details and derivations have been already covered in [BL06, Ley08, LMO08, LOBMO10]. For a multibody system consisting of

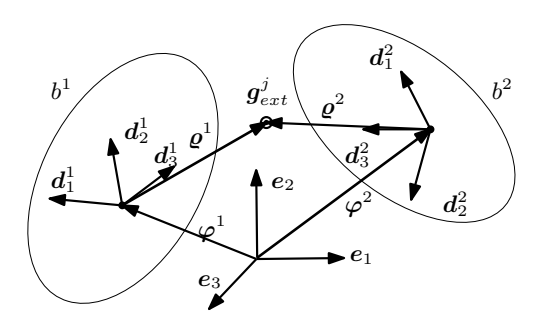


Figure 2.2: A generic kinematic chain example with two bodies having configurations \mathbf{q}^1 and \mathbf{q}^2 . Body b^1 is free to move in space and b^2 is connected to b^1 via joint j, described with holonomic constrains $\mathbf{g}_{ext}^j\left(\mathbf{q}^1,\mathbf{q}^2\right)=\mathbf{0}$. The bodies b^1 and b^2 are connected to the joint via vectors $\mathbf{\varrho}^1$ and $\mathbf{\varrho}^2$, respectively.

two bodies b^1 and b^2 with configurations q^1 and q^2 , respectively, the combined configuration vector is

$$q = \begin{bmatrix} q^1 \\ q^2 \end{bmatrix}. \tag{2.4}$$

Body b^1 is free to move in space and b^2 is connected to b^1 via joint j, described with holonomic constrains $g^j\left(q^1,q^2\right)=\mathbf{0}\in\mathbb{R}^{m_{ext}^j}$. On each body, we define a material point with local coefficients $\{\varrho_l^b\}_{l=1,2,3}$, whose location in the inertial frame is given as $\varphi^b+\varrho^b=\varphi^b+\sum_{l=1}^3\varrho_l^bd_l^b$. The joint is located

in the bodies b^1 and b^2 at ϱ^1 and ϱ^2 , respectively. The rigid body internal constraints and joint external constraints can be written in vector form as

$$\boldsymbol{g}^{j}(\boldsymbol{q}) = \begin{bmatrix} \boldsymbol{g}_{int}(\boldsymbol{q}) \\ \boldsymbol{g}_{ext}^{j}(\boldsymbol{q}) \end{bmatrix} \in \mathbb{R}^{12 + m_{ext}^{j}}$$
 (2.5)

where $g_{int}(q) = \left[g_{int}(q^1); g_{int}(q^2)\right]$, as in Equation (2.2). Also, the total number of degrees of freedom for the second body is now reduced from 6 to $r^j = 6 - m_{ext}^j$. This yields the size of the minimal coordinates or kinematic update $\mathbf{u}^j \in \mathbb{R}^{6+r^j}, \mathbf{u}_{n+1}^j = \left[\mathbf{u}_{\varphi_{n+1}}, \; \boldsymbol{\theta}_{n+1}, \; \boldsymbol{\theta}_{n+1}^j\right]$. Here, $\boldsymbol{\theta}_{n+1}^j \in \mathbb{R}^{r^j}$ is the kinematic update for the second body depending on the joint description j. The new location of the two bodies with respect to the increment \mathbf{u}^j is given through joint-specific nodal reparameterisation $\mathbf{q}_{n+1} = \mathbf{F}_d^j \left(\mathbf{u}_{n+1}^j, \mathbf{q}_n\right)$, which satisfies the constraints $\mathbf{g}^j(\mathbf{q}) = \mathbf{0}$.

In this work, we consider lower pairs, in particular revolute, universal and fixed joints to model different connections in the hand anatomy. The constraint vectors and their respective nodal reparameterisation, have been detailed in [BL06, LOBMO10, Maa14]. Furthermore, we introduce a new joint description in the following section, which anatomically captures the complex motion of the thumb joint.

2.1.1.1 Non-intersecting and non-orthogonal axes

The CMC and the MCP joints are modelled as a joint system with two axes which are non-intersecting and non-orthogonal (nino) to each other, as shown in Figure 2.3. It is a two degree of freedom joint with rotation axes n^1 and n^2 , where n^1 is fixed to the first body and n^2 is fixed to the second body, $n^1 = \sum_{I=1}^3 n^1_I d_I^1$, $n^2 = \sum_{I=1}^3 n^2_I d_I^2$. A vector $d = \varphi^2 - \varphi^1 + \varrho^2 - \varrho^1$ joins the points P_1 and P_2 which define the locations for axes n^1 and n^2 , respectively. This kinematic pair gives rise to a constraint vector with four external constraints between the rigid bodies with configuration vectors q^1

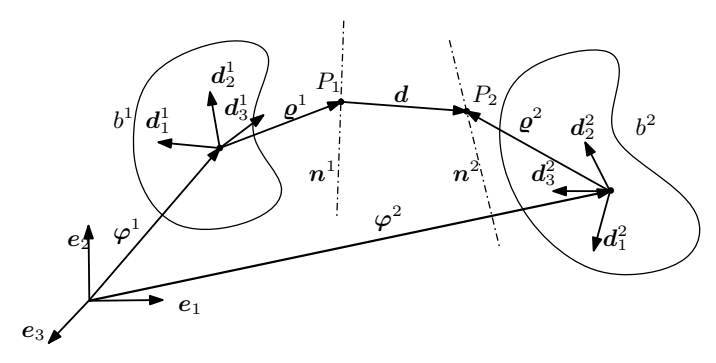


Figure 2.3: The kinematic pair with non-intersecting and non-orthogonal axes n^1 and n^2 between bodies b^1 and b^2 with configuration vectors q^1 and q^2 , respectively. The local vectors ϱ^1 and ϱ^2 define the locations of the points P_1 and P_2 for the axes n^1 and n^2 , while the vector d connects these points. $\{e_I\}_{I=1,2,3}$ is the spatially fixed orthonormal basis.

and q^2 as

$$g(q) = \begin{bmatrix} \|\varphi^{2} - \varphi^{1} + \varrho^{2} - \varrho^{1}\|^{2} - \|d\|_{initial}^{2} \\ n^{1} \cdot d - (n^{1} \cdot d)_{initial} \\ n^{2} \cdot d - (n^{2} \cdot d)_{initial} \\ n^{1} \cdot n^{2} - (n^{1} \cdot n^{2})_{initial} \end{bmatrix} = \mathbf{0} \in \mathbb{R}^{4}$$
(2.6)

wherein the first constraint keeps the distance between the points P_1 and P_2 constant. The second and third constraints keep the relative orientation of the non-intersecting and non-orthogonal axes n^1 and n^2 , with the vector d constant. The last constraint keeps the angle between the two axes constant. The kinematic update for the nino joint, through an increment $u_{n+1} = (u_{\varphi_{n+1}}, \theta_{n+1}, \theta_{n+1}^1, \theta_{n+1}^2, \theta_{n+1}^2) \in \mathbb{R}^8$, where θ_{n+1}^1 and θ_{n+1}^2 are the incremental

rotation around axes n^1 and n^2 , respectively, is given as

$$q_{n+1} = F_d(u_{n+1}, q_n) = \begin{bmatrix} \varphi_n + u_{\varphi_{n+1}} \\ R_1 \cdot d_{1n}^1 \\ R_1 \cdot d_{2n}^1 \\ R_1 \cdot d_{3n}^1 \\ \varphi_n + u_{\varphi_{n+1}} + R_1 \cdot (\varrho_n^1 + R_{11} \cdot (d_n - R_{12} \cdot \varrho_n^2)) \\ R_1 \cdot R_{11} \cdot R_{12} \cdot d_{1n}^2 \\ R_1 \cdot R_{11} \cdot R_{12} \cdot d_{2n}^2 \\ R_1 \cdot R_{11} \cdot R_{12} \cdot d_{3n}^2 \end{bmatrix}$$

$$(2.7)$$

where $R_1 = R\left(\widehat{\boldsymbol{\theta}_{n+1}}\right)$, $R_{11} = R\left(\widehat{\boldsymbol{\theta}_{n+1}^1\boldsymbol{n}_n^1}\right)$ and $R_{12} = R\left(\widehat{\boldsymbol{\theta}_{n+1}^2\boldsymbol{n}_n^2}\right)$, are rotation matrices for body b_1 , rotation about axes \boldsymbol{n}_n^1 and \boldsymbol{n}_n^2 , respectively.

2.2 Thumb anatomy

Although the motion between the bones occurs due to the tendons and the ligaments connecting the bones, the CMC and the MCP have often been mathematically approximated, see [CLCL81, Kap81], and implemented, see [WAC⁺09, SBML⁺14], in multibody models as universal joints, which means that the two axes of rotations are orthogonal and intersecting. Also, the flex-ext axis of the IP is assumed to be perpendicular to the sagittal plane of the thumb. However, a universal joint does not allow for the rotation of a single body along its longitudinal axis, which is observed in the thumb. Also in a study done by Valero-Cuevas, see [VCJT03], when compared with physical measurements, a thumb model with universal joints does not produce accurate forces at its tip in different postures. However, from the cadaveric measurements done by Hollister in [HBM⁺92] and [HGB⁺95], it was determined that the axes of the joints are neither orthogonal to each other or the bones nor intersecting with each other, as shown in Figure 2.4 (left). This was later confirmed by a number of studies through different methods, for example using optical measurements with surface markers, see [CM06, CMM⁺08], or MRI, see [CMM⁺10, SHSvdS14]. The CMC, MCP, IP flex-ext axes move with respect to the trapezium, the I MC, and the PP, respectively, while the CMC and MCP add-abd axes move with the I MC and the PP, respectively, see [HBM⁺92, HGB⁺95, GHB⁺95].

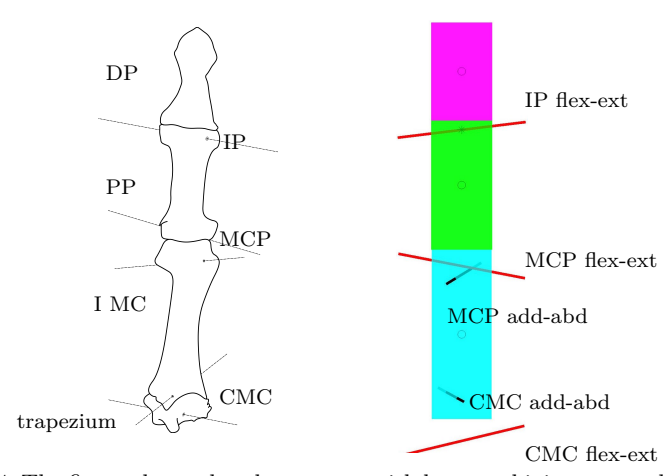


Figure 2.4: The figure shows thumb anatomy with bone and joint nomenclature and associated multibody model with anatomically correct locations and orientations for the MCP and the CMC, and IP axes.

2.3 Thumb multibody models

Following the anatomy, the thumb multibody model is shown in Figure 2.4 (right) consisting of three bodies. The IP joint is modeled as a revolute joint which has been described in [Ley08]. The CMC and the MCP joints are modelled as nino joints, as shown in Figure 2.3. The dimensions of the bones, i.e. the lengths and the radii of the bone in the radial and palmar directions and the locations and orientations of the axes of rotation of the joints have been obtained from cadaver studies from Santos, see [SVC06], and

from Hollister, see [HBM⁺92, HGB⁺95], respectively.

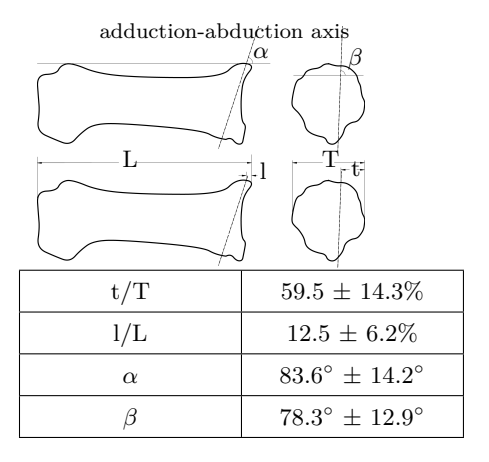


Figure 2.5: The CMC adduction-abduction axis, reproduced here from [HBM⁺92], is located in the head of the I MC (above). The orientation of the axis is defined with angles α and β . The location of the axis is defined with two length ratios t/T and l/L. The values are shown in the table (below), taken from [HBM⁺92].

To describe in detail the complexity of the measurement adopting to multibody models, an example is provided. Hollister in 1992 provided measurements for locations and orientations of the CMC axes from seven cadaver thumbs. The add-abd axis of the CMC, as shown in Figure 2.5 (left), is located in the head of the I MC. In the study, its location in two directions is specified with ratios (or percentages) which helps in scaling the model, while the orientation is reported with angles with respect to the anatomical planes. These measurements are described with a mean \pm standard deviation with a high anatomical variance, as shown in the table in Figure 2.5 (right), which gives little insight into the distribution of the values. To understand this variance, which depicts the natural variation in the human population, a Monte-Carlo study was performed by Santos, see [SVC06]. The study concluded that the anatomical variation converges to four multi-modal distributions of distinct

thumb models, shown in Figure 2.6 along with the base thumb model, named as types I, II, III and IV and described in Denavit-Hartenberg (D-H) notation, see [HD64]. These models have biomechanically distinct different kinematic features, namely in types I and IV, which comprise 65.2% of the population, the flex-ext axis of the MCP is distal to its add-abd axis, while it is opposite in the other 34.8%. The next level of differences involves the common normals, as described in the D-H notation, to the distal axis of the MCP and the flex-ext axis of the IP. Specifically, the common normal to the MCP distal axis points dorsally in type I and palmarly in type IV, while the common normal to the IP axis points proximally in type II and distally in type III. The base model is created using the mean values of all the above mentioned cadaver measurements.

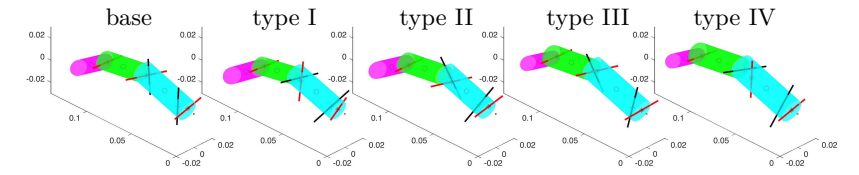


Figure 2.6: The different thumb models used to compare validation results. The base model is created with the mean values from cadaver measurements. The models named as types I, II, III and IV are taken from [SVC06]. The models have differences in the axes locations and orientations. For example, the base, type II and type III models have the MCP add-abd axis proximal with respect to its flex-ext, when compared with type I and type IV models.

2.3.1 Range of motion (RoM)

The RoM of the thumb has been investigated in a number of studies, e.g. [CLCL81, LKL⁺11]. However, they do not provide information such as location of the axes around which the angles are measured, or provide specification of the values of total flex-ext motion instead of only flexion or extension values (similar for add-abd angles), like in [CHM⁺15]. Furthermore, some use the assumption that the CMC and/or the MCP joints are modeled as universal joints and provide the Euler (cardan) angles ranges as done in [CLCL81, LKL⁺11].

Moreover, the studies which describe the axes do not provide the range of motion values. A comparative study of the RoM angles given by different researchers was done by [DIL13] and [CM06], for the maximum RoM, which is the maximum extent to which the bones can be moved.

However, we also have limits on the range of motion with respect to grasping activity. Grasping cannot be performed with the fingers in their extreme positions, for example, holding a basketball with a flat hand is not possible. To quantify the grasp RoM, a study was done [LKL+11] to measure the RoM for six grasps, namely tip pinch, palm pinch, lateral pinch, cylindrical grip, spherical grip and power grip. This RoM data was further post-processed, see [DIL13] to determine the grasp RoM limits. The values for the maximum RoM and grasp RoM are tabulated in Table 2.1.

-	rable 2:1: Italiges of motion for thamb Joines, taken from [B1215].										
	joint	maximum RoM		grasp RoM							
		flex-ext	add-abd	flex-ext	add-abd						
	CMC	-20° – 25°	$20^{\circ}-20^{\circ}$	-16° – 8°	$-10^{\circ}-15^{\circ}$						
	MCP	-60° – 10°	-15° – 15°	-24° – 23°	-23° – 6°						
	IP	-60° - 20°	-	-49° - 0°	_						

Table 2.1: Ranges of motion for thumb joints, taken from [DIL13].

2.4 Validation technique

For validation, there have been attempts to compare kinematics with a thumb modelled with universal joints, e.g. see [CMM⁺08], or to compare the Hausdorff distances in moving the first metacarpal from an initial posture to a particular posture, see [CMM⁺10]. Also, with the addition of muscles and tendons to the kinematic model, validation checks have been demonstrated with thumb kinetics, by comparing muscle moment arms, see [CM06], or the forces in the thumb tips for different postures, see [GM10]. Here, we compare the kinematic performance of the thumb, without resorting to marker-based physical measurements or introducing muscles in the model, rather which

quantifies the point cloud workspace of the thumb tip.

The point clouds are generated for all the five models for the maximum and the grasp RoMs. A quantitative indicator for the different point clouds of the thumb tip can simply be its encompassing volume. These volumes can be computed using α -shape, which is "a generalization of the convex hull of a finite set of points in the plane" (quoted from [EKS83]). For a set S in \mathbb{R}^3 , e.g. thumb tip end effector points, with a real constant $0 \le \alpha \le \infty$, an α -shape is the space generated by point pairs that can be touched by a sphere of radius α . Also, we have $\lim_{\alpha \to 0} S_{\alpha} = S$ and $\lim_{\alpha \to \infty} S_{\alpha} = \text{conv } S$, which is the convex hull for S. For detailed definition and explanation, see [EKS83].

2.4.1 RoM volume reduction for grasping

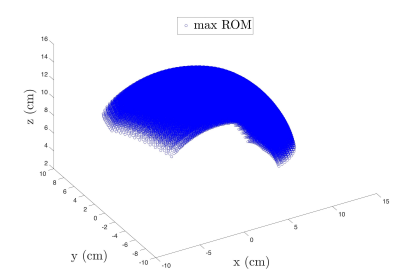


Figure 2.7: The point cloud for base model with maximum RoM.

To generate a point cloud, the thumb model is kinematically moved through all its DoFs and a set is created with the thumb tip points in all positions. The ranges of angles, as given in Table 2.1, for every DoF are partitioned with 13 divisions to obtain a set of kinematic inputs to achieve a unique position. A point cloud with the thumb tip points is created for the base model and maximum RoM, as shown in Figure 2.7. It is observed that the α -shape volume does not change significantly with more divisions.

Using an α -shape radius of 0.5, the point cloud is enveloped with a smooth α -shape with no holes and the volume of the α -shape is computed. The point clouds are created for the base model and the four anatomically variable models from [SVC06], which are converted from the D-H notation to the

director formulation. This conversion is done to employ these models for calculating internal rotation of the I MC, which is readily possible as the directors of the I MC form the necessary rotation matrix. The volumes are computed for both the maximum and grasp ranges of motion. The α -shapes from point clouds for all the thumb models with the maximum and grasp RoM are shown in Figure 2.8. The volumes for all the point clouds are tabulated in Table 2.2.

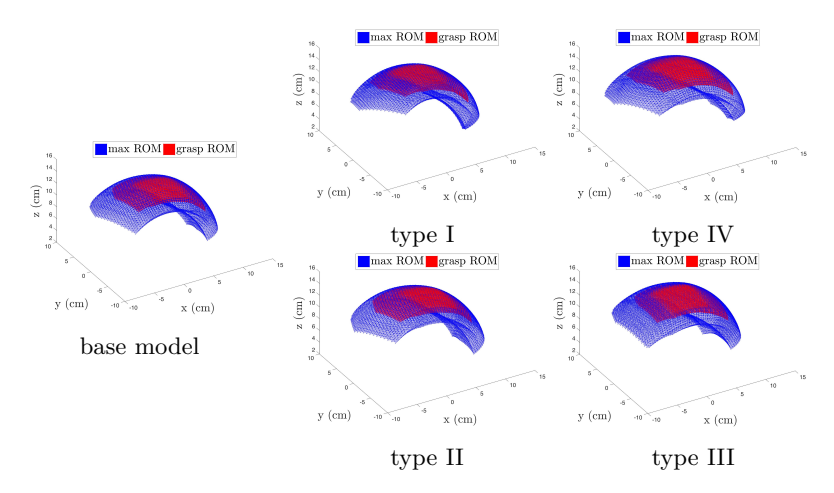


Figure 2.8: α -shapes for all models with maximum (blue) and grasp (red) RoM.

From Figure 2.8, the overall shapes of the α -shapes look similar, which suggests different individuals with different thumbs can cover a similar work-space shape and can perform similar functions. However, on closer observations, differences between the edges and corners are apparent. Also the grasp volume α -shapes lie completely within the maximum volume α -shapes for the respective model, while having different shape than the grasp RoM α -shapes for the other models. The differences are much more evident in the volume reduction for the two RoMs, which we evaluate as the percentage reduction in volume for grasp RoM with respect to maximum RoM to compare the different

models. It suggests individuals with model type III can cover more volume for grasping, however they are less effective in terms of the percentage of its grasping capacity, when compared to the model type I. A key observation from the values in Table 2.2 is that the volume and volume reduction for the base model lies within the range of anatomically variable models suggesting that a base model created with the mean values from cadaver measurements can be one realistic representation for a thumb model. The results from the

	type I	type II	type III	type IV	base
volume maximum RoM (cm ³)	319.9	390.8	508.0	493.1	386.3
volume grasp RoM (cm ³)	100.1	104.2	129.6	123.2	99.3
% reduction	68.7	73.3	74.45	75.0	74.3

Table 2.2: Volume reduction results for all models.

point cloud volumes suggest that the thumb model created using the mean values from cadaver measurements can be useful with regards to defining the reach of the thumb. The volume and volume reduction results for this base model lies within the ranges of anatomically variable models. This is important as it indicates that a thumb model with such measurements and dimensions has as much grasping capacity as any thumb from the human population.

2.5 Conclusions

The complex thumb anatomy is a major contributor to the human grasping capability. Its modelling through joint axes systems with non-intersecting and non-orthogonal axes allows for its typical opposition behaviour. The validation methodology makes use of a technique that does not require motion capture measurements. The validation results from the point cloud volumes suggest that the thumb model created using the mean values from cadaver measurements can be useful with regards to defining the reach of the thumb.

The volume and volume reduction results for this base model lies within the ranges of anatomically variable models. This is important as it indicates that a thumb model with such measurements and dimensions has as much grasping capacity as any thumb from the human population. In the following chapter, we focus on the development of grasping concepts, namely contact modelling and quality measures, from the robotics perspective and discuss its applications to the human context.

3 Human grasping

The topic of grasping is a well-researched area with multiple review articles published with regular fare, e.g. [Shi96, Bic00, AHK⁺09, SEKB12, BK19, GAI19, ZXZ⁺20]. The research is dominated, however, through a robotics point of view, wherein also the majority of key elements have been developed. These include the design of the manipulator or the hand, the outline of the object and surroundings, the control strategies, the cognition capability, the contact closure and grasp synthesis algorithms, and if prescribed, the task planning. Within the vast context, one can focus on human grasping with respect to the research fields such as the biomechanical hand model, the realization of force-closure grasps through well-defined contact models and measures for grading grasp postures. These fields can be further distilled to fundamental ideas such as the definition of a grasp, contact and force and velocity transmission between the hand the object.

A grasp is defined as a set of multi-point contacts on the surface of the object in order to control the possible movements of the object that can arise due to any external disturbance, see [Bic00, LMSB14, PT16]. A contact can be described as a unilateral joint that prevents a finger digit from penetrating into the object or maintaining constant relative motion between object and finger. The forces or moments transferred through the contact points depends on the contact surfaces, and its frictional and stiffness characteristics. Since there are numerous possibilities to obtain a grasp posture, there are some postures which are definitely better than others. This classification of a 'good' grasp requires certain measures based on the hand posture relative to the object. These measures are developed using two well-known matrices in grasping research, namely the grasp matrix and hand Jacobian.

This chapter gives a short introduction to the theoretical grasping concepts involved in this thesis and grasping research in general. In contrast to the minimal coordinates multibody formulation, such as Denavit-Hartenberg notation [HD64], used in many robotics and human grasping applications, see [PT16, MA04], the equations are presented in the director formulation.

The chapter begins with a few definitions and basic grasping theory in Section 3.1. It includes with setting up the equations for different contact models (Section 3.1.4, expressions for the grasp matrix and hand Jacobian matrices (Section 3.1.5) and concludes with the notion of form and force closures (Section 3.1.6). Thereafter, we discuss the grasp quality measures to evaluate the 'goodness' of a grasp in Section 3.2. Having discussed the grasp related topics, the chapter concludes with the description of the hand and object models in Sections 3.3 and 3.4 that are used in the grasping optimal control setup in this thesis. Certain sections of this chapter, in particular the derivation of the grasp matrix and hand Jacobian matrices, have been reproduced from [PRL22].

3.1 Grasping Theory

This section introduces the basic terminology concerning contact mechanics, in particular the concepts and equations for twists and wrenches. Consider a rigid object O whose position and orientation is described with configuration $\mathbf{q}^O = \left[\boldsymbol{\varphi}^{O,T}, \mathbf{d}_1^{O,T}, \mathbf{d}_2^{O,T}, \mathbf{d}_3^{O,T}\right]^T$ with respect to an inertial orthonormal basis $\{e_I\}_{I=1,2,3}$, as shown in Figure 3.1. The object is in contact with a finger digit a with configuration \mathbf{q}^a at point A. At this point, we describe an orthonormal frame consisting of three vectors, namely, a direction \mathbf{n}^A normal to and pointing outwards from the object surface, and two orthogonal vectors \mathbf{t}^A and \mathbf{o}^A , in the tangential plane T to the object surface at the contact point. Altogether, $[\mathbf{n}^A, \mathbf{t}^A, \mathbf{o}^A]$ form the contact point frame.

The digit a is part of a kinematic chain, representing a finger in a hand, as shown in Figure 3.2. Let $q \in \mathbb{R}^l$ be the hand redundant configuration vector, as described for a kinematic chain in Equation (2.4). The hand has n_j joints. Every joint can have either one (revolute), two (nino or cardan) or three (spherical) degrees of freedom. Due to this, the configuration q of the hand is restricted to a constraint manifold depending on the joint and rigid body holonomic constraints q (q) = $0 \in \mathbb{R}^m$.

For every joint description, we can assign angular velocities or twists. The

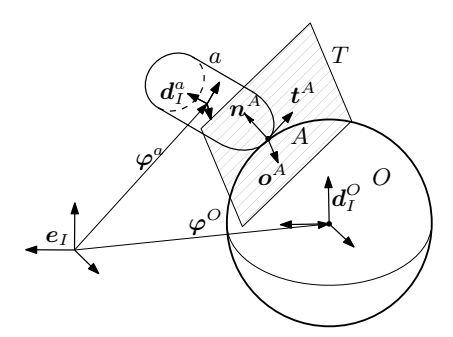


Figure 3.1: An object O with configuration \boldsymbol{q}^O is in contact with a finger digit a with configuration \boldsymbol{q}^a at point A. $\left[\boldsymbol{n}^A,\,\boldsymbol{t}^A,\,\boldsymbol{o}^A\right]$ forms a orthonormal frame at the contact point with \boldsymbol{n}^A as outward normal to the object surface and $\left[\boldsymbol{t}^A,\,\boldsymbol{o}^A\right]$ spans the tangential plane T.

combined twist vector for all joints can be written as

$$\nu(t) = \begin{bmatrix} \nu_1 \\ \nu_2 \\ \dots \\ \nu_{n_j-1} \\ \nu_{n_i} \end{bmatrix} \in \mathbb{R}^{l-m}$$
(3.1)

where l-m is the minimal number of degrees of freedom for the hand. Similar to twist, we can assign control torques to every joint and form the vector of controls, as

$$\boldsymbol{\tau}(t) = \begin{bmatrix} \boldsymbol{\tau}_1 \\ \boldsymbol{\tau}_2 \\ \dots \\ \boldsymbol{\tau}_{n_j - 1} \\ \boldsymbol{\tau}_{n_j} \end{bmatrix} \in \mathbb{R}^{l - m}$$
(3.2)

We define a matrix $P(q) \in \mathbb{R}^{l \times (l-m)}$, which maps the twists, or minimal

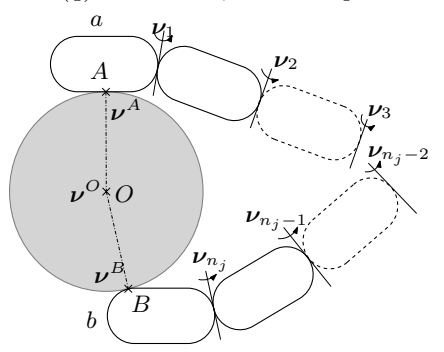


Figure 3.2: A two dimensional view of an object O in contact with two digits a and b of a hand at points A and B, respectively.

velocities in the constraint manifold tangent space to the hand configuration redundant velocity \dot{q} , as

$$\dot{q} = P \cdot \nu. \tag{3.3}$$

This matrix P is the null-space matrix for the kinematic hand chain, see [LMO08, BL06]. For the object, we describe the twist $\nu^O \in \mathbb{R}^6$ as the vector of its translational and angular velocities. The object twist $\nu^O \in \mathbb{R}^6$ is related to its redundant coordinate velocity through the object null-space matrix $P^O \in \mathbb{R}^{12 \times 6}$ via

$$\dot{\mathbf{q}}^O = \mathbf{P}^O \cdot \mathbf{\nu}^O. \tag{3.4}$$

The twists at the contact points A and B are given as $\boldsymbol{\nu}^C = \{\boldsymbol{\nu}^A, \boldsymbol{\nu}^B\}$. Also, consider the object is acted upon by an external force $\tau_t \in \mathbb{R}^3$ and a moment $\tau_\theta \in \mathbb{R}^3$. These are combined into a vector called as the external wrench $\tau_{ext} = \begin{bmatrix} \tau_t^T, \ \tau_\theta^T \end{bmatrix}^T \in \mathbb{R}^6$. In Figure 3.2 the object is grasped through the forces and twists are transmitted from the two digits of the hand through the contact points A and B. The twists at points A and B, $\boldsymbol{\nu}^A$ and $\boldsymbol{\nu}^B$ respectively, are expressed in the contact point frames in the respective points, i.e. the translational velocities are expressed along contact frame directions and the angular velocities are about these directions at points A and B. Similarly, the contact forces and moments or collectively, contact wrenches

 τ^A and τ^B , are also the forces along and moments in the contact frames. The total wrench τ_{app} acting on the object through the contact points is the linear combination of the individual wrenches, i.e.

$$\tau_{app} = \mathbf{R}^{A,T} \cdot \boldsymbol{\tau}^A + \mathbf{R}^{B,T} \cdot \boldsymbol{\tau}^B, \tag{3.5}$$

where $\mathbf{R}^P = \begin{bmatrix} \mathbf{n}^P, \mathbf{t}^P, \mathbf{o}^P \end{bmatrix}$ is the contact point frame at contact point P. For the object to be have complete contact closure, i.e. the grasp should not break under the influence of any external wrench τ_{ext} , the condition to be satisfied is

$$\tau_{app} = \tau_{ext}. \tag{3.6}$$

Here, the external wrench represents all possible forces and moments, such as object weight, inertia force and other external forces. The condition Equation (3.6) corresponds to the fact that in complete contact closure the translational and angular velocities on the hand and the object at the contact points are equal. The force and velocity transmission though the contact frames depends on the type of contact model used to close the grasp. We discuss the widely used models in literature in the following subsections.

3.1.1 Point contact without friction (PwoF)

As the name suggests, this model has a one point of contact between two rigid body surfaces, such as a single finger of the hand and the object surfaces. This contact prevents the relative motion between them along the line normal to the object surface. The normal acts as the line of force and velocity transfer. The PwoF model allows for sliding due to the lack of friction due to the absence of any force in the tangential plane. It is commonly used in robotics with small contact patches and slippery surfaces [PT16, LMSB14], however, does not represent real contact situations [Cut89, LBR00].

We now describe the equations involved with the PwoF model with respect to the contact point locations, kinematic constraints and the contact forces, using Figure 3.3. We extend the setup described in Figure 3.1 and give the kinematic description of the contact point A as

$$\varphi^{a} + \varrho^{A,a} = \varphi^{a} + \sum_{I=1}^{3} \varrho_{I}^{A,a} d_{I}^{a}$$

$$(3.7)$$

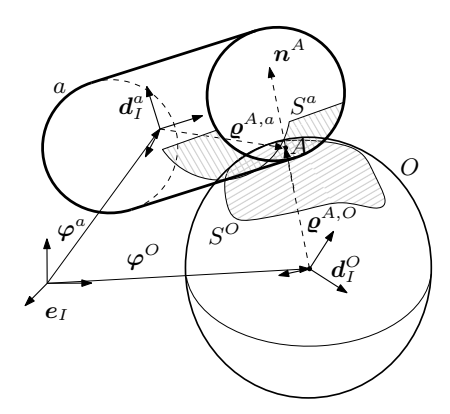


Figure 3.3: Kinematic representation of a point contact without friction contact model between digit a and object O. The vectors $\boldsymbol{\varrho}^{A,a}$ and $\boldsymbol{\varrho}^{A,O}$ connect the mass centres of the digit and object, respectively, to the contact point A. The dashed lines represent that the contact points may move within areas S^a and S^O on the digit and object, respectively, where the contact is to be maintained.

through coefficients $\{\varrho_I^{A,a}\}_{I=1,2,3}$ in the digit body-axis system for digit a. This location is shared by the object and is represented in the object body-axis system through coefficients $\{\varrho_I^{A,O}\}_{I=1,2,3}$ as

$$\varphi^{O} + \varrho^{A,O} = \varphi^{O} + \sum_{I=1}^{3} \varrho_{I}^{A,O} d_{I}^{O}$$

$$(3.8)$$

The coefficients $\{\varrho_I^{A,a}\}_{I=1,2,3}$ and $\{\varrho_I^{A,O}\}_{I=1,2,3}$ may change under the influence of an external wrench even while maintaining the contact. This is due to the absence of friction to prevent sliding between the surfaces. To maintain contact between the digit and the object, we enforce three sets of constraints. The first two restrict the location of the contact points within their respective body-axis system, while the third constraint maintains zero distance between the two points. We first prescribe specific areas S^a and S^O on the digit and object, respectively, where the contact is to be maintained. These

limits are mathematically written as holonomic equality g_{ϱ} and inequality h_{ϱ} constraints

$$g_{\varrho}^{A,a}\left(\varrho_{1}^{A,a},\varrho_{2}^{A,a},\varrho_{3}^{A,a}\right) = 0, \qquad h_{\varrho}^{A,a}\left(\varrho_{1}^{A,a},\varrho_{2}^{A,a},\varrho_{3}^{A,a}\right) \leq 0$$
 (3.9)

$$\begin{aligned} & \boldsymbol{g}_{\varrho}^{A,a} \left(\varrho_{1}^{A,a}, \varrho_{2}^{A,a}, \varrho_{3}^{A,a} \right) = \boldsymbol{0}, \qquad \boldsymbol{h}_{\varrho}^{A,a} \left(\varrho_{1}^{A,a}, \varrho_{2}^{A,a}, \varrho_{3}^{A,a} \right) \leq \boldsymbol{0} \\ & \boldsymbol{g}_{\varrho^{O}}^{A,O} \left(\varrho_{1}^{A,O}, \varrho_{2}^{A,O}, \varrho_{3}^{A,O} \right) = \boldsymbol{0}, \qquad \boldsymbol{h}_{\varrho^{O}}^{A,O} \left(\varrho_{1}^{A,O}, \varrho_{2}^{A,O}, \varrho_{3}^{A,O} \right) \leq \boldsymbol{0}. \end{aligned} \tag{3.9}$$

These constraints are described using the surfaces for the primitives used to represent the digits and the objects. Additionally, the following holonomic equality constraint is to be satisfied,

$$g_{PwoF}\left(\boldsymbol{q}^{a},\boldsymbol{q}^{O},\varrho_{I}^{A,a},\varrho_{I}^{A,O}\right) = \|\boldsymbol{\varphi}^{a} + \boldsymbol{\varrho}^{A,a} - \left(\boldsymbol{\varphi}^{O} + \boldsymbol{\varrho}^{A,O}\right)\| = 0 \in \mathbb{R}$$
 (3.11)

With Equations (3.9) and (3.10), the contact points lie on the finger and object surfaces, respectively, while with Equation (3.11), the two points stay coincident.

In constraint-based formulation of dynamics, a holonomic equality constraint is accompanied by a constraint force, evaluated as the multiplication of the transposed constraint Jacobian G_{PwoF} with Lagrange multipliers $\lambda \in \mathbb{R}$ (or wrench intensities, as described in [PT16]). The forces on the hand and the object are equal and opposite in nature and are evaluated as

$$\mathbf{f}^{a} = \mathbf{G}_{pwof}^{a,T} \cdot \lambda = \left(\frac{\partial g_{PwoF}}{\partial \mathbf{q}^{a}}\right)^{T} \cdot \lambda \in \mathbb{R}^{12}$$
 (3.12a)

$$\boldsymbol{f}^{O} = \boldsymbol{G}_{pwof}^{O,T} \cdot \lambda = \left(\frac{\partial g_{PwoF}}{\partial \boldsymbol{q}^{O}}\right)^{T} \cdot \lambda \in \mathbb{R}^{12}$$
 (3.12b)

The force on the object f^O can be transformed into a six-dimensional wrench $\boldsymbol{\tau}^O \in \mathbb{R}^6$ using the null-space matrix for a single rigid body, see [Ley11], as

$$\boldsymbol{\tau}^{O} = \boldsymbol{P}^{O,T} \cdot \boldsymbol{f}^{O}. \tag{3.13}$$

This transformation is analogous to the twist-redundant velocity transform used in Equation (3.4).

For the forces to be physically viable, they have to be acting on their respective bodies. For example, if n^A is the outward pointing normal to the object surface, then the constraint reads

$$h_{normal} = \boldsymbol{n}^{A,T} \cdot \boldsymbol{f}^O \le 0 \in \mathbb{R}$$
 (3.14)

for the force to be pushing on the object.

3.1.2 Hard contact model

The hard contact model is used to model contact between rigid bodies with a significant amount of friction with a very small contact patch [PT16, LMSB14]. In contrast to the PwoF model, the wrenches and velocities are constrained along all the three directions in the contact point frame, which includes frictional forces in the plane tangential to the object surface. Considering an appropriate amount of friction, the contact points do not slide on the finger and object surfaces. Therefore, to maintain contact closure under an external wrench, the contact points need to satisfy the following constraint which reads

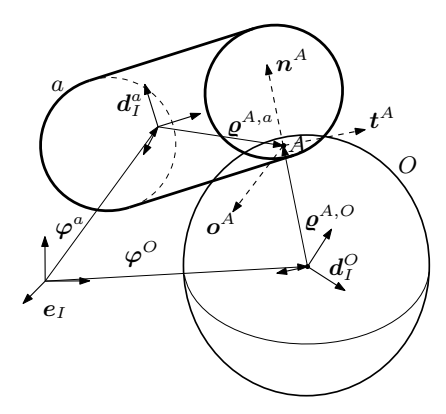


Figure 3.4: Kinematic representation of a hard contact model between digit a and object O, extending the PwoF model from Figure 3.3. The contact point vectors $\boldsymbol{\varrho}^{A,a}$ and $\boldsymbol{\varrho}^{A,O}$ are fixed, while the orientations between the digit and the object along the directions (represented by dashed lines) in the contact point frame $[\boldsymbol{n}^A, \boldsymbol{t}^A, \boldsymbol{o}^A]$ are free.

$$g_{hard}\left(q^{a}, q^{O}\right) = \varphi^{a} + \varrho^{a} - (\varphi^{O} + \varrho^{O}) = 0 \in \mathbb{R}^{3}$$
 (3.15)

In the kinematic chain of rigid bodies formulation, such a constraint is the description for a spherical joint between two bodies [BL06, Ley08]. Also, this equation is simply the vector form of Equation (3.11).

The inclusion of friction is possible through a number of models, though the use of the classical Coulomb's model is very common. This model is independent of the velocity and the contact area and uses a constant called as the coefficient of friction μ_{hard} to constrain the forces in the tangential plane relative to the normal force component, see Figure 3.5. The wrench

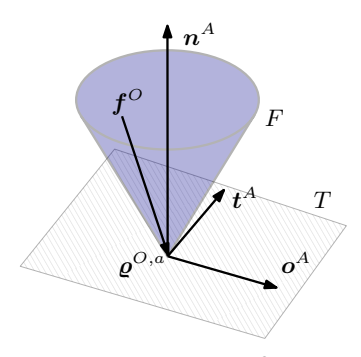


Figure 3.5: The representation of the force f^O lying inside a friction cone Fat contact point $\rho^{O,a}$.

intensities or Lagrange multipliers in this model is a vector $\lambda \in \mathbb{R}^3$. Similar to Equation (3.12b), the contact force applied by the hand on the object is calculated as $f^O = G_{hard}^{O,T} \cdot \lambda = \left(\frac{\partial g_{hard}}{\partial q^O}\right)^T \cdot \lambda$.

calculated as
$$m{f}^O = m{G}_{hard}^{O,T} \cdot m{\lambda} = \left(rac{\partial m{g}_{hard}}{\partial m{q}^O}
ight)^T \cdot m{\lambda}.$$

From Equation (3.15), we can evaluate the Jacobian

$$G_{hard}^{O} = \begin{bmatrix} -I & -\varrho_1^{O}I & -\varrho_2^{O}I & -\varrho_3^{O}I \end{bmatrix} \in \mathbb{R}^{12 \times 3}$$
 (3.16)

where I is the identity matrix. This leads the contact forces acting on the object to be simply the negative of the components of the Lagrange multipliers $-\lambda = -[\lambda_1; \lambda_2; \lambda_3]$, expressed in the inertial reference system. Correspondingly, the contact force from the object to the hand is the vector λ , showing that the contact forces work as an action-reaction pair. Using the Coulomb's law, the contact force is constrained to lie in the friction cone F

$$h_{fric,hard} := \| \left[\mathbf{I} - \mathbf{n}^A \otimes \mathbf{n}^A \right] \cdot (-\boldsymbol{\lambda}) \| \le \mu_{hard} \| \mathbf{n}^{A,T} \cdot (-\boldsymbol{\lambda}) \|$$
 (3.17)

where $\mu_{hard} \in \mathbb{R}$ is the coefficient of static friction and n^A is the outward normal.

Remark 1 Equation (3.15) can also be reformulated to determine one set of the contact point coefficients, provided the digit and object configurations along with the other contact point coefficients are known. For example, if the contact point coefficients for the digit are prescribed, then the object contact point coefficients can be determined by,

$$\{\varrho_I^O\}_{I=1,2,3} = \begin{bmatrix} \boldsymbol{d}_1^O, \ \boldsymbol{d}_2^O, \ \boldsymbol{d}_3^O \end{bmatrix}^T \cdot (\boldsymbol{\varphi}^a + \boldsymbol{\varrho}^a - \boldsymbol{\varphi}^O)$$
 (3.18)

This reformulation is useful in the grasping optimal control setup and will be utilized in Chapter 4.

3.1.3 Soft contact model

The soft contact model is a direct extension to the hard contact model. This model is a representation for contact between bodies with deformable surfaces e.g. the human hand, see [LMSB14, PT16, CLA07]. In this case, there exists a contact patch in the tangent plane to the object surface normal, which can generate a significant amount of friction restricting the rotation about the normal, as shown in Figure 3.6. This implies that only relative rotation about two directions in the tangential plane is permissible, which mechanically resembles a universal or cardan joint. We recall that the contact point frame $\mathbf{R}^a = \begin{bmatrix} \mathbf{n}^A, \ \mathbf{t}^A, \ \mathbf{o}^A \end{bmatrix}$ is composed of the normal vector \mathbf{n}^A and two vectors \mathbf{t}^A and \mathbf{o}^A spanning the tangential plane.

The constraint vector for the soft contact model uses the hard contact constraint from Equation (3.15) to constrain the relative translation while adding another constraint to constrain one rotation about the normal direction. It is formulated as

$$g_{soft}\left(\boldsymbol{q}^{a}, \boldsymbol{q}^{O}\right) = \begin{bmatrix} \boldsymbol{\varphi}^{a} + \boldsymbol{\varrho}^{a} - \left(\boldsymbol{\varphi}^{O} + \boldsymbol{\varrho}^{O}\right) \\ \boldsymbol{t}^{a} \left(\boldsymbol{q}^{a}\right)^{T} \cdot \boldsymbol{o}^{a} \left(\boldsymbol{q}^{O}\right) \end{bmatrix} = \mathbf{0} \in \mathbb{R}^{4}$$
(3.19)

The vector $\mathbf{t}^a\left(\mathbf{q}^a\right)$ is expressed with coefficients $\{t_I^a\}_{I=1,2,3}$ multiplied with digit directors $\{\mathbf{d}_I^a\}_{I=1,2,3}$. Similarly, the vector $\mathbf{o}^a\left(\mathbf{q}^O\right)$ is expressed with coefficients $\{o_I^a\}_{I=1,2,3}$ and object configuration directors $\{\mathbf{d}_I^O\}_{I=1,2,3}$. The

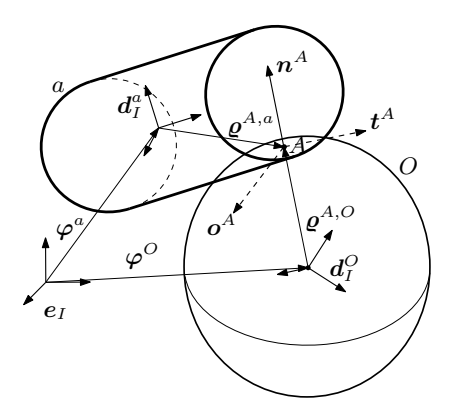


Figure 3.6: Kinematic representation of a soft contact model between digit a and object O, extending the PwoF and hard contact models from Figure 3.3 and Figure 3.4, respectively. Along with fixing the contact point vectors $\boldsymbol{\varrho}^{A,a}$ and $\boldsymbol{\varrho}^{A,O}$, the rotation around the normal \boldsymbol{n}^A is constrained.

dot product $t^{a}\left(q^{a}\right)^{T}\cdot o^{a}\left(q^{O}\right)$ is constrained to zero to prohibit the relative rotation between the digit and object surface about n_{a} .

The wrench intensities used to describe the contact force are the Lagrange multipliers $\lambda \in \mathbb{R}^4$. Similar to hard contact model, the contact force applied by the digit on the object is calculated as $f^O = G^{O,T}_{soft} \cdot \lambda$. It is transformed into a force-moment vector again through $\boldsymbol{\tau}^O = P^T \cdot f^O$ with $\boldsymbol{\tau}^O = \begin{bmatrix} \boldsymbol{\tau}_t^T, \boldsymbol{\tau}_\theta^T \end{bmatrix}^T$, where $\boldsymbol{\tau}_t \in \mathbb{R}^3$ and $\boldsymbol{\tau}_\theta \in \mathbb{R}^3$ are the force and moment components, respectively. The first three rows of the constraint Jacobian $G^O_{soft} = \begin{pmatrix} \frac{\partial g_{soft}}{\partial q^O} \end{pmatrix}^T \in \mathbb{R}^{4 \times 12}$ are the same as for the hard contact model, i.e. $\boldsymbol{\tau}_t = -\lambda$. However, since the direction of the surface normal \boldsymbol{n}^A is a function of the object shape, the Jacobian of the fourth constraint is relatively complicated. For this purpose, $\boldsymbol{\tau}_\theta$ is transformed from the inertial frame to the contact point frame, i.e. $\boldsymbol{\tau}_\theta^a = \boldsymbol{R}^a \cdot \boldsymbol{\tau}_\theta$. Thereafter, the Coulomb's law is applied using $[\boldsymbol{\tau}_\theta^a]_{\boldsymbol{n}^a}$, which is the component of the moment along the normal direction, in addition to the

hard contact model from Equation (3.17)

$$h_{fric,soft} := \frac{\| \left[\boldsymbol{I} - \boldsymbol{n}^{A} \otimes \boldsymbol{n}^{A} \right] \cdot \boldsymbol{\tau}_{t} \|}{\mu_{hard}} + \frac{\| \left[\boldsymbol{\tau}_{\theta}^{a} \right]_{\boldsymbol{n}^{A}} \|}{\mu_{soft}} \leq \| \boldsymbol{n}^{A,T} \cdot (-\boldsymbol{\lambda}) \| \quad (3.20)$$

where μ_{hard} and μ_{soft} are the coefficients of friction for the hard and soft components of the applied force, respectively [KLB16].

The representation here can be improved if actual deformable bodies are used, which represent in detail the contact patch area and accompanying stresses. For example, the use of the elastic foundation models [Ker84, CMA05] and finite element models [PGFESB⁺08] has been demonstrated to model more accurate contact mechanics in biomechanical systems. However, with such descriptions, the problem complexity increases to a great extent, especially in the optimal control framework.

3.1.4 Combined contact constraints vector

Using the equations for the individual contact constraints from the subsections above, we represent the combined vector for contact constraints $g_C(q,q^O) = \mathbf{0} \in \mathbb{R}^{p \cdot n_c}$ when grasping with n_c contact points using the complete hand, as

$$g_{C}\left(q,q^{O}\right) = \begin{bmatrix} g_{1}\left(q,q^{O}\right) \\ g_{2}\left(q,q^{O}\right) \\ g_{3}\left(q,q^{O}\right) \\ \vdots \\ g_{n_{c}}\left(q,q^{O}\right) \end{bmatrix} = \mathbf{0}, \tag{3.21}$$

Here, $g_i\left(\mathbf{q},\mathbf{q}^O\right)$ for $i=1,\ldots,n_c$ can be either of three Equations (3.11), (3.15) or (3.19) representing either of the three contact models. For the sake of brevity, the contact point coefficients $\boldsymbol{\varrho} \in \mathbb{R}^{3 \cdot n_c}, \boldsymbol{\varrho}^O \in \mathbb{R}^{3 \cdot n_c}$ from Equation (3.11) are omitted, where $\boldsymbol{\varrho}$ and $\boldsymbol{\varrho}^O$ consists of the n_c contact point coefficients with respect to the hand and object, respectively. The factor p relates to the size of the contact constraints, i.e. p=1,3 or 4 for PwoF,

hard or soft contact model, respectively. The wrench intensities are similarly ordered to form a combined contact wrench vector $\lambda_C \in \mathbb{R}^{p \cdot n_c}$

$$\boldsymbol{\lambda}_{C} = \begin{bmatrix} \boldsymbol{\lambda}_{1} \\ \boldsymbol{\lambda}_{2} \\ \boldsymbol{\lambda}_{3} \\ \vdots \\ \boldsymbol{\lambda}_{n_{c}} \end{bmatrix} . \tag{3.22}$$

The gradients with respect to the hand and object configurations are then simply evaluated as,

$$G_{C}\left(q,q^{O}\right) = \begin{bmatrix} \left(\frac{\partial g_{1}\left(q,q^{O}\right)}{\partial q}\right) \\ \left(\frac{\partial g_{2}\left(q,q^{O}\right)}{\partial q}\right) \\ \vdots \\ \left(\frac{\partial g_{n_{c}}\left(q,q^{O}\right)}{\partial q}\right) \end{bmatrix} \text{ and } G_{C}^{O}\left(q,q^{O}\right) = \begin{bmatrix} \left(\frac{\partial g_{1}\left(q,q^{O}\right)}{\partial q^{O}}\right) \\ \left(\frac{\partial g_{2}\left(q,q^{O}\right)}{\partial q^{O}}\right) \\ \vdots \\ \left(\frac{\partial g_{n_{c}}\left(q,q^{O}\right)}{\partial q^{O}}\right) \end{bmatrix},$$

$$(3.23)$$

respectively. Following on, the contact forces acting on the hand and the object systems, respectively, get evaluated as

$$\mathbf{f}_C = \mathbf{G}_C^T \cdot \boldsymbol{\lambda}_C = \sum_{i=1}^{n_C} \left[\mathbf{G}_i^T \cdot \boldsymbol{\lambda}_i \right], \tag{3.24}$$

$$\mathbf{f}_C^O = \mathbf{G}_C^{O,T} \cdot \boldsymbol{\lambda}_C = \sum_{i=1}^{n_c} \left[\mathbf{G}_i^{O,T} \cdot \boldsymbol{\lambda}_i \right]. \tag{3.25}$$

The complete constraint vector is used in the following to set up relations for grasp analysis.

3.1.5 Grasp matrix and hand Jacobian

The overall behaviour of the hand and object systems during grasping is analysed using two matrices, namely the grasp matrix G_{ν} and the hand Jacobian H_{ν} , see [PT16]. These matrices characterize the velocity kinematics and force transmission properties between the fingers and the object through the contact points, using the terms introduced in Figure 3.2. The grasp matrix $G_{\nu}^{T} \in \mathbb{R}^{p \cdot n_{c} \times 6}$ maps the object twist ν^{O} to the twist at the contact points ν^{C} , i.e. $\nu^{C} = G_{\nu}^{T} \cdot \nu^{O}$, for a closed contact with n_{c} points. Correspondingly, the wrenches λ_{C} applied at the object contact points get transformed to a collective wrench or applied torque as $\tau_{app} = G_{\nu}\lambda_{C}$. The hand Jacobian matrix $H_{\nu} \in \mathbb{R}^{p \cdot n_{c} \times (l-m)}$ maps the joint twists ν to ν^{C} and we have the relation $\nu^{C} = H_{\nu} \cdot \nu$. Also, in the wrench space the hand Jacobian transforms the contact wrenches to the joint torques applied, as $\tau = H_{\nu} \cdot \lambda_{C}$. The relations between G_{ν} , G_{ν}^{T} , H_{ν} , and H_{ν}^{T} is summarised in Figure 3.7. Hand

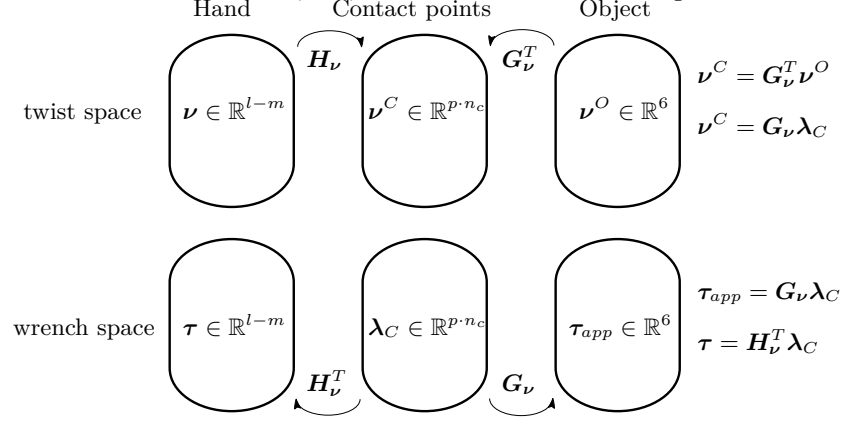


Figure 3.7: The relationship between the object and hand twist and force/torque spaces through the G_{ν} , G_{ν}^{T} , H_{ν} , and H_{ν}^{T} matrices, reproduced from [RS14].

The method to derive the expressions for these matrices has been detailed in a number of places, most notably in [PT16], which simply put is quite cumbersome and tedious, though mechanical. In the director formulation, we use a similar idea to derive the expressions using the constraint that the contact closure is fulfilled in the twist space,

$$(\nu^C)^{\text{hand}} - (\nu^C)^{\text{object}} = 0$$

$$H_{\nu} \cdot \nu - G_{\nu}^T \cdot \nu^O = 0.$$
(3.26)

Taking a time derivative of the constraint vector Equation (3.21), which is enforced during the manipulation phase, and using from Equation (3.3) $\mathbf{q} = \mathbf{P} \cdot \mathbf{\nu}$ and Equation (3.4) $\mathbf{q}^O = \cdot \mathbf{P}^O \cdot \mathbf{\nu}^O$, we get

$$\frac{d}{dt}g_{C}(q, q^{O}) = \frac{\partial g_{C}}{\partial q} \cdot \dot{q} + \frac{\partial g_{C}}{\partial q^{O}} \cdot \dot{q}^{O} = \frac{\partial g_{C}}{\partial q} \cdot P \cdot \nu + \frac{\partial g_{C}}{\partial q^{O}} \cdot P^{O} \cdot \nu^{O} = 0$$
which is equivalent to $H_{\nu} \cdot \nu + (-G_{\nu}^{T}) \cdot \nu^{O} = 0$

with
$$\mathbf{H}_{\nu} = \left(\frac{\partial \mathbf{g}_{C}\left(\mathbf{q}, \mathbf{q}^{O}\right)}{\partial \mathbf{q}} \cdot \mathbf{P}\right)$$
 (3.27)

$$G_{\nu} = -\left(\frac{\partial g_{C}\left(q, q^{O}\right)}{\partial q^{O}} \cdot P^{O}\right)^{T}$$
(3.28)

and consequently, we obtain the simple expressions for the hand Jacobian H_{ν} (Equation (3.27)) and the grasp matrix G_{ν} (Equation (3.28)).

3.1.6 Form and force closure

Once a multi-point grasp closure has been achieved, the first step in grasp analysis is to evaluate its closure properties, in essence to understand how many contact points with a particular contact model are required to completely constrain an object. These questions are answered through the concepts of form and force closure that have been discussed in a number of contributions and text books, for example, [Bic94, BFH99, BFH03, PT16, CLA07, SKG12, Zhe19] to name a few. To describe briefly, we summarise the explanation from [BFH03, PT16].

Consider a two-dimensional example of a box, which is grasped in such a way that it is completely immobilised using the PwoF contact model, as shown

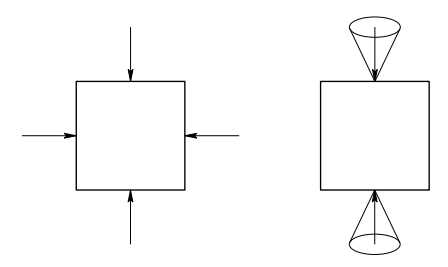


Figure 3.8: Left: Form closure for a two-dimensional object achieved with four contact points, each modelled with PwoF contact model. Right: Force closure for the similar object possible with two contact points modelled with hard contact model.

in Figure 3.8 (left). This implies that the object does not break contact due to the application of external wrench in any direction and of any magnitude. Such a condition would be achievable through the use of four contact points, as shown by Reuleaux, see [Reu76]. This condition is termed as form closure. In three-dimensions, seven contact points are needed to achieve form closure for an object with six degrees of freedom [Som00]. In practical scenarios, this can be explained with a human grasp performed with the fingers along with the palm to restrict the complete motion of the object. Such a grasp is also termed as a power grasp, see [Lan62, PT16]. However, in human and robotic grasping, closure with lesser number of contact points is performed with the help of friction, e.g., while performing precision grasps [Lan62]. In particular, for the same object, as shown in Figure 3.8 (right), two contacts with hard fingers will resist external wrenches along all possible directions, which can be countered with applied forces lying inside the friction cone defined by the coefficient of static friction, see [MC94, Ngu88, Che06]. This condition is termed as force closure. In three dimensions, grasp configurations with three hard contacts or two soft contacts are required to achieve force closure. It is also a very active research area, wherein different methods are analysed which can generate optimal force closure grasps, for example one can read [BFH99, BFH03, RB96, Ngu88, Zhe19, Bic00, MA04, ZW03, ZQ06].

3.2 Grasp quality measures

In grasp planning, it is possible to obtain different of configurations with a particular number of contact points for a specific object, each with force closure. To adjudicate whether a certain grasp is better than another, quality measures have been developed to determine the 'goodness' of a particular grasp. The quality measures have been developed using the concepts covered in this chapter, namely, the grasp matrix [LS88, KOYS01], the hand Jacobian [Shi96, SC82], the grasp wrench space [Pol94, FC92, ZQ06], as well as configuration of the hand [Lie77, PSS⁺97]. A complete review of such measures has been done in [RS14]. While it may be desirable to use as many possible qualitz measures to compare the different grasp configurations, [LSBJB⁺12] showed the inherent similarities between the different measures, thus reducing the overall list from [RS14] to a select few. We employ some of these measures as objectives in our nonlinear optimisation setup, provided they are twice continuously differentiable. We select two of those that are not twice differentiable to be used as quality measures in this thesis and are introduced here.

3.2.1 Grasp isotropy index

The grasp matrix G_{ν} transforms the Lagrange multipliers λ_{C} to the net contact force $G_{\nu} \cdot \lambda_{C}$ on the object. Its six singular values $\sigma_{G_{\nu}}$ denote the grasp capability of withstanding external wrenches along the six translational and rotational directions. The quality index is computed as the ratio of the smallest to the largest singular value and called the grasp isotropy index. This means that the higher the value for this ratio, the better the object is isotropically controlled in all possible directions, see [LS88].

$$Q_1 = \frac{(\sigma_{G_{\nu}})_{min}}{(\sigma_{G_{\nu}})_{max}} \tag{3.29}$$

Extending the two-dimensional example in Section 3.1.6, in three dimensions for a grasp with two contact points modelled as hard contacts, the object is not fully constrained, as there is free rotation that is possible about the line joining the two contact points. This is reflected in the grasp matrix by the fact that the last singular value $(\sigma_{G_{\nu}})_{6}$ is zero. Therefore, for this grasp, the smallest singular value is taken as $(\sigma_{G_{\nu}})_{5}$ as $(\sigma_{G_{\nu}})_{min}$ in Equation (3.29), whereas for other grasps, it is $(\sigma_{G_{\nu}})_{6}$.

3.2.2 Uniformity of transformation index

The joint torques contribution to the contact forces λ_C applied to the object at the contact points is calculated through $-\boldsymbol{H}_{\nu}^T \cdot \lambda_C$. To provide an equitable contribution of joint torques to the contact forces, it is desirable to have a hand posture away from configurations in which certain joint torques produce no wrench on the object. For this, we compute the singular values $\sigma_{H_{\nu}}$ and obtain the ratio of the smallest to the largest singular value. This ratio is called the uniformity of transformation index, with a higher value signifying better object control ability.

$$Q_2 = \frac{\left(\sigma_{H_{\nu}}\right)_{min}}{\left(\sigma_{H_{\nu}}\right)_{max}} \tag{3.30}$$

Till now, we focussed on developing the mathematical basis for grasp stability and quality determination through contact point models. From here, we introduce the hand and the object rigid body models that will be used to perform the grasping simulations in the following chapters.

3.3 Hand Model

We consider a two-finger rigid multibody model for the hand, as shown in Fig. 3.9, modelled with time-dependent absolute coordinates $q(t) \in Q$, where Q is the configuration manifold. Using the description in Section 2.1, a single rigid body b is represented by twelve degrees of freedom $q^b \in \mathbb{R}^{12}$ comprising of a position vector φ^b of the centre of mass with respect to a global inertial frame and an orthonormal body-fixed coordinate frame, also called a director triad $d_1, d_2, d_3 \in \mathbb{R}^3$ which represents the orientation of the body, from Equation (2.1). The orthonormality condition is enforced through g^b_{int} (q^b) = $0 \in \mathbb{R}^6$, i.e. six internal constraints which results in six degrees of freedom for the body b, listed in Equation (2.2).

The hand is composed of nine bodies with the forearm, the wrist, the thumb (three bodies) and the index finger (four bodies), i.e. b = 1, ..., 9, due to which we obtain a configuration vector $\mathbf{q}(t) \in \mathbb{R}^l, l = 108$. The bodies are connected to form a tree-like structure through a combination of revolute [Ley11], cardan [ML13], nino (non-intersecting and non-orthogonal axes, see [PRB+17]), and fixed joints, as shown in Fig. 3.9. The forearm is connected

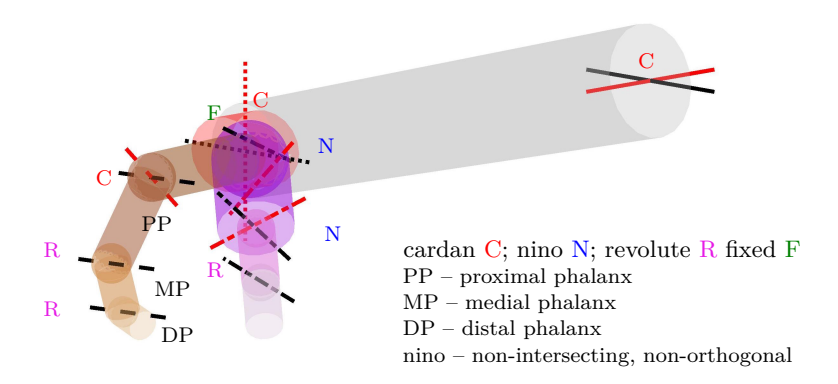


Figure 3.9: The two-finger hand model with the joint axes for different joints. The adjoining table shows the joint types.

to the ground with a cardan joint. The wrist is treated as a composite body for its eight individual bones and is connected to the forearm with a cardan joint. The four fingers, namely, index, middle, ring and little, are modelled similarly. The index finger, consisting of the metacarpal (MC), proximal, medial and distal phalanges, is fixed completely with respect to the wrist, followed by a succession of a cardan joint for the metacarpophalangeal (MCP) joint for flexion/extension (F/E) and adduction/abduction (A/A) motions, see [Kap81], and revolute joints for the proximal and distal interphalangeal (IP) joints for F/E motions. These joints are highly idealised, as implemented in [Maa14] for the upper extermity and in [KL16] for lower extremity, with the joint rotation axes perpendicular to the anatomical planes. The thumb is however modelled with joint axes skewed to the anatomical planes, as per the measurements suggested in [HBM⁺92], [HGB⁺95]. Furthermore, instead of the model described in [LMSB14, SBML⁺14] with sequential revolute joints, we implement a two degree of freedom joint with non-intersecting and non-orthogonal (nino) axes for the carpometacarpal (CMC) and the MCP joints for F/E and A/A motions, with relations from Equation (2.3). The thumb IP joint is a revolute joint for F/E motions. These joints are modelled through holonomic constraints q_{ext} $(q) = 0 \in \mathbb{R}^{41}$. Also, accounting for the

internal constraints for all bodies, we require g_{int} $(q) = 0 \in \mathbb{R}^{54}$, resulting in g_{int} $(q) = [g_{int} (q); g_{ext} (q)] = 0 \in \mathbb{R}^m$, m = 41 + 54 = 95. In summation, the redundant coordinates are constrained holonomically to the (l-m) = 13 dimensional constraint manifold which is locally parameterised by $u(t) \in \mathbb{R}^{13}$ minimal coordinates for the hand.

The measures of hand length and hand width are chosen for a 50th percentile male, [oD89]. They are used to calculate the specific dimensions of the finger digits modelled as cylinders, as shown in Figure 3.10, using the relations from [SB00]. The cylinder cross section is represented by the directors d_1^b, d_2^b , while

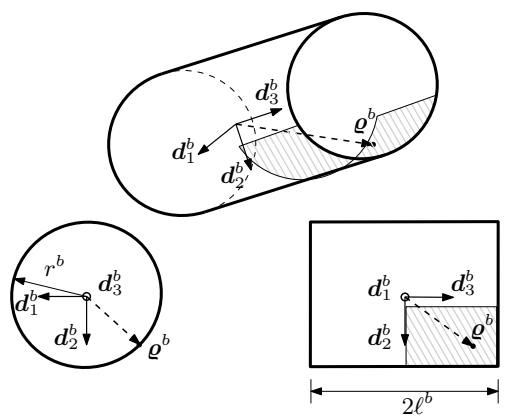


Figure 3.10: The surface S^b limiting the contact point $\boldsymbol{\varrho}^b$ on the finger digit b with radius r^b and length $2\ell^b$. The directors $\boldsymbol{d}_1^b, \boldsymbol{d}_2^b$ represent the cross-section, while \boldsymbol{d}_2^b represents the axis.

the cylinder axis is represented by d_3^b .

For a contact point ϱ^b to lie within an area S^b , as specified in Equation (3.9), the contact point coefficients $(\varrho_1^b, \varrho_2^b)$ are used in an equality constraint for the point to lie on the cylindrical cross-section via

$$g_{\varrho}^{a}(\varrho_{1}^{a},\varrho_{2}^{a}) = (\varrho_{1}^{b})^{2} + (\varrho_{2}^{b})^{2} - (r^{b})^{2} = 0,$$
 (3.31)

where r^b is the digit radius. Additionally, inequality constraints are used, firstly, for the third coordinate ϱ_3^b to lie within the finger length, and secondly,

for specific grasping areas, such as on the palmar side of the digit, as opposed to the dorsal side. Collectively, we can write them as,

$$\boldsymbol{h}_{\varrho}^{b}\left(\varrho_{1}^{b},\varrho_{2}^{b},\varrho_{3}^{b}\right) = \begin{bmatrix} \varrho_{1}^{b} - c_{1} \\ c_{2} - \varrho_{1}^{b} \\ \varrho_{2}^{b} - c_{3} \\ c_{4} - \varrho_{2}^{b} \\ \varrho_{3}^{b} - c_{5} \\ c_{6} - \varrho_{3}^{b} \end{bmatrix} \leq \boldsymbol{0}, \tag{3.32}$$

where the parameters c_1, c_2, \ldots, c_6 represent the areas S^b on the digit for particular grasps.

Finally, the hand is actuated through a minimal number of joint torques $\tau(t) \in \mathbb{R}^{13}$. They are multiplied by a transformation matrix $\boldsymbol{B}^T(q) \in \mathbb{R}^{108 \times 13}$ to give the redundant force $\boldsymbol{f}(q,\tau) = \boldsymbol{B}^T(q) \cdot \boldsymbol{\tau}$. The method to compose such a transformation matrix has been demonstrated in [Maa14, Lev11].

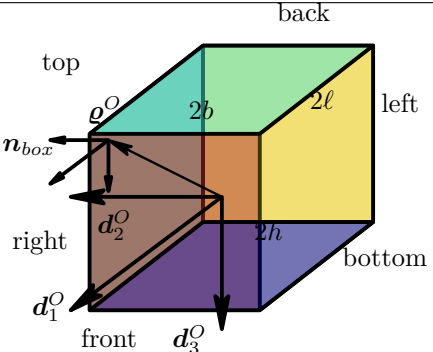
3.4 Object Models

The rigid object to be grasped is also modelled with redundant coordinates $q^O \in \mathbb{R}^{12}$, subject to internal constraints $g^O_{int} (q) = \mathbf{0} \in \mathbb{R}^6$. In this work, we grasp objects with primitive shapes, specifically, cube, cylinder or sphere, with specified dimensions. Similar to S^b , we can define the grasping areas S^O on the object for the three geometries. The object has uniform density with its mass centroid coinciding with the geometric one. For every object, we write expressions for the contact points to lie on their surface and the normal vector at those points.

3.4.1 Box

A box is described with three lengths 2ℓ , 2b and 2h and six planes, each perpendicular to one of the directors, as shown in Figure 3.11. For a contact point ρ^O on a plane, its location is described by the equation

$$g_{\varrho^O}^O\left(\varrho_1^O,\varrho_3^O,\varrho_2^O\right) = \boldsymbol{n}^T \cdot \left(\varrho^O - \boldsymbol{C}\right) = 0,$$
 (3.33)



front d_3^O Figure 3.11: The plane definitions on a box along with location of contact ϱ^O and the normal n_{box} at that location.

where n is the normal to the plane and C is a point on the plane. In particular for our model, we describe the six planes in Table 3.1. If the point must lie

Table 3.1: Plane definitions for box

plane	n	C		
front	\boldsymbol{d}_1^O	$\ell oldsymbol{d}_1^O$		
back	$-\boldsymbol{d}_{1}^{O}$	$-\ell oldsymbol{d}_1^O$		
right	\boldsymbol{d}_2^O	$boldsymbol{d}_2^O$		
left	$-\boldsymbol{d}_2^O$	$-b oldsymbol{d}_2^O$		
bottom	\boldsymbol{d}_3^O	$holdsymbol{d}_3^O$		
top	$-oldsymbol{d}_3^O$	$-h oldsymbol{d}_3^O$		

on the 'right' plane, the inequality constraints are

$$\boldsymbol{h}_{\boldsymbol{\varrho}^{O}}^{O}\left(\varrho_{1}^{O},\varrho_{2}^{O},\varrho_{3}^{O}\right) = \begin{bmatrix} \varrho_{2}^{O} - \ell \\ -\ell - \varrho_{2}^{O} \\ \varrho_{3}^{O} - h \\ -h - \varrho_{3}^{O} \end{bmatrix} \leq \boldsymbol{0}. \tag{3.34}$$

The inequality constraints for other planes change accordingly. Following on, we express the orthonormal basis at the contact point using the director along the normal to the plane, and other two directors forming its tangential plane. E.g. for the 'right' plane, the orthonormal basis is

$$\left[oldsymbol{n}_{box},oldsymbol{t}_{box},oldsymbol{o}_{box}
ight]\equiv\left[oldsymbol{d}_{1}^{O},oldsymbol{d}_{2}^{O},oldsymbol{d}_{3}^{O}
ight]$$

3.4.2 Cylinder

A cylinder is described with two dimensions, namely radius r and axis length 2ℓ . As with the finger digit in Section 3.3, the circular cross section of the cylinder is described with directors d_1^O, d_2^O , while d_3^O represents its axis, as shown in Figure 3.12. The contact point ϱ^O is constrained to lie on the curved

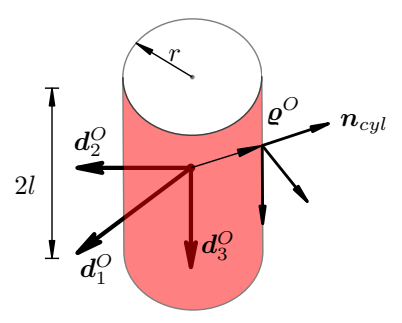


Figure 3.12: The depiction of contact surface on a cylinder with contact point location ϱ^O and the normal n_{cyl} at that location

surface through equality constraint,

$$g_{\varrho^O}^O\left(\varrho_1^O,\varrho_2^O,\varrho_3^O\right) = \left(\varrho_1^O\right)^2 + \left(\varrho_2^O\right)^2 - r^2 = 0 = 0, \tag{3.35}$$

along with inequality constraint to lie withing the length of the cylinder through inequality constraints,

$$\boldsymbol{h}_{\boldsymbol{\varrho}^{O}}^{O}\left(\varrho_{1}^{O},\varrho_{2}^{O},\varrho_{3}^{O}\right) = \begin{bmatrix} \varrho_{3}^{O} - \ell \\ -\ell - \varrho_{3}^{O} \end{bmatrix} \leq \boldsymbol{0}. \tag{3.36}$$

Additionally, we define an orthonormal basis $[n_{cyl}, t_{cyl}, o_{cyl}]$ at the contact point ϱ on the cylinder curved surface. The normal n is computed through

$$\boldsymbol{n}_{cyl} = \frac{\varrho_1^O d_1^O + \varrho_2^O d_2^O}{r}$$
 (3.37)

Thereon, one of the vectors in the tangential plane is the director along the cylinder axis, $t_{cyl} = d_3^O$, and the third vector is computed through the cross product

$$oldsymbol{o}_{cyl} = oldsymbol{n}_{cyl} imes oldsymbol{t}_{cyl}$$

3.5 Summary

The chapter discussed the steps normally followed in the mathematical representation of grasps beginning with the understanding of the concepts of twists and wrenches. These then included the evaluation of the expressions for the contact forces that are applied through the different contact models. The combined contact constraints vector was then utilized to develop expressions for the grasp matrix and the hand Jacobian so as to easily calculate two widely used grasp quality measures to compare grasping performance. Finally, the rigid and multibody models were introduced while elaborating on the location of contact points on their surfaces. The fundamentals laid in this chapter, particularly the contact constraints and the grasp quality measures, form the core elements in the development of the grasping optimal control problem in the next chapter and the evaluation of the results obtained therein.

4 Grasping optimal control setup

The application of optimal control methods to simulate mechanical systems has been well established in [OB08, LMO08, Sie12, Fla13]. The approach has been utilized to simulate electro-mechanical [Sch18, PSL17], feedback control [GL19] and more notably, biomechanical systems [ML13, KRL17, BNC $^+$ 17] showing its modularity, flexibility and robustness. While there are examples of performing trajectory optimization of biomechanical systems aided by motion capture and/or electromyography measurements [MTL10, NDH $^+$ 20, BBH11, ORB $^+$ 20], we focus on examples with predictive simulations [Koc16, SMF $^+$ 17, PRL22], especially with non-smooth dynamics, i.e. including contact and collisions.

The fundamental objective in using optimal control methods for biomechanical systems is to find controls, either joint torques or muscle activations, to perform movement of a musculoskeletal system is such a way as to minimise or maximise a certain physiological or task-related criterion. The optimal control formulation used in this thesis extends the work of [Koc16]. Herein, optimal control simulations of multibody dynamics was demonstrated for systems with non-smooth dynamics by using structure preserving integrators. The time integrator is a derived from a discrete variational principle based on a discrete action function that approximates the continuous one, as opposed to the use of standard integration methods, where one would start with ordinary differential equations and replace the continuous quantities with discrete approximations. The variational integrators show excellent long term energy behaviour [MW01] and enable the use of large time steps [MSL12]. The inclusion of non-smooth dynamics, in particular collisions and contacts, is done by way of holonomic constraint functions [Koc16]. In the case of grasping, we want to model the complete manuever where the hand first moves to the object and then holds the object and performs a manipulation task. In the first part, the hand and object systems have dynamics independent of each other, whereas while performing the manipulation task, the two systems are in contact. These are represented by two different sets of equations of

motion with known order of events. To execute this manuever, we make use of the discrete mechanics and optimal control for constrained systems (DMOCC) approach [LOBMO10], which generates a hybrid dynamical system with a given switching sequence and unknown switching times. The DMOCC approach transcribes the infinite dimensional optimal control problem is transcribed into a finite dimensional nonlinear optimisation problem, which is solved using standard sequential quadratic programming (SQP) or interior point(IP) algorithms.

The chapter begins with the continuous Lagrangian formulation in Section 4.1 where we derive the constrained forced Euler-Lagrange equations of motion from the variational principle. In Section 4.2, we consider the inclusion of the non-smooth dynamics and give the expressions for the equations of motion with collisions. Then, we dive into the deep end with the derivation of the discrete Euler-Lagrange (DEL) equations of motion for each of the hybrid phase in Section 4.3. This is followed by the description of the grasping optimal control problem (OCP) in Section 4.4. Thereafter, we discuss the discrete hybrid dynamical system with the DEL equations of motion, employed as equality constraints, the additional equality and inequality constraints and the objective functions that are employed in the OCP in Sections 4.4.1 to 4.4.3 respectively. Note that the grasping optimal control problem, the hybrid dynamical formulation and the objective functions have already been discussed and published in [PRL22].

4.1 Continuous Lagrangian formulation

We first describe the generic procedure to arrive at the continuous form Euler-Lagrange equations of motion under conservative forces. This procedure is described in detail in [Lev08, BL06] and repeated here in an abridged version.

We consider the Lagrangian for a mechanical system composed of the kinetic $\mathcal{T}(q, \dot{q})$ and potential $\mathcal{V}(q)$ energies as

$$\mathcal{L}(q, \dot{q}) = \mathcal{T}(q, \dot{q}) - \mathcal{V}(q)$$
(4.1)

where $q(t) \in \mathbb{R}^l$ contains the l-dimensional spatial configuration of the system and $\dot{q}(t)$ is its time derivative. The action integral for the system is obtained

by integrating the Lagrangian over a continuous time interval $[t_0, t_N]$

$$S(\mathbf{q}) = \int_{t_0}^{t_N} \mathcal{L}(\mathbf{q}, \dot{\mathbf{q}}) dt$$
 (4.2)

Hamilton's principle states that the action integral is stationary for any system trajectory, i.e. $\delta S=0$, i.e., the variation of the action is zero for all δq with boundary conditions. Using the variational principle, integration by parts and fixed boundary values $\delta q(t_0) = \delta q(t_N) = \mathbf{0}$, we obtain the second order Euler-Lagrange equations of motion

$$\frac{\partial \mathcal{L}(q, \dot{q})}{\partial q} - \frac{d}{dt} \left(\frac{\partial \mathcal{L}(q, \dot{q})}{\partial \dot{q}} \right) = \mathbf{0}$$
(4.3)

With the director-based multibody formulation, one works with a reduced system with a constraint vector $g(q) = 0 \in \mathbb{R}^m$ usually composed of internal and joint constraints. The set of constraints restricts the configuration q to a constraint manifold $C \subset Q$. To include them, the integrand of the action integral is extended with Lagrange multipliers $\lambda(t) \in \mathbb{R}^m$ as

$$S(\boldsymbol{q}, \boldsymbol{\lambda}) = \int_{t_0}^{t_N} \left(\mathcal{L}(\boldsymbol{q}, \dot{\boldsymbol{q}}) - \boldsymbol{g}(\boldsymbol{q})^T \cdot \boldsymbol{\lambda} \right) dt$$
(4.4)

where $\tilde{\mathcal{L}}(q,\dot{q},\boldsymbol{\lambda}) = \mathcal{L}(q,\dot{q}) - g(q)^T \cdot \boldsymbol{\lambda}$ is termed as the augmented Lagrangian. Using the Hamilton principle $\delta S = 0$, we arrive at the constrained Euler-Lagrange equations of motion

$$\frac{\partial \mathcal{L}(q, \dot{q})}{\partial q} - \frac{d}{dt} \left(\frac{\partial \mathcal{L}(q, \dot{q})}{\partial \dot{q}} \right) - G^{T}(q) \cdot \lambda = 0$$
 (4.5a)

$$g\left(q\right) = 0\tag{4.5b}$$

where $G = \frac{\partial g\left(q\right)}{\partial q} \in \mathbb{R}^{m \times l}$ is the constraint Jacobian. The expression $G^T\left(q\right) \cdot \lambda$ can be physically interpreted as the constraint forces. This system is composed of (l+m) equations. These are used to solve for the l redundant configuration variables and m Lagrange multipliers.

Following this, we consider the influence of non-conservative contributions such as friction or external loads on the mechanical system. These contributions change the amount of energy and are considered via the Lagrange-d'Alembert principle which reads

$$\delta \int_{t_0}^{t_N} \mathcal{L}(\mathbf{q}, \dot{\mathbf{q}}) dt + \int_{t_0}^{t_N} \delta W(\mathbf{q}, \boldsymbol{\tau}) dt = 0, \tag{4.6}$$

with the variation of the work of non-conservative contributions $\delta W\left(q,\tau\right)$, also known as non-conservative virtual work. In the context of this thesis, this refers to the actuation in terms of torques $\tau\left(t\right)\in\mathbb{R}^{l-m}$ applied to the joints in a multibody system. The virtual work

$$\delta W(\mathbf{q}, \boldsymbol{\tau}) = f(\mathbf{q}, \boldsymbol{\tau}) \cdot \delta \mathbf{q} \tag{4.7}$$

contains the non-conservative external forces $f(q, \tau)$. When evaluating the Lagrange-d'Alembert principle, the external forces appear in the equations of motion in Equation (4.5a) as

$$\frac{\partial \mathcal{L}\left(\boldsymbol{q}, \dot{\boldsymbol{q}}\right)}{\partial \boldsymbol{q}} - \frac{d}{dt} \left(\frac{\partial \mathcal{L}\left(\boldsymbol{q}, \dot{\boldsymbol{q}}\right)}{\partial \dot{\boldsymbol{q}}} \right) - \boldsymbol{G}^{T}\left(\boldsymbol{q}\right) \cdot \boldsymbol{\lambda} + \boldsymbol{f}\left(\boldsymbol{q}, \boldsymbol{\tau}\right) = \boldsymbol{0}$$
(4.8)

with Equation (4.5b) appearing as before.

The dimension of the system of equations is reduced with the use of two methods. For every $q \in C$ a (l-m)-dimensional tangent space T_qC exists, the basis vectors of which form a $l \times (l-m)$ matrix P(q) with the linear map $P(q): \mathbb{R}^{l-m} \to T_qC$. This is called as the null-space matrix as it has the property

range
$$(\mathbf{P}(\mathbf{q})) = \text{null}(\mathbf{G}(\mathbf{q})) = T_{\mathbf{q}}C.$$
 (4.9)

Due to this property, we see that the multiplication of the null-space matrix with the constraint Jacobian yields zero, i.e.,

$$G(q) \cdot P(q) = 0 \tag{4.10}$$

Pre-multiplying Equation (4.8) with the transpose of this matrix projects the equations of motion to the space T_qC , and eliminates the constraint Jacobian

 $G\left(q\right)$ along with the Lagrangian multipliers λ and we obtain the constrained forced Euler-Lagrange equations of motion

$$\boldsymbol{P}^{T}\left(\boldsymbol{q}\right) \cdot \left[\frac{\partial \mathcal{L}\left(\boldsymbol{q}, \dot{\boldsymbol{q}}\right)}{\partial \boldsymbol{q}} - \frac{d}{dt}\left(\frac{\partial \mathcal{L}\left(\boldsymbol{q}, \dot{\boldsymbol{q}}\right)}{\partial \dot{\boldsymbol{q}}}\right) + \boldsymbol{f}\left(\boldsymbol{q}, \boldsymbol{\tau}\right)\right] = \boldsymbol{0}$$
(4.11a)

$$g\left(q\right) = 0 \tag{4.11b}$$

This reduced system now consists of l equations which is used to solve for the l configuration variables. Thereafter, we employ a second method to further reduce the overall system size. In our description of multibody systems with holonomic constraints, there exists a possibility to locally parameterise the constraint manifold, $\mathbf{F}: U \subseteq \mathbb{R}^{l-m} \to C$ through $\mathbf{q} = \mathbf{F}(\mathbf{u})$ in terms of generalised coordinates $\mathbf{u}(t) \in \mathbb{R}^{l-m}$. These fulfil the holonomic constraints function

$$g\left(F\left(u\right)\right) = 0. \tag{4.12}$$

With respect to Equation (4.12), the constraints are automatically satisfied and accordingly the dimension of system of equations in Equation (4.11) reduced to (l-m)-dimensional equations of motion.

Remark 2 The null space matrix for a multibody system can be obtained through the approach of velocity analysis, which uses the relation between configuration velocities \dot{q} and the independent generalised velocities $\nu(t) \in \mathbb{R}^{l-m}$ as

$$\dot{q} = P(q) \cdot \nu$$

4.2 Collision and grasping dynamics

Following on from the continuous formulation described in the previous section, we consider the inclusion of collisions or contacts in dynamics of mechanical systems. In grasping problems, we extend the Euler-Lagrange equations of motion to handle unilateral contact problems, primarily impacts and sticking. The grasping motion occurs in two phases, namely the *reaching* and *manipulation* phases, as shown in Figure 4.1. The first phase begins with the hand moving towards the object, with a collision at the end to close the contact and form the grasp. In the second phase, the hand performs a manipulation maneuver with the contacts closed. To understand the equations

of motion for these dynamics, we first consider the collision at the end of the reaching phase, and thereafter extend the concept to closed contacts or adhesion during the manipulation phase.

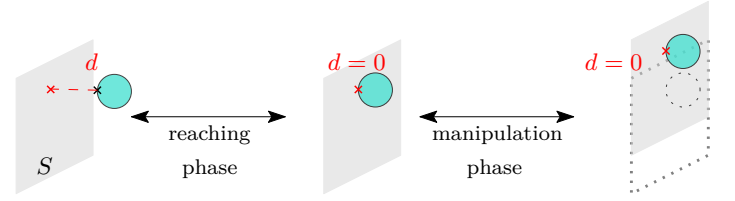


Figure 4.1: The reaching and manipulation phase description in the grasping problem. In the reaching phase, the finger digit, represented by a ball, moves toward the object surface S. After the gap d between them becomes zero, the two move together in the manipulation phase.

We consider the l-dimensional configuration \mathbf{q} from Section 4.1 defined on configuration manifold $Q \subseteq \mathbb{R}^l$ with velocity $\dot{\mathbf{q}} \in T_{\dot{\mathbf{q}}}Q$ in the time span $[t_0, t_N] \subset \mathbb{R}$. The configuration is limited to a admissible set $C = \{\mathbf{q} \in Q \mid \mathbf{g}(\mathbf{q}(t)) = \mathbf{0}\}$, due to holonomic constraints. At time $t_k \in (t_0, t_N)$, there occurs a collision in the form of a unilateral constraint $g_C(\mathbf{q}) = 0$. The admissible set, before and after collision, is further restricted to $C^+ = \{\mathbf{q} \in Q \mid \mathbf{g}(\mathbf{q}(t)) = \mathbf{0}, g_C \geq 0\}$ and the boundary δC^+ represents configurations $\mathbf{q}(t_k)$ where the non-penetration condition $g_C \geq 0$ becomes zero. With the collision constraint, the augmented Lagrangian is expressed as

$$\tilde{\mathcal{L}}(\boldsymbol{q}, \dot{\boldsymbol{q}}, \boldsymbol{\lambda}, \lambda_C) = \mathcal{L}(\boldsymbol{q}, \dot{\boldsymbol{q}}) - \boldsymbol{g}(\boldsymbol{q})^T \cdot \boldsymbol{\lambda} - g_C(\boldsymbol{q})^T \lambda_C. \tag{4.13}$$

Here, λ_{C} is the impact multiplier or the force associated with the collision constraint $g_{C}\left(\boldsymbol{q}\right)$.

For the purpose of brevity, the derivation of the equations of motion is avoided here as it is non-trivial and we move to the equations of motion directly. The reader is referred to [LHK12] and Chapter 4 in [Koc16] for the complete derivation. The equations of motion for such a collision problem for time $t < t_k$ are the same as expressed in Equation (4.11). However, at the

time of collision t_k the equations of motion take the form

$$\frac{\partial \mathcal{L}}{\partial \boldsymbol{q}} \left(\boldsymbol{q} \left(t_{k} \right), \dot{\boldsymbol{q}} \left(t_{k} \right) \right) - \frac{d}{dt} \left(\frac{\partial \mathcal{L}}{\partial \dot{\boldsymbol{q}}} \right) \left(\boldsymbol{q} \left(t_{k} \right), \dot{\boldsymbol{q}} \left(t_{k} \right) \right) - \boldsymbol{G}^{T} \left(\boldsymbol{q} \left(t_{k} \right) \right) \cdot \boldsymbol{\lambda} \\
- \boldsymbol{G}_{C}^{T} \left(\boldsymbol{q} \left(t_{k} \right) \right) \lambda_{C} = \boldsymbol{0} \quad (4.14a) \\
\boldsymbol{g} \left(\boldsymbol{q} \left(t_{k} \right) \right) = \boldsymbol{0} \quad (4.14b) \\
\boldsymbol{g}_{C} \left(\boldsymbol{q} \left(t_{k} \right) \right) = 0 \quad (4.14c)$$

Here $G_C^T(q(t_k)) = \frac{\partial g_C(q(t_k))}{\partial q}$ is the collision constraint Jacobian. This is a (l+m+1) system of equations, similar to Equation (4.5).

The contact constraint used to impose adhesion is similar to the collision constraint with the difference that the contact constraint is imposed for the time duration $t \in (t_k, t_N]$ and not just for the instant t_k . This leads us to a similar augmented Lagrangian as Equation (4.13), with a similar set of equations of motion as Equation (4.14) following the same derivation procedure.

As in Section 4.1, the size of the system of equations can be reduced using the null space matrix and reparameterisation for $t < t_k$ and $t > t_k$. For $t = t_k$, the null space matrix can be pre-multiplied to eliminate the constraint force $-\mathbf{G}^T(\mathbf{q}(t_k)) \cdot \boldsymbol{\lambda}$. However, the reparameterisation described in Equation (4.12) cannot be applied due to the additional constraint $g_C(\mathbf{q}(t_k)) = 0$ and therefore alternate strategies are needed to further reduce the number of equations, which will be dealt with in the following section.

4.3 Derivation of discrete Euler-Lagrange equations

The equations of motion in Sections 4.1 and 4.2 have been derived for configuration variable q which is used for describing the hand. For the discrete setting, we derive the equations of motion for the object as well. The object configuration is described using $q^O(t)$.

The derivation of the discrete equations of motion follow the similar script of starting the action integral and then utilising the calculus of variations and integration by parts, however, in a discrete context. We intend to derive a numerical time-stepping scheme intended to computationally determine the forward dynamics in the two phases of the grasping problem. In the

reaching phase, the equations of motion for the hand and the object are independent of each other. At the end of the reaching phase, there occurs a collision between the fingers and the object due to enforced constraints $g_{C1}\left(q,q^O,\varrho,\varrho^O\right)=\mathbf{0}\in\mathbb{R}^{n_c}$ for n_c contact points. These constraints are also termed as gap functions, as they enforce gap closure and are expressed using the PwoF contact model constraint from Section 3.1.1. To perform the required manipulation, the hand and the object are constrained to move together using contact constraints $g_{C2}\left(q,q^O\right)=\mathbf{0}\in\mathbb{R}^{p\cdot n_c}$, where p depends on the number of constraints used at every contact point. For instance, in case of hard contact model from Section 3.1.2 we have p=3, while for the soft contact model from Section 3.1.3 we have p=4.

Remark 3 The gap closure constraint $g_{C1}(q, q^O, \varrho, \varrho^O) = 0$ is denoted in this derivation as $g_{C1}(q, q^O) = 0$, since the contact points ϱ_I, ϱ_I^O are not time-continuous and can be excluded from the derivation, for brevity.

The discrete Euler-Lagrange (DEL) equations of motion to describe the hand and object dynamics are derived through a discrete variational principle, as described in [LMO08]. This gives a symplectic time stepping scheme with structure preserving properties. Since the derivation procedure for the hand and the object systems is similar, except for the configuration vector and the control torques, we only focus on the procedure for the hand and reproduce the final equations for the object later on.

In the first part we introduce the discrete approximations for the continuous forms of the Lagrangian and the constraints. It is followed by introducing the discrete action and thereafter apply Hamilton's stationarity principle to obtain the DEL equations of motion.

In a numerical setting, the time interval $t = [t_0, t_N] \subset \mathbb{R}$ is discretized by $t_1 = \Delta t, \dots, t_n = n\Delta t, \dots, t_N = N\Delta t$ with $N \in \mathbb{N}$ time nodes and $\Delta t \in \mathbb{R}$ as the time step. The discrete configuration variables $q_d = \{q_n\}_{n=0}^N$ are then approximations at these time nodes such as $q_n \approx q(t_n)$, and other discrete quantities such as $\tau_d = \{\tau_n\}_{n=0}^{N-1}$, $q_d^O = \{q_n^O\}_{n=0}^N$ accordingly are approximated as $\tau_n \approx \tau(t_n)$, $q_n^O \approx q^O(t_n)$ respectively, and so on. We begin

with the discrete Lagrangian, $\mathcal{L}_d: Q \times Q \to \mathbb{R}$,

$$\mathcal{L}_{d}\left(\boldsymbol{q}_{n}, \boldsymbol{q}_{n+1}\right) \approx \int_{t_{n}}^{t_{n+1}} \mathcal{L}\left(\boldsymbol{q}, \dot{\boldsymbol{q}}\right) dt$$

$$\mathcal{L}_{d}\left(\boldsymbol{q}_{n}, \boldsymbol{q}_{n+1}\right) = \Delta t \mathcal{L}\left(\frac{\boldsymbol{q}_{n+1} + \boldsymbol{q}_{n}}{2}, \frac{\boldsymbol{q}_{n+1} - \boldsymbol{q}_{n}}{\Delta t}\right)$$

$$(4.15)$$

which is an approximation of the action of the continuous Lagrangian \mathcal{L} in a time internal $[t_n, t_{n+1}]$ through a midpoint rule for the configuration and finite difference approximation for the velocity. The discrete constraint function in the similar time interval is approximated version of the constraint function g(q) and multipliers λ , with the trapezoidal rule

$$\frac{1}{2} \mathbf{g}_d \left(\mathbf{q}_n \right)^T \cdot \boldsymbol{\lambda}_n + \frac{1}{2} \mathbf{g}_d \left(\mathbf{q}_{n+1} \right)^T \cdot \boldsymbol{\lambda}_{n+1} \approx \int_{t_n}^{t_{n+1}} \mathbf{g} \left(\mathbf{q} \right)^T \cdot \boldsymbol{\lambda} dt \tag{4.16}$$

wherein $g_d(q_n) = \Delta t g(q_n)$ and consequently $G_d(q_n) = \Delta t G(q_n)$ is the discrete Jacobian and $\lambda_n \approx \lambda(t_n)$ is approximation for the discrete multipliers $\lambda_d = \{\lambda_n\}_{n=1}^N$.

Similar to Equation (4.4), the discrete approximation of the augmented Lagrangian becomes

$$\tilde{\mathcal{L}}_{d}\left(\boldsymbol{q}_{n}, \boldsymbol{\lambda}_{n}, \boldsymbol{q}_{n+1}, \boldsymbol{\lambda}_{n+1}\right) = \mathcal{L}_{d}\left(\boldsymbol{q}_{n}, \boldsymbol{q}_{n+1}\right) - \frac{1}{2}\left(\boldsymbol{g}_{d}^{T}\left(\boldsymbol{q}_{n}\right) \cdot \boldsymbol{\lambda}_{n} + \boldsymbol{g}_{d}^{T}\left(\boldsymbol{q}_{n+1}\right) \cdot \boldsymbol{\lambda}_{n+1}\right)$$

$$(4.17)$$

Equation (4.17) represents the dynamics of the hand over the complete time-span $t = [t_0, t_N]$. Next, the collision constraints occurring at time t_k are expressed in their discrete forms using the trapezoidal rule similar to Equation (4.16). They are discretized between the time interval $[t_{k-1}, t_{k+1}]$, see [LHK12, Koc16], as

$$\frac{t_{k} - t_{k-1}}{2} \boldsymbol{g}_{C1}^{T} \left(\boldsymbol{q}_{k}, \boldsymbol{q}_{k}^{O}\right) \cdot \boldsymbol{\lambda}_{C1,k} + \frac{t_{k+1} - t_{k}}{2} \boldsymbol{g}_{C1}^{T} \left(\boldsymbol{q}_{k}, \boldsymbol{q}_{k}^{O}\right) \cdot \boldsymbol{\lambda}_{C1,k} \approx
\int_{t_{k-1}}^{t_{k+1}} \boldsymbol{g}_{C1}^{T} \left(\boldsymbol{q}\left(t_{k}\right), \boldsymbol{q}^{O}\left(t_{k}\right)\right) \cdot \boldsymbol{\lambda}_{C1}\left(t_{k}\right) dt,$$
(4.18)

while the contact constraints are expressed as a continuous sum in the discrete form for the time interval (t_{k+1}, t_N]

$$\sum_{n=k+1}^{N-1} \frac{\Delta t}{2} \boldsymbol{g}_{C2}^{T} \left(\boldsymbol{q}_{n}, \boldsymbol{q}_{n}^{O} \right) \cdot \boldsymbol{\lambda}_{C2,n} + \frac{\Delta t}{2} \boldsymbol{g}_{C2}^{T} \left(\boldsymbol{q}_{n+1}, \boldsymbol{q}_{n+1}^{O} \right) \cdot \boldsymbol{\lambda}_{C2,n+1} \approx$$

$$\int_{t_{k+1}}^{t_{N}} \boldsymbol{g}_{C2}^{T} \left(\boldsymbol{q} \left(t \right), \boldsymbol{q}^{O} \left(t \right) \right) \cdot \boldsymbol{\lambda}_{C2} \left(t \right) dt$$

$$(4.19)$$

Here, the contact closure time t_k is between $t_{k-1} \leq t_k \leq t_{k+1}$ with $t_{k+1} - t_{k-1} = \Delta t$. Thereafter, we include the discrete versions of the collision and contact constraints in the augmented Lagrangian from Equation (4.17) and write the discrete action sum \tilde{S}_d over the complete time interval $[t_0, t_N]$ analogous to the continuous one in Section 4.2, which reads as

$$\tilde{S}_d = \tilde{S}_{d,1} + \tilde{S}_{d,2} + \tilde{S}_{d,3} \tag{4.20}$$

with components $\tilde{S}_{d,1}$, $\tilde{S}_{d,2}$ and $\tilde{S}_{d,3}$ representing the discrete action for the reaching phase, collision instant and manipulation phase, respectively. The individual components are

$$\tilde{S}_{d,1} = \sum_{n=0}^{k-2} \tilde{\mathcal{L}}_d \left(\boldsymbol{q}_n, \boldsymbol{\lambda}_n, \boldsymbol{q}_{n+1}, \boldsymbol{\lambda}_{n+1} \right), \tag{4.21}$$

$$\tilde{S}_{d,2} = \tilde{\mathcal{L}}_d \left(\mathbf{q}_{k-1}, \boldsymbol{\lambda}_{k-1}, \mathbf{q}_k, \boldsymbol{\lambda}_k \right) - \frac{t_k - t_{k-1}}{2} \mathbf{g}_{C1}^T \left(\mathbf{q}_k, \mathbf{q}_k^O \right) \cdot \boldsymbol{\lambda}_{C1,k}
+ \tilde{\mathcal{L}}_d \left(\mathbf{q}_k, \boldsymbol{\lambda}_k, \mathbf{q}_{k+1}, \boldsymbol{\lambda}_{k+1} \right) - \frac{t_{k+1} - t_k}{2} \mathbf{g}_{C1}^T \left(\mathbf{q}_k, \mathbf{q}_k^O \right) \cdot \boldsymbol{\lambda}_{C1,k}$$
(4.22)

and

$$\tilde{S}_{d,3} = \sum_{n=k+1}^{N-1} \tilde{\mathcal{L}}_{d} (q_{n}, \lambda_{n}, q_{n+1}, \lambda_{n+1})
- \sum_{n=k+1}^{N-1} \left(\frac{\Delta t}{2} g_{C2}^{T} (q_{n}, q_{n}^{O}) \cdot \lambda_{C2,n} + \frac{\Delta t}{2} g_{C2}^{T} (q_{n+1}, q_{n+1}^{O}) \cdot \lambda_{C2,n+1} \right)$$
(4.23)

The discrete variational principle for the constrained motion requires that $\delta \tilde{S}_d = 0$ for all possible variations $\{\delta q_n\}_{n=0}^N$, $\{\delta q_n^O\}_{n=k}^N$, $\{\delta \lambda_n\}_{n=0}^N$, $\delta \lambda_{C1,k}$, $\{\delta \lambda_{C2,n}\}_{n=k+1}^N$ with zero variations for the configurations and Lagrange multipliers at the time boundaries, i.e. $\delta q_0 = \delta q_N = \mathbf{0}$, $\delta q_N^O = \mathbf{0}$, $\delta \lambda_0 = \delta \lambda_N = \mathbf{0}$, and $\delta \lambda_{C2,N} = \mathbf{0}$. Using the calculus of variations, we now write the variation for each of the actions expressed in Equations (4.21) to (4.23) as follows, starting with $\delta \tilde{S}_{d,1}$

$$\delta \tilde{S}_{d,1} = \left[D_1 \mathcal{L}_d \left(\mathbf{q}_0, \mathbf{q}_1 \right) - \frac{t_1 - t_0}{2} \mathbf{G} \left(\mathbf{q}_0 \right)^T \cdot \boldsymbol{\lambda}_0 \right] \cdot \delta \mathbf{q}_0$$

$$- \frac{t_1 - t_0}{2} \mathbf{g}^T \left(\mathbf{q}_0 \right) \cdot \delta \boldsymbol{\lambda}_0$$

$$+ \sum_{n=1}^{k-1} \left[D_2 \mathcal{L}_d \left(\mathbf{q}_{n-1}, \mathbf{q}_n \right) + D_1 \mathcal{L}_d \left(\mathbf{q}_n, \mathbf{q}_{n+1} \right) \right]$$

$$- \frac{t_{n+1} - t_{n-1}}{2} \mathbf{G}^T \left(\mathbf{q}_n \right) \cdot \boldsymbol{\lambda}_n \cdot \delta \mathbf{q}_n$$

$$- \sum_{n=1}^{k-1} \frac{t_{n+1} - t_{n-1}}{2} \mathbf{g}^T \left(\mathbf{q}_n \right) \cdot \delta \boldsymbol{\lambda}_n,$$

$$(4.24)$$

followed by $\delta \tilde{S}_{d,2}$ with

$$\delta \tilde{S}_{d,2} = \left[D_2 \mathcal{L}_d \left(\mathbf{q}_{k-1}, \mathbf{q}_k \right) + D_1 \mathcal{L}_d \left(\mathbf{q}_k, \mathbf{q}_{k+1} \right) \right.$$

$$\left. - \frac{t_{k+1} - t_{k-1}}{2} \mathbf{G}^T \left(\mathbf{q}_k \right) \cdot \boldsymbol{\lambda}_k \right.$$

$$\left. - \frac{t_{k+1} - t_{k-1}}{2} \mathbf{G}_{C1}^T \left(\mathbf{q}_k \right) \cdot \boldsymbol{\lambda}_{C1,k} \right] \cdot \delta \mathbf{q}_k$$

$$\left. - \frac{t_{k+1} - t_{k-1}}{2} \mathbf{g}^T \left(\mathbf{q}_k \right) \cdot \delta \boldsymbol{\lambda}_k \right.$$

$$\left. - \frac{t_{k+1} - t_{k-1}}{2} \mathbf{g}_{C1}^T \cdot \delta \boldsymbol{\lambda}_{C1,k},$$

$$(4.25)$$

and finally with $\delta \tilde{S}_{d,3}$

$$\delta \tilde{S}_{d,3} = \sum_{n=k+1}^{N-1} \left[D_{2} \mathcal{L}_{d} \left(\mathbf{q}_{n-1}, \mathbf{q}_{n} \right) + D_{1} \mathcal{L}_{d} \left(\mathbf{q}_{n}, \mathbf{q}_{n+1} \right) - \frac{t_{n+1} - t_{n-1}}{2} \mathbf{G}^{T} \left(\mathbf{q}_{n} \right) \cdot \boldsymbol{\lambda}_{n} \right] \cdot \delta \mathbf{q}_{n}$$

$$- \sum_{n=k+1}^{N-1} - \left[\frac{t_{n+1} - t_{n-1}}{2} \mathbf{G}^{T}_{C2} \left(\mathbf{q}_{n} \right) \cdot \boldsymbol{\lambda}_{C2,n} \right] \cdot \delta \mathbf{q}_{n}$$

$$- \sum_{n=k+1}^{N-1} \frac{t_{n+1} - t_{n-1}}{2} \mathbf{g}^{T} \left(\mathbf{q}_{n} \right) \cdot \delta \boldsymbol{\lambda}_{n} - \frac{t_{n+1} - t_{n-1}}{2} \mathbf{g}^{T}_{C2} \cdot \delta \boldsymbol{\lambda}_{C2,n}$$

$$+ \left[D_{2} \mathcal{L}_{d} \left(\mathbf{q}_{N-1}, \mathbf{q}_{N} \right) - \frac{t_{N} - t_{N-1}}{2} \mathbf{G}^{T} \left(\mathbf{q}_{N} \right) \cdot \boldsymbol{\lambda}_{N} \right]$$

$$- \frac{t_{N} - t_{N-1}}{2} \mathbf{G}^{T}_{C2} \left(\mathbf{q}_{N} \right) \cdot \boldsymbol{\lambda}_{C2,N} \cdot \delta \boldsymbol{\lambda}_{N} - \frac{t_{N} - t_{N-1}}{2} \mathbf{g}^{T}_{C2} \left(\mathbf{q}_{N} \right) \cdot \delta \boldsymbol{\lambda}_{C2,N}. \quad (4.26)$$

with $\delta \tilde{S}_d = \delta \tilde{S}_{d,1} + \delta \tilde{S}_{d,2} + \delta \tilde{S}_{d,3}$. Here D_1 and D_2 refer to the differential operator with respect to the first and second argument of \mathcal{L}_d , respectively. The fundamental lemma of the calculus of variations requires that the terms in the brackets in Equations (4.24) to (4.26) to equal zero. Applying the lemma to variation $\delta \tilde{S}_{d,1}$ from Equation (4.24), we obtain the DEL equations of motion to describe the forward dynamics for the hand for the time nodes before the collision $n = 1, \ldots, k-1$. They are utilized to compute the configuration q_{n+1} from configurations q_{n-1} , q_n via

$$D_{2}\mathcal{L}_{d}(\mathbf{q}_{n-1}, \mathbf{q}_{n}) + D_{1}\mathcal{L}_{d}(\mathbf{q}_{n}, \mathbf{q}_{n+1}) - \frac{t_{n+1} - t_{n-1}}{2} \mathbf{G}^{T}(\mathbf{q}_{n}) \cdot \boldsymbol{\lambda}_{n} = \mathbf{0}$$

$$\frac{t_{n+1} - t_{n-1}}{2} \mathbf{g}^{T}(\mathbf{q}_{n+1}) = \mathbf{0}.$$
(4.27)

Similarly, considering $\delta \tilde{S}_{d,2}$ for the collision time instant t_k , we get the

equations,

$$D_{2}\mathcal{L}_{d}(\boldsymbol{q}_{k-1}, \boldsymbol{q}_{k}) + D_{1}\mathcal{L}_{d}(\boldsymbol{q}_{k}, \boldsymbol{q}_{k+1}) - \frac{t_{k+1} - t_{k-1}}{2}\boldsymbol{G}^{T}(\boldsymbol{q}_{k}) \cdot \boldsymbol{\lambda}_{k}$$

$$-\frac{t_{k+1} - t_{k-1}}{2}\boldsymbol{G}_{C1}^{T}(\boldsymbol{q}_{k}) \cdot \boldsymbol{\lambda}_{C1,k} = \boldsymbol{0}$$

$$\frac{t_{k+1} - t_{k-1}}{2}\boldsymbol{g}^{T}(\boldsymbol{q}_{k}) = \boldsymbol{0},$$

$$\frac{t_{k+1} - t_{k-1}}{2}\boldsymbol{g}_{C1}^{T}(\boldsymbol{q}_{k}) = \boldsymbol{0}.$$

$$(4.28)$$

Finally, with $\delta \tilde{S}_{d,3}$, we can write the equations of motion for the manipulation phase, which occurs from $n=k+1,\ldots,N-1$

$$D_{2}\mathcal{L}_{d}\left(q_{n-1}, q_{n}\right) + D_{1}\mathcal{L}_{d}\left(q_{n}, q_{n+1}\right) - \frac{t_{n+1} - t_{n-1}}{2}\boldsymbol{G}^{T}\left(q_{n}\right) \cdot \boldsymbol{\lambda}_{n}$$

$$-\frac{t_{n+1} - t_{n-1}}{2}\boldsymbol{G}_{C2}^{T}\left(q_{n}\right) \cdot \boldsymbol{\lambda}_{C2,n} = \mathbf{0}$$

$$\frac{t_{n+1} - t_{n-1}}{2}\boldsymbol{g}^{T}\left(q_{n}\right) = \mathbf{0},$$

$$\frac{t_{n+1} - t_{n-1}}{2}\boldsymbol{g}_{C2}^{T}\left(q_{n}\right) = \mathbf{0}.$$
(4.29)

As in the continuous case, the size of the system of equations in Equations (4.27) to (4.29) is modified in the following ways. Firstly, the discrete external force due to the control torques is added. The virtual work described in Equation (4.7) is approximated by

$$f_n^-(q_n, \tau_n^-) \cdot \delta q_n + f_n^+(q_{n+1}, \tau_n^+) \cdot \delta q_{n+1} \approx \int_{t_n}^{t_{n+1}} f \cdot \delta q dt,$$
 (4.30)

where f_n^-, f_n^+ are named as the left and right discrete forces, respectively and $\tau_n^- = \tau_n^+ = \frac{\Delta t}{2} \tau_n$, refer to Figure 1 in [LOBMO10]. Furthermore, the discrete null space $P(q_n) \in \mathbb{R}^{l \times (l-m)}$ is pre-multiplied to eliminate the constraint forces, as done in the continuous method in Equation (4.11). Finally, the minimal coordinates are also discretized as incremental updates $u_d = \{u_n\}_{n=1}^N$, which is used to form a discrete local or nodal reparameterisation $q_{n+1} = F_d(u_{n+1}, q_n)$, such the holonomic constraints $g(q_{n+1}) = 0$ are fulfilled.

With these modifications, the equations of motion from Equation (4.27) appear as

$$\boldsymbol{P}^{T}\left(\boldsymbol{q}_{n}\right)\cdot\left[D_{2}\mathcal{L}_{d}\left(\boldsymbol{q}_{n-1},\boldsymbol{q}_{n}\right)+D_{1}\mathcal{L}_{d}\left(\boldsymbol{q}_{n},\boldsymbol{F}_{d}\left(\boldsymbol{u}_{n+1},\boldsymbol{q}_{n}\right)\right)+\boldsymbol{f}_{n-1}^{+}+\boldsymbol{f}_{n}^{-}\right]=\boldsymbol{0}$$
(4.31)

to compute the update u_{n+1} . The forces are evaluated as $f_{n-1}^+ = B^T(q_n) \cdot \tau_n$ and $f_n^- = B^T(q_n) \cdot \tau_{n+1}$, where B(q) is the transformation matrix, see [Ley11, Maa14].

For the object, we follow the same principle with \mathcal{L}_d^O as the discrete Lagrangian and then following the same procedure to obtain the DEL equations of motion. These are similarly pre-multiplied by the transposed object discrete null-space matrix $\boldsymbol{P}^{O,T}\left(\boldsymbol{q}_n^O\right)$. Here a nodal reparameterisation is not carried out and the internal constraints are solved for every time node as well. We solve the forward dynamics equations

$$P^{O,T}\left(q_{n}^{O}\right)\cdot\left[D_{2}\mathcal{L}_{d}^{O}\left(q_{n-1}^{O},q_{n}^{O}\right)+D_{1}\mathcal{L}_{d}^{O}\left(q_{n}^{O},q_{n+1}^{O}\right)\right]=\mathbf{0}$$

$$q^{int}\left(q_{n+1}^{O}\right)=\mathbf{0}$$
(4.32)

to solve for the configuration q_{n+1}^O , given previous time step configurations q_{n-1}^O and q_n^O .

At the instant of contact closure and the time nodes thereafter, i.e., $n=k,\ldots,N$, the open chain dynamics of the hand transforms into a closed loop system due to inclusion of the holonomic contact constraints. To describe closed loop dynamics with redundant or natural coordinates, two methods have been presented in literature, both involving the contact constraint Jacobian. Firstly, the Jacobian can be eliminated through the use of another null-space matrix, as done for the kinematic chain constraint Jacobian in Equation (4.11). This method reduces the size of the problem, again, by eliminating the Lagrange multipliers required for the contact constraints. This matrix can be either analytically described for a closed kinematic chain, e.g. see [BL06], or can be evaluated using the QR decomposition, as described in [Maa14, Koc16]. The former method is contact configuration dependent and not modular, while the latter involves a numerical method which is computationally expensive and for which a derivative cannot be efficiently written. In both methods, the Lagrange multipliers for the contact constraints

have to be recalculated to be used in the frictional constraints, which is an additional computational cost.

The second method is to not eliminate the contact constraint Jacobian in the equations of motion as in [dJB94]. This increases the problem size. However, it avoids all the extra computations and keeps the structure modular. The omission of nodal reparameterisation for the object further preserves the modularity to keep the form of the system of equations independent of the number of the contact points, and the digits which perform the contact closure. Keeping this in mind, we write the closed loop dynamics discrete equations of motion for the hand and object as

$$P^{T}(q_{n}) \cdot \left[D_{2}\mathcal{L}_{d}(q_{n-1}, q_{n}) + D_{1}\mathcal{L}_{d}(q_{n}, F_{d}(u_{n+1}, q_{n})) + f_{n-1}^{+} + f_{n}^{-} - G_{C}^{T}(q_{n}, q_{n}^{O}) \cdot \lambda_{C, n}\right] = \mathbf{0}$$

$$P^{O,T}(q_{n}^{O}) \cdot \left[D_{2}\mathcal{L}_{d}^{O}(q_{n-1}^{O}, q_{n}^{O}) + D_{1}\mathcal{L}_{d}^{O}(q_{n}^{O}, q_{n+1}^{O}) - G_{C}^{O,T}(q_{n}, q_{n}^{O}) \cdot \lambda_{C, n}\right] = \mathbf{0}$$

$$g^{int}(q_{n+1}^{O}) = \mathbf{0}$$

$$g_{C}(q_{n+1}, q_{n+1}^{O}) = \mathbf{0}.$$

$$(4.33)$$

The DEL equations of motion can be written either by using the bracket terms in Equation (4.28) or Equation (4.29) along with the corresponding equations for the object dynamics. Equation (4.33) is generic for both gap closure or contact constraints between two systems. This means that $g_C(q_{n+1}, q_{n+1}^O)$ can be chosen to be either $g_{C1}(q_{n+1}, q_{n+1}^O)$ or $g_{C2}(q_{n+1}, q_{n+1}^O)$, with the corresponding constraint Jacobian, and the equations look the same. Both systems are pre-multiplied with their respective null-space matrices and the hand actuation through the redundant force is also considered.

Equation (4.33) solves for hand and object configurations, namely u_{n+1} and q_{n+1}^O respectively, using their respective configurations at the previous two time nodes, as well as the Lagrange multipliers to calculate the contact force $\lambda_{C,n}$. Using Equations (4.31) to (4.33), we now move to the description of the optimal control problem for the reaching and manipulation phases in the following sections.

4.4 Grasping optimal control problem

The time-continuous optimal control problem (OCP) for mechanical systems has been exhaustively discussed in a number of publications and theses, such as [LHK12, OB08, Fla13, Maa14, Koc16, Sch18] to name a few. We describe it here in brief for the sake of completeness. Consider a dynamical system described through $\dot{x}(t) = f(x(t), u(t))$ with state x, control u and continuously differentiable f. For the system to be steered from an initial state x_0 to a final one a time interval $t \in [0,T]$, with path constraints $h(x(t), u(t)) \geq 0$, an optimal control problem can be formulated as

$$\min_{x(\cdot), u(\cdot), T} J(x, u) = \int_{0}^{T} C(x(t), u(t)) dt$$
subject to $\dot{x}(t) = f(x(t), u(t))$

$$x(0) = x_{0}$$

$$0 \le h(x(t), u(t))$$
(4.34)

where J is a given objective functional with continuously differentiable function C. The time interval T may be either fixed or appear as a degree of freedom in the optimisation problem.

The numerical simulation of OCP is performed here with the direct approach [OB08, LHK12], which transcribes the infinite dimensional optimal control problem into a finite dimensional nonlinear programming problem, see [Bet98, Str98]. The OCP has defined numbers of time nodes, namely N_k and N_m for the reaching and grasping phases, respectively, with $N = N_k + N_m$. The discrete unknowns used in the OCP are the trajectories u_d, q_d^O for the hand and object, respectively, along with control actuation torques τ_d for the hand, as introduced in Section 4.3.

Furthermore the Lagrangian multipliers to describe the contact forces $\lambda_{C,d} = \{\lambda_{C,n}\}_{n=N_k}^N$ and the contact points vector $\boldsymbol{\varrho} \in \mathbb{R}^{3 \cdot n_c}$ on the finger digits are included as optimisation variables. The vector $\boldsymbol{\varrho}$ consists of the n_c contact point locations $\{\varrho_I\}_{I=1,2,3}$. The contact points on the object are not a part of the optimisation variables, as they are calculated according to the reformulation in Equation (3.18). For a contact point $\boldsymbol{\varrho}^a$ on the hand, the counterpart on the object (with coefficients $\{\varrho_I^{O,a}\}_{I=1,2,3}$) at the instant of

contact closure is calculated through

$$\{arrho_{I}^{O,a}\}_{I=1,2,3} = \left[oldsymbol{d}_{1}^{O}, \ oldsymbol{d}_{2}^{O}, \ oldsymbol{d}_{3}^{O}
ight]^{T} \cdot \left(oldsymbol{arphi}^{a} + oldsymbol{arrho}^{a} - oldsymbol{arphi}^{O}
ight),$$

with the quantities on the right hand side as optimisation variables. Finally, the optimal durations T_k , T_m for the reaching and grasping phases are part of the optimisation variables. We define a discrete objective function

$$J_d\left(\boldsymbol{u}_d, \boldsymbol{\tau}_d, \boldsymbol{q}_d^O, \boldsymbol{\lambda}_{C,d}, \boldsymbol{\varrho}, T_k, T_m\right) = \sum_{n=0}^{N-1} B_d\left(\boldsymbol{u}_n, \boldsymbol{u}_{n+1}, \boldsymbol{\tau}_n, \boldsymbol{q}_n^O, \boldsymbol{q}_{n+1}^O, \boldsymbol{\lambda}_{C,n}, \boldsymbol{\varrho}, T_k, T_m\right)$$
(4.35)

as a sum of a scalar-valued cost function B_d , which has to be minimised subject to equality and inequality constraints. As it is the case in nonlinear constrained optimisation, the objective and constraints equations have to be twice continuously differentiable to ensure feasibility in obtaining a solution. The following subsections describe the constraints used in the grasping OCP, in particular the DEL equations of motion describing the grasping dynamics.

4.4.1 Hybrid dynamical system

The hybrid formulation, with the varying equality and inequality constraints imposed at the different time nodes, is illustrated in Fig. 4.2. These are described along with the DEL equations of motion listed below, which are included in the OCP as equality constraints.

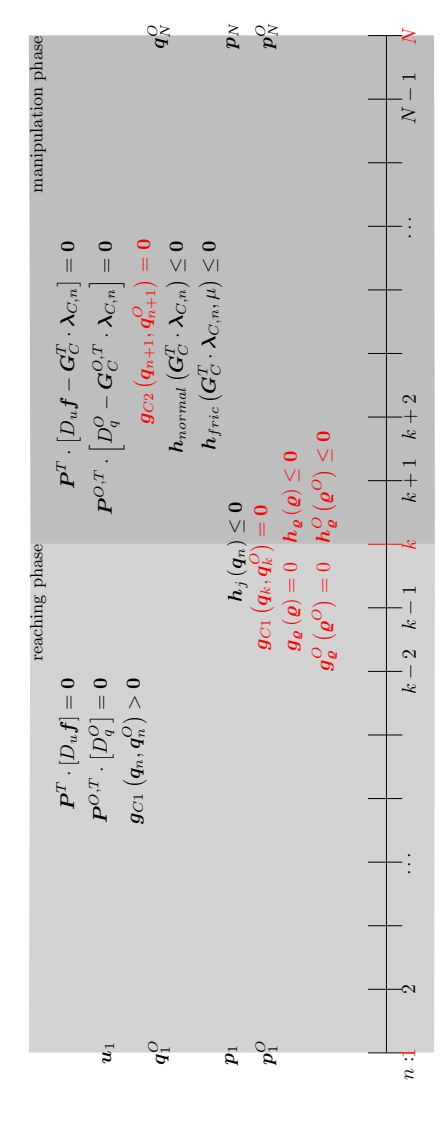


Figure 4.2: The grasping OCP setup with the time grid of the reaching and the grasping phase and $D_q^O = D_1 \mathcal{L}_d^O \left(q_{n-1}^O, q_n^O\right) + D_2 \mathcal{L}_d^O \left(q_n^O, q_{n+1}^O\right)$ are the DEL equations of motion. The additional and the contact-related equality and inequality constraints in the two phases describe the hybrid dynamical system. The placeholders $D_{u}f = D_{1}\mathcal{L}_{d}(q_{n-1},q_{n}) + D_{2}\mathcal{L}_{d}(q_{n},F_{d}(u_{n+1},q_{n})) + f_{n-1}^{+} + f_{n}^{-}$ constraints are catalogued in Section 4.4.2.

At node n=0 or time t=0, the positions for the hand q_0 , through u_0 , and the object q_0^O are constrained with respect to prescribed configurations q_{00} and q_{00}^O , respectively. Additionally, we apply the discrete Legendre transform, see [LOBMO10], to constrain their initial momenta with prescribed values p_0 and p_0^O for the hand and the object, respectively,

$$egin{aligned} oldsymbol{P}^{T}\left(oldsymbol{q}_{0}
ight) \cdot \left[oldsymbol{p}_{0} + D_{1}\mathcal{L}_{d}\left(oldsymbol{q}_{0}, oldsymbol{F}_{d}\left(oldsymbol{u}_{1}, oldsymbol{q}_{0}
ight)
ight) + oldsymbol{f}_{1}^{O}}{oldsymbol{P}^{O, T}\left(oldsymbol{q}_{0}^{O}
ight) \cdot \left[oldsymbol{p}_{0}^{O} + D_{1}\mathcal{L}_{d}^{O}\left(oldsymbol{q}_{0}^{O}, oldsymbol{q}_{1}^{O}
ight)
ight]} = oldsymbol{0} \\ oldsymbol{g}^{int}\left(oldsymbol{q}_{0}^{O}
ight) + oldsymbol{p}_{1}^{O}oldsymbol{q}^{O} + D_{1}\mathcal{L}_{d}^{O}\left(oldsymbol{q}_{0}^{O}, oldsymbol{q}_{1}^{O}
ight)
ight] = oldsymbol{0} \end{aligned}$$

The reaching phase extends in the time frame $]T_0, T_k$ [, i.e. from time nodes $n=1,\cdots,N_k-2$. The discrete open chain dynamics follow from Equations (4.31) and (4.32). The gap closure functions g_{C1} are imposed as inequality constraints to ensure non-penetration between fingers and object surfaces

$$\begin{split} \boldsymbol{P}^{T}\left(\boldsymbol{q}_{n}\right)\cdot\left[D_{2}\mathcal{L}_{d}\left(\boldsymbol{q}_{n-1},\boldsymbol{q}_{n}\right)+D_{1}\mathcal{L}_{d}\left(\boldsymbol{q}_{n},\boldsymbol{F}_{d}\left(\boldsymbol{u}_{n+1},\boldsymbol{q}_{n}\right)\right)+\boldsymbol{f}_{n-1}^{+}+\boldsymbol{f}_{n}^{-}\right]&=\boldsymbol{0}\\ \boldsymbol{P}^{O,T}\left(\boldsymbol{q}_{n}^{O}\right)\cdot\left[D_{2}\mathcal{L}_{d}^{O}\left(\boldsymbol{q}_{n-1}^{O},\boldsymbol{q}_{n}^{O}\right)+D_{1}\mathcal{L}_{d}^{O}\left(\boldsymbol{q}_{n}^{O},\boldsymbol{q}_{n+1}^{O}\right)\right]&=\boldsymbol{0}\\ \boldsymbol{g}^{int}\left(\boldsymbol{q}_{n+1}^{O}\right)&=\boldsymbol{0}\\ \boldsymbol{g}_{C1}\left(\boldsymbol{q}_{n+1},\boldsymbol{q}_{n+1}^{O}\right)&>\boldsymbol{0} \end{split}$$

The reaching phase concludes at time T_k , or node $n = N_k$, using Equation (3.9), (3.10) and (3.11) to determine configurations q_k , through u_k and q_k^O . At this time instant, the contact points on the hand and the object are closed. They will stay fixed for the remainder of the manipulation phase in respective body frames

$$egin{aligned} oldsymbol{P}^{T}\left(oldsymbol{q}_{k-1}
ight)\cdot\left[D_{2}\mathcal{L}_{d}\left(oldsymbol{q}_{k-2},oldsymbol{q}_{k-1}
ight)+D_{1}\mathcal{L}_{d}\left(oldsymbol{q}_{k-1},oldsymbol{F}_{d}\left(oldsymbol{u}_{k},oldsymbol{q}_{k-1}
ight)
ight)+D_{1}\mathcal{L}_{d}^{O}\left(oldsymbol{q}_{k-1}^{O},oldsymbol{q}_{k}^{O}
ight)&=oldsymbol{0} \ oldsymbol{q}^{OT}\left(oldsymbol{q}_{k-1}^{O}
ight)\cdot\left[D_{2}\mathcal{L}_{d}^{O}\left(oldsymbol{q}_{k-2}^{O},oldsymbol{q}_{k-1}^{O}
ight)+D_{1}\mathcal{L}_{d}^{O}\left(oldsymbol{q}_{k-1}^{O},oldsymbol{q}_{k}^{O}
ight)
ight]&=oldsymbol{0} \ oldsymbol{g}^{int}\left(oldsymbol{q}_{k}^{O}
ight)&=oldsymbol{0} \ oldsymbol{g}^{int}\left(oldsymbol{q}_{k}^{O}
ight)&=oldsymbol{0} \ oldsymbol{g}_{C1}\left(oldsymbol{q}_{k},oldsymbol{q}_{k}^{O}
ight)&=oldsymbol{0} \ oldsymbol{0} \ oldsymbol{q}_{i}^{OT}\left(oldsymbol{q}_{k},oldsymbol{q}_{k}^{O}
ight)&=oldsymbol{0} \ oldsymbol{0} \ oldsymbol{q}_{i}^{OT}\left(oldsymbol{q}_{k},oldsymbol{q}_{k}^{O}
ight)&=oldsymbol{0} \ oldsymbol{0} \ oldsymbol{0} \ oldsymbol{0} \ oldsymbol{q}_{i}^{OT}\left(oldsymbol{q}_{k},oldsymbol{q}_{k}^{O}
ight)&=oldsymbol{0} \ oldsymbol{0} \ oldsymbol$$

For the next time node, $n = N_k + 1$, the corresponding contact forces are included in the DEL Equations (4.33) with Lagrange multipliers λ_{C1} . The

contact forces, hereafter, are constrained to be pressing on the object, while observing the Coulomb's law for static friction.

$$egin{aligned} oldsymbol{P}^{T}\left(q_{k}
ight)\cdot\left[D_{2}\mathcal{L}_{d}\left(q_{k-1},q_{k}
ight)+D_{1}\mathcal{L}_{d}\left(q_{k},oldsymbol{F}_{d}\left(u_{k+1},q_{k}
ight)
ight)+oldsymbol{f}_{k-1}^{+}+oldsymbol{f}_{k}^{-}\ &-G_{C1}^{T}\left(q_{k}
ight)\cdot\lambda_{C1}
ight]=oldsymbol{0} \\ oldsymbol{P}^{O,T}\left(q_{k}^{O}
ight)\cdot\left[D_{2}\mathcal{L}_{d}^{O}\left(q_{k-1}^{O},q_{k}^{O}
ight)+D_{1}\mathcal{L}_{d}^{O}\left(q_{k}^{O},q_{k+1}^{O}
ight) \\ -G_{C1}^{O,T}\left(q_{k}^{O}
ight)\cdotoldsymbol{\lambda}_{C1}
ight]=oldsymbol{0} \\ oldsymbol{g}^{int}\left(q_{k+1}^{O}
ight)=oldsymbol{0} \\ oldsymbol{g}_{C2}\left(q_{k+1},q_{k+1}^{O}
ight)=oldsymbol{0} \end{aligned}$$

Hereon, the manipulation phase is executed in the $]T_k$, T [, for time nodes $n = N_k, \dots, N-1$. The DEL equations are appended with spherical joint contact constraints g_{C2} and forces, with Lagrange multipliers λ_{C2} . The contact forces are now represented by the gradient of the spherical joint constraints.

$$egin{aligned} oldsymbol{P}^{T}\left(oldsymbol{q}_{n}
ight) \cdot \left[D_{2}\mathcal{L}_{d}\left(oldsymbol{q}_{n-1},oldsymbol{q}_{n}
ight) + D_{1}\mathcal{L}_{d}\left(oldsymbol{q}_{n},oldsymbol{F}_{d}\left(oldsymbol{u}_{n+1},oldsymbol{q}_{n}
ight)
ight) + oldsymbol{f}_{n-1}^{+}+oldsymbol{f}_{n}^{-} \ -oldsymbol{G}_{C2}^{T}\left(oldsymbol{q}_{n}^{O}
ight) \cdot oldsymbol{\lambda}_{C2,n}
ight] = oldsymbol{0} \ oldsymbol{P}^{O,T}\left(oldsymbol{q}_{n}^{O}
ight) \cdot oldsymbol{\lambda}_{C2,n}
ight] = oldsymbol{0} \ oldsymbol{g}^{int}\left(oldsymbol{q}_{n+1}^{O}
ight) = oldsymbol{0} \ oldsymbol{g}_{C2}\left(oldsymbol{q}_{n},oldsymbol{q}_{n}^{O}
ight) = oldsymbol{0} \end{aligned}$$

At final time T, the configuration \mathbf{q}_N^O is bounded. The momenta \mathbf{p}_N and \mathbf{p}_N^O for the hand and the object, respectively, are prescribed and the Legendre transform is again utilised

$$egin{aligned} oldsymbol{P}^{T}\left(oldsymbol{q}_{N}
ight)\cdot\left[oldsymbol{p}_{N}-D_{2}\mathcal{L}_{d}\left(oldsymbol{q}_{N-1},oldsymbol{F}_{d}\left(oldsymbol{u}_{N},oldsymbol{q}_{N-1}
ight)
ight)+oldsymbol{f}_{N}^{+}-oldsymbol{G}_{C2}^{T}\left(oldsymbol{q}_{N}
ight)\cdotoldsymbol{\lambda}_{C2,N}
ight]=oldsymbol{0} \ oldsymbol{P}^{O,T}\left(oldsymbol{q}_{N}^{O}
ight)\cdot\left[oldsymbol{p}_{N}^{O}-D_{2}\mathcal{L}_{d}^{O}\left(oldsymbol{q}_{N-1}^{O},oldsymbol{q}_{N}^{O}
ight)-oldsymbol{G}_{C2}^{O,T}\left(oldsymbol{q}_{N}^{O}
ight)\cdotoldsymbol{\lambda}_{C2,N}
ight]=oldsymbol{0} \ oldsymbol{g}_{C2}\left(oldsymbol{q}_{N},oldsymbol{q}_{N}^{O}
ight)=oldsymbol{0} \end{aligned}$$

In the following subsection we describe the supplementary path constraints, inequality and equality, used in the OCP.

4.4.2 Additional path constraints

The DEL equations of motion prescribe the primary constraints in the non-linear optimisation problem. They are supplanted with constraints on other parameters to perform a particular grasp in the most possible human-like way. We use linear bounds on the optimisation variables that are supplied to the optimiser in the form of upper and lower limits. We also need non-linear bounds that are provided as constraints for quantities such as normal forces or contact angles between the fingers and the object. Following is the list of inequality and equality constraints that are used in this work.

4.4.2.1 Inequality constraints

In addition to the normal force h_{normal} (Equation (3.14)) and frictional force h_{fric} constraints, for the hard (Equation (3.17)) and soft (Equation (3.20)) contact models, as shown in Figure 4.1, we introduce the following inequality constraints.

Joint angle limits The joint angles between the fingers have limits on them due to anatomical constraints such as skin or tendon length limits. For every degree of freedom, there exists an upper and a lower bound, with respect to a particular initial resting position. The joint angles in the director formulation are calculated through the use of relative rotation matrix $\mathbf{R}^{ba} = (\mathbf{R}^a)^T \cdot \mathbf{R}^b$ for successive bodies a,b, where $\mathbf{R}^\dagger = \begin{bmatrix} \mathbf{d}_1^\dagger, \ \mathbf{d}_2^\dagger, \ \mathbf{d}_3^\dagger \end{bmatrix}$ for $\dagger = \{a,b\}$. The matrix \mathbf{R}^{ba} is used to calculate the roll, pitch and yaw, or Cardan angles with the order XYZ, or flexion/extension (α^{ba}) , adduction/abduction (β^{ba}) or pronation/supination (γ^{ba}) , through

$$\alpha^{ba} = \tan^{-1} \left(-\frac{R_{23}^{ba}}{R_{33}^{ba}} \right)$$

$$\beta^{ba} = \tan^{-1} \left(\frac{R_{13}^{ba}}{\sqrt{R_{23}^{ba} + R_{33}^{ba}}} \right)$$

$$\gamma^{ba} = \tan^{-1} \left(-\frac{R_{12}^{ba}}{R_{11}^{ba}} \right)$$
(4.36)

A particular constraint for an angle, say α^{ba} is applied via

$$\boldsymbol{h}_{j}\left(\boldsymbol{q}\right) := \begin{bmatrix} \alpha^{ba} - \theta^{\text{upper}} \\ \theta^{\text{lower}} - \alpha^{ba} \end{bmatrix} \leq \boldsymbol{0}, \tag{4.37}$$

for its respective upper θ^{upper} and lower θ^{lower} limits. For the interphalangeal joints with one degree of freedom, we have $\beta^{ba} = 0$ and $\gamma^{ba} = 0$. For the metacarpal joints with two degrees of freedom, the order flexion/extension followed by adduction/abduction is consistent with the joint modelling and we again have $\gamma^{ba} = 0$. The joint angle limits are imposed for all time steps.

Surface limits S^a and S^O for contact points The contact points ϱ and ϱ^O are constrained to lie on specified areas on the finger and object surfaces, respectively, as introduced in Section 3.3. Since ϱ is chosen as an optimisation variable, the linear bounds are supplied directly to the optimiser. Since ϱ^O are calculated within the optimisation problem, the bounds are applied non-linearly through the relations from Section 3.4..

Contact point normal angle It is possible to position the thumb and index or middle finger using the normals at the contact points to achieve a proper opposition posture while performing grasping. The normal to the digit cylindrical surface at contact point ϱ , is calculated as

$$\boldsymbol{n} = \frac{\varrho(1)\boldsymbol{d}_1 + \varrho(2)\boldsymbol{d}_2}{r},\tag{4.38}$$

where directors d_1, d_2 describe the cylindrical cross-section of the digit and r is its radius. For thumb and index finger normals n^t and n^f , the constraint is written as

$$\boldsymbol{h}_{n}\left(\boldsymbol{q}_{k},\boldsymbol{\varrho}\right):=\left(\boldsymbol{n}^{t}\right)^{T}\cdot\boldsymbol{n}^{f}-\cos\left(\theta_{normal}\right)\leq0$$
 (4.39)

to have an angle of at least θ_{normal} between them. The angle value is chosen as per a particular grasp.

Contact point tangential angle The angle between the normals to the finger digit and the object surfaces at the contact point can be constrained to serve two purposes, firstly to achieve a good grasp posture and secondly to reduce penetration between the two surfaces. While the normal to the finger digit is calculated through Equation (4.38), while the normal for different object surfaces is detailed in Section 3.4. For normals n^f and n^O , the constraint to have an angle $\theta_{\rm tang}$ between them is given as

$$\boldsymbol{h}_t\left(\boldsymbol{q}_k,\boldsymbol{\varrho}\right) := \left(\boldsymbol{n}^f\right)^T \cdot \boldsymbol{n}^O - \cos\left(\theta_{\mathrm{tang}}\right) \le 0$$
 (4.40)

Contact points height This is an additional constraint useful for grasping cylindrical objects, wherein the contact point coordinates along the cylindrical axis are to be within a certain distance of each other to reduce moments occurring due to the normal forces applied by the finger digits. The distance between contact points $(\varrho^O)^t$ and $(\varrho^O)^f$ is constrained to be within a distance d_{height} as

$$\boldsymbol{h}_{height}\left(\boldsymbol{q}_{k}\right) := \left(\left(\boldsymbol{\varrho}^{O}\right)^{t}\left(3\right) - \left(\boldsymbol{\varrho}^{O}\right)^{f}\left(3\right)\right)^{2} - d_{height}^{2} \leq 0 \tag{4.41}$$

Object manipulation constraints In addition to the absolute bounds used to guide the movement of the object in the manipulation phase, it is sometimes helpful to use the object configurations at two different, mostly successive, time nodes to describe specific instructions to drive the object motion. This constraint is highly grasp specific and can be expressed in different ways possible.

$$\boldsymbol{h}_{mani}\left(\boldsymbol{q}_{n}^{O}\right) \leq 0 \tag{4.42}$$

4.4.2.2 Equality constraints

The primary equality constraints in the grasping OCP are the DEL equations of motion listed in Section 4.4.1 and depicted in Figure 4.1, including the initial and final momenta. These are supplemented with the following equality constraints.

Object fix constraints In the reaching phase, as the hand approaches the object, the latter is fixed to the ground with respect to its initial configuration q_{ini}^{O} . This is done through the following constraint

$$g_{f}\left(q_{n}^{O}\right) = \begin{bmatrix} q_{n,1}^{O} - q_{ini,1}^{O} \\ q_{n,2}^{O} - q_{ini,2}^{O} \\ q_{n,3}^{O} - q_{ini,3}^{O} \\ q_{n,4}^{O} - q_{ini,4}^{O} \\ q_{n,7}^{O} - q_{ini,7}^{O} \\ q_{n,10}^{O} - q_{ini,10}^{O} \end{bmatrix} = \mathbf{0} \in \mathbb{R}^{6}.$$

$$(4.43)$$

for $n=1,\ldots,N_k$. The coordinates $\{q_{ini,I}^O\}_{I=1,2,3}$ refers to the location of the object, while each of the value $\{q_{ini,I}^O\}_{I=4,7,10}$ refers to the each of the director. These constraints along with the internal constraints describe the complete configuration of the object for the reaching phase. This constraint vector also causes a force, evaluated as $f_f = -G_f^T \cdot \lambda_f$, where G_f is the constant Jacobian and $\lambda_f \in \mathbb{R}^6$ is the corresponding Lagrange multiplier. The constraint force is included in the object DEL equations of motion in the hybrid dynamical system.

Surface limits S^a and S^O for contact points These constraints have been introduced in Section 3.3 to fix the local coordinates for the contact points on the finger surface from Equation (3.9). For the object, the equality constraint forms the contact gap closure function, which has been covered in Equation (3.10), with examples for box in Equation (3.33) and a cylinder in Equation (3.35).

Finger interphalangeal constraints For the index finger, the flexion motion of the proximal and distal interphalangeal joints (PIP and DIP, respectively) is related through the following equation

$$g_{\theta} = \theta_{DIP} - \frac{2}{3}\theta_{PIP} = 0 \tag{4.44}$$

This results from the underlying tendon structure for flexion and extension

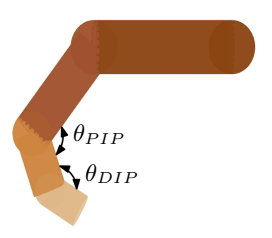


Figure 4.3: The angles for the proximal (θ_{PIP}) and distal (θ_{DIP}) interphalangeal joints in the index finger.

finger movements and makes the hand motion in the reaching phase realistic. The calculation of joint angles is done by evaluating the Euler angles, as done for the inequality constraints. The constraint is imposed differently for the fingers which are used to perform the grasp, and those which are not. For the non-grasp fingers, the constraint is imposed for all time steps. For the fingers which perform object manipulation, the constraint is imposed only for reaching phase, to allow in-hand object manipulation, depending on the grasp type and maneuver.

Object manipulation constraints Similar to the constraints of the same name as described in Section 4.4.2.1, object manipulation can be guided through the use of equality constraints. The constraint formulation is grasp specific, and can be generically described as

$$g_{mani}\left(q_{n}^{O}\right) = 0\tag{4.45}$$

4.4.3 Objective Functions

The primary goal in optimal grasping is to perform force closure grasps with a viable hand configuration while performing a cognitive task. This requires optimal contact locations on the hand and the object to manipulate the object with stability and dexterity. This motivation can be exercised either in the synthesis or evaluation stage for a particular grasp. The methods to evaluate the 'goodness' of a grasp through quality measures has been introduced in Section 3.2. The two indices explained in the section therein are

from an exhaustive list, compiled in [RS14], through a number of objectives encompassing different concepts. These include measures based on the position of contact points, on limitations of finger forces, and on the configuration of the hand. However, quite a few suitable functions are not fit to be used as objectives in the optimal control setting. For example, the grasp isotropy and uniformity of transformation indices are evaluated through the singular value decomposition of matrices which are done algorithmically in numerical computations and are not twice continuously differentiable. Hence, the chances of obtaining a solution from the view of nonlinear constrained optimisation with these objectives range from very low feasibility to near infeasibility. Additionally, many of the measures are either derivatives of each other or inter-dependent, the results of which have been illustrated in [LSBJB⁺12, LMSB14]. With such considerations, the following list of objective functions is presented which are suitable in our grasping optimal control environment.

Unity function (J_0) The grasping nonlinear optimisation problem is solved for feasibility with an objective value of 1. The solution is termed as feasible as it satisfies the nonlinear constraints and works as an initial guess for the subsequent nonlinear objectives.

$$J_0 = 1$$
 (4.46)

Grasp contact polygon centroid (J_1) This kinematic objective is based on the location of the contact points on the object. The possibilities for utilising these are either through the algebraic properties, i.e., using the grasp matrix [LS88] or use their distribution on the object, see [LRSBM14]. These include either the area [MC94, CFMP03], shape [PS92, KOYS01] or the centroid [DLW01, CMFdP05] of the contact polygon. While all three achieves a good spread of the contact points around the object, thereby ensuring an even distribution of the contact forces, the computation of centroid is easier compared to the area or shape. Here, we calculate the centroid of the contact points at the time of closure, through $\varrho^{cen} = \frac{1}{n_c} \sum_{i=1}^{n_c} \left(\varphi^b + \varrho^b_i \right)$. This objective minimises the distance between the object centre of mass φ^O and ϱ^{cen} .

$$J_1 = \frac{1}{2} || \varrho^{cen} - \varphi^O ||^2 \tag{4.47}$$

Rate of change of control torques (J_2) The objectives based on controls, kinetic energy, jerk, joint reaction or time are normally termed as physiologically motivated objectives. As opposed to the other mentioned quantities, the use of controls in minimisation is relatively easier with examples demonstrated for voltage [PSL17], control torques [Koc16, Ley08, ML13] or muscle activations [Maa14, DBF⁺20]. The objective used here minimises the changes in the control torques to ensure a smooth movement of the fingers for the complete simulation duration. This is a form of objective from quantities concerning the hand.

$$J_2 = \frac{1}{2} \sum_{n=1}^{N-2} (t_{n+1} - t_n) \left(\frac{\tau_{n+1} - \tau_n}{t_{n+1} - t_n} \right)^2$$
 (4.48)

The forearm torque values are relatively higher compared to the other joints, on account of the high moment arm used for its movements. Therefore, they are excluded in the evaluation of this objective.

Normal contact force (J_3) The use of contact forces is a physiological objective related to the grasping framework. Referring to the list of quality measures in [RS14], contact forces have found applications in [Pol04, LXWL04], wherein the inverse of the sum of magnitudes of normal components of applied forces is considered as a quality measure. This is an indication of the force efficiency of the grasp with a higher value signifying better quality. Contrary to this, it is required in some cases, especially with precision grasps, to perform a manipulation task with minimum force possible. The normal contact force $f_{in,c}$ on the object at contact point ϱ_c^O is evaluated through the relation in Equation (3.14). Provided the force closure is maintained through the friction force constraint, as expressed in Equation (3.17) or (3.20), we define an objective to minimise the contact forces

$$J_{3} = \frac{1}{2} \sum_{n=N_{L}}^{N} \sum_{c=1}^{n_{c}} f_{in,c}^{2} \left(\mathbf{q}, \mathbf{q}^{O}, \lambda_{c,n} \right)$$
(4.49)

Comfortable joint flexion (J_4) This objective concerns the posture of the finger joints, in a way that they are as much away from their extreme positions as possible. Such an index quantifies the comfortableness of the grasp pose,

see [Lie77, RS14], and is evaluated as

$$J_4 = \frac{1}{2} \sum_{i=1}^{l-m-4} \left(\frac{\theta_i - \theta_{0,i}}{\theta_{max,i} - \theta_{min,i}} \right)^2$$
 (4.50)

Here, θ_i and $\theta_{0,i}$ are the actual and mean joint angle positions for joint i, while $\theta_{max,i}$ and $\theta_{min,i}$ are the maximum and minimum joint angle limits, respectively. This objective is evaluated at the contact closure time node for joint angles excluding the forearm and the wrist.

4.5 Summary

The numerical formulation for the grasping OCP as a hybrid dynamical system with non-smooth dynamics has been developed. The DEL equations of motion in the reaching and manipulation phases of the hybrid system have structure preserving properties due to their derivation using the discrete variational principle. The method to formulate the DEL equations of motion for the kinematic closed loop system during the manipulation phase gives the OCP the required modularity to model grasps with different number of contact points with different configurations. Along with the DEL equations of motion, the OCP is composed of additional equality and inequality constraints with describing the contact point locations, the relative orientation of the finger joints and the orientation of the finger digits during contact closure, the finger joint limits and equations that may be used to guide the object configuration during the manipulation phase. The final part of the chapter discusses three grasp-based and one physiological objective function, two of which are kinematic in nature and two are dynamic. These objectives will be utilized to perform the nonlinear optimisation in the following chapter to simulate grasping actions for three different grasp types.

5 Grasping optimal control simulations

Following on from the formulation for the grasping optimal control problem (OCP) in the previous chapter, we present here the results for four grasping simulations. These include three precision grasps, namely the tip pinch, the lateral pinch and the palmar pinch, see [FRS+16]. The tip pinch grasp, see Fig. 5.1 (a), holds thin cylindrical objects such as a toothpick. This grasp is performed with two contact points for the distal phalanges of the two fingers, see Fig. 5.1 (d). The lateral pinch grasp, see Fig. 5.1 (b), holds thin objects with flat faces such as a key or a credit card. This is simulated with two contact points on the index finger medial phalanx and one contact point on the thumb distal phalanx, see Fig. 5.1 (e). The palmar pinch grasp, see Fig. 5.1 (c), holds thin or thick objects such as a credit card, a dice or a ball. This is simulated with two contact points each on the index finger and the thumb distal phalanges, see Fig. 5.1 (f).

Since the tip pinch is simulated with two contact points, with hard contacts it is not fully constrained as explained in Section 3.2.1. We simulate it twice, each with a hard and soft contact model which sets up a basis for comparison between the two contact models. The other two grasps are simulated only with the hard contact model. Each grasping simulation is a rest-to-rest maneuvers with prescribed initial and final configurations, while minimising each of the four objective functions introduced in Section 4.4.3. The results for each grasp are compared with respect to the final objective function values, the location of the contact points on the fingers and the object, the control torques, the contact forces, the reaching and manipulation phase durations as well as the grasp quality measures. Partial results presented in this chapter have been published in [PRL22].

In Section 5.1, we introduce the simulation parameters for the different grasps, followed by the results for the tip pinch simulation for hard contact (Section 5.2) and soft contact models (Section 5.3), lateral pinch (Section 5.4) and palmar pinch (Section 5.5). Section 5.6 discusses the conclusions.

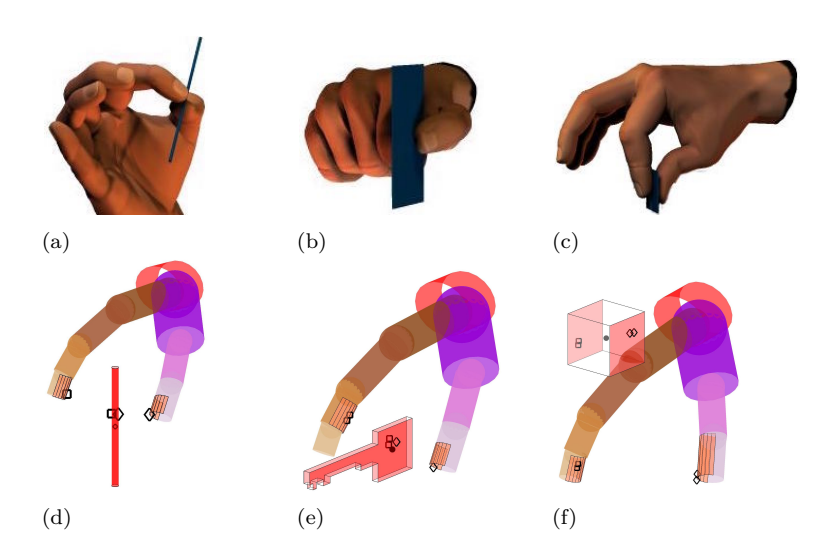


Figure 5.1: The tip, lateral and palmar pinch postures (a) - (c) as taken from [FRS⁺16] and configurations for the simulation with contact points ((\Diamond) for the thumb and (\Box) for the index finger) defined on the fingers for the corresponding grasps (d) - (f). The shaded areas are the limits of the surface areas for the contact points on the different finger digits.

5.1 Simulation parameters

The computational solution of the nonlinear programming is done in MATLAB, using the function $fmincon()^1$ with the sequential quadratic programming (SQP) algorithm to perform the constrained non-linear optimisation. The derivatives for the objectives and constraints are user-written. The bounds on the control torques are taken from the values provided in [NL15]. The bounds on the finger joint angles is realised through nonlinear inequality constraints. A solution is said to be converged with constraint and first-order optimality tolerances of $1e^{-8}$ and $1e^{-4}$, respectively.

¹https://www.mathworks.com/help/optim/ug/fmincon.html

First a feasible solution is determined by running the optimisation problem with the unity objective in Equation 4.46. Its solution X_0 satisfies the equality and inequality constraints, explained in Sections 4.4.1 and 4.4.2 and is then used as the initial guess to the different objectives, so as to maintain parity among the optimal solutions obtained. This serves a good basis for comparison among solutions of the OCP with different objectives. As a remark, we must mention that the minima obtained are local, and not global. The information about the different problem sizes is detailed in Table 5.1. The coefficient of static friction for the Coulomb force constraint is $\mu = 0.7$ [SLZ08]. The initial positions for the hand and object are specified through constraints. The simulation is performed as a rest-to-rest manoeuvre while the final position of object is specified through bounds. The initial value for the reaching and grasping phase durations is 0.1 seconds with 0.01 and 0.5 seconds as lower and upper bounds, respectively. This value is physically very less compared to actual human grasping duration. However, on the one hand, a higher phase duration would require a large number of time steps, which would make the problem computationally extremely challenging. On the other hand, a higher time with the same number of steps will lead to time step duration of the order of 0.1 s, which is quite high for a numerical integrator.

Table 5.1: The table provides the information about the problem size for the optimisation to perform tip, lateral and palmar pinch simulations, with n_c contact points. It details the values for the time steps for the reaching N_k and manipulation N_m phases and the number of optimisation variables X, inequality c, and equality ceq constraints.

grasp	n_c	N_k	N_m	size (X)	size (c)	size (ceq)
tip pinch hard contact	2	7	15	965	694	751
tip pinch soft contact	2	7	15	979	694	765
lateral pinch	3	5	12	779	526	642
palmar pinch	4	6	15	1013	618	813

The results are elaborated for the different grasps with respect to the location of contact points on the digits and the objects, the time evolution for

control torques and the contact forces. The torque profiles are illustrated for the finger MCP and thumb CMC joints, for brevity. The optimal solutions of the different objectives are denoted as X_1, X_2, X_3, X_4 for minimising the objectives J_1, J_2, J_3, J_4 , respectively. The function values for the different solutions are compared with each other across all objectives, with $J_{i,j} = J_i(X_j)$, where $i = 1, \ldots, 4$, represents the objectives and $j = 0, \ldots, 4$, correspond to the initial guess, $J_0 = 1$, and optimal solutions. The results are tabulated for every grasp. The values for the grasp quality measures for different solutions are also compared.

5.2 Tip pinch hard contact model

For the tip pinch grasp, the goal is to hold the curved surface of a thin cylindrical object and raise it to a predefined height, as shown in Figure 5.2 for the feasible initial guess X_0 . This simulation is carried out using the hard contact model for the manipulation phase.

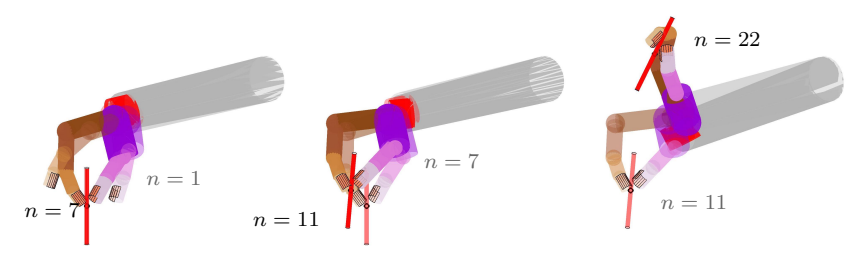


Figure 5.2: Snapshots tip pinch grasping maneuver with hard contacts at different time nodes. Two configurations at different time nodes are superimposed in each of the three pictures. The hand starts from an open posture at n = 1 with grasp closure obtained at $n = N_k = 7$. Thereafter, a lifting task is performed with postures shown for time nodes n = 11, 22.

The function values $J_{i,j}$ for the different objectives and solutions are provided in Table 5.2. It is clear that a local minimum has been obtained for every objective, for example comparing $J_{1,1} = 6.21e^{-8}$ m² while $J_{1,0} = 1.39e^{-3}$ m² or $J_{1,2} = 3.2e^{-4}$ m² for objective J_1 , or comparing $J_{2,2} = 1.39e^{-3}$ m³ or $J_{2,2} = 1.39e^{-3}$ m⁴ or $J_{2,2} = 1.39e^{-3}$ m⁵ or $J_{2,2} = 1.39e^{-3}$ m⁷ or $J_{2,2} = 1.39e^{-3}$ m⁸ or $J_{2,2} = 1.39e^{-3}$ m⁹ or $J_{2,2} = 1.39e^{-3}$ m⁹ for objective $J_{2,2} = 1.39e^{-3}$ m⁹ or $J_{2,2} = 1.39e^{-3}$ m⁹ for objective $J_{2,2} = 1.39e^{-3}$ m⁹ or $J_{2,2} = 1.39e^{-3}$ m⁹ for objective $J_{2,2} = 1.39e^{-3}$ m⁹ or $J_{2,2} = 1.39e^{-3}$ m⁹ for objective $J_{2,2} = 1.39e^{-3}$ m⁹ or $J_{2,2} = 1.39e^{-3}$ m⁹ for objective $J_{2,2} = 1.39e^{-3}$

167.6 N²m²s⁻¹, with $J_{2,0} = 4068$ N²m²s⁻¹ or $J_{2,3} = 4134$ N²m²s⁻¹ for objective J_2 . Apart from the optimal solutions $J_{i,i}$, the function values for other optimal solutions, $J_{i,j}$ with $i \neq j$, are close to that of the respective initial guess $J_{i,0}$, suggesting that the behaviour of the objectives is nearly independent.

Table 5.2: The table shows the evaluation of the different objective functions at the different optimal solutions $J_{i,j}$ while performing tip pinch grasp with hard contacts.

objective	X_0	X_1	X_2	X_3	X_4
J_1	$1.39e^{-3}$	$6.21e^{-8}$	$3.20e^{-4}$	$1.03e^{-3}$	$1.82e^{-5}$
J_2	$4.06e^{3}$	$3.99e^{3}$	$1.67e^{2}$	$4.13e^{3}$	$3.81e^{3}$
J_3	5.08	2.42	2.69	$1.17e^{-7}$	3.98
J_4	$8.75e^{-4}$	$6.81e^{-4}$	$5.69e^{-4}$	$8.5e^{-4}$	$1.27e^{-4}$

Objective J_1

We compare the contact point locations for the different solutions in Figure 5.3. The contact points on the object are closer to its centroid for solution X_1 , than for the initial guess X_0 . The contact points for the other solutions are nearly the same as in the initial guess. This is similar for the contact points on the digits. For X_1 , the finger contact points are near the distal end of the digits, while for the other solutions, the grasp is closed with points on the finger pulp.

Objective J_2

Here, we compare the torque profiles, as shown in Figure 5.4. We observe two contributions for the minimise torque change objective J_2 through the solution X_2 . Primarily, the magnitude of torque and torque changes are substantially reduced compared to the other solutions, which follow the profile from the initial guess X_0 . Secondly, the time taken for the two phases is higher for X_2 compared to the other objectives, as can be seen in Table 5.3

Objectives J_3 and J_4

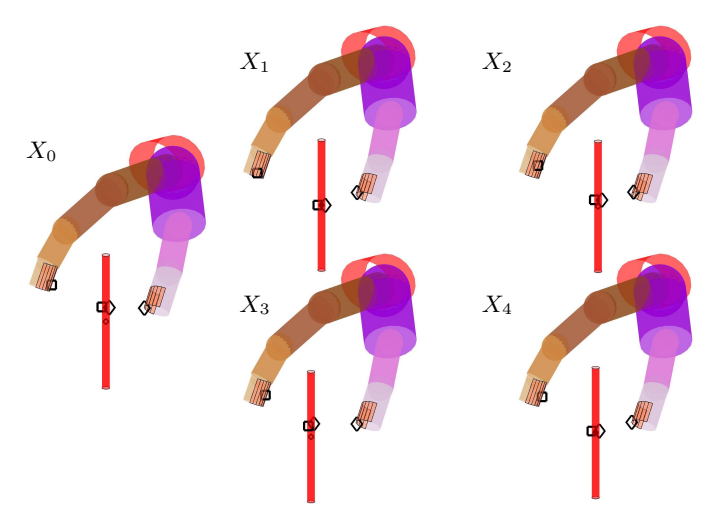


Figure 5.3: Location of the contact points on the finger digits and the object for the different solutions for tip pinch grasp with hard contacts, along with the initial guess.

Table 5.3: The table provides the phase durations in seconds for the different objectives while performing tip pinch grasp with hard contacts.

time	X_0	X_1	X_2	X_3	X_4
reaching phase	0.0247	0.0264	0.0816	0.0248	0.0271
manipulation phase	0.0579	0.0580	0.0754	0.0565	0.0636

Following on, we compare the contact force for the different objectives. The solution X_3 , shows a remarkable decrease in the contact force, while the other solutions follow the time-profile from the initial guess, as shown in Figure 5.5. The quality measures for all solutions is computed as a post-processing quantity, i.e. not minimised, and is summarised in Table 5.4. We

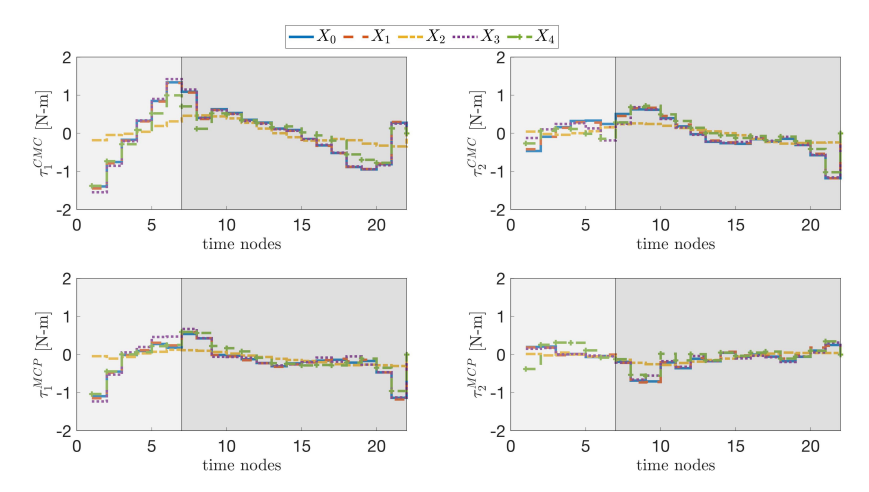


Figure 5.4: Time evolution of the control torques for the different solutions while performing tip pinch grasp with hard contacts, for the thumb CMC joint τ_1^{CMC} (top-left), τ_2^{CMC} (top-right) and the finger MCP joint τ_1^{MCP} (bottom-left), τ_2^{MCP} (bottom-right).

first discuss the grasp isotropy index Q_1 . The values for the different solutions have not improved compared to the initial guess X_0 . For the uniformity of transformation index Q_2 , we see that all the objectives have caused a reduction in the quality value. Even for X_4 , where $Q_2(X_4) = 0.0626$ and is believed to increase hand control as the finger joints are in their most comfortable position, we do not observe an increase, when compared to the initial guess $Q_2(X_0) = 0.0687$. It suggests that a comfortable hand posture does not imply efficient transfer of torques to the contact points. The lowest value is observed for X_3 , i.e. while performing the grasp with minimum contact force. This follows the fact that the force input to object is fairly detached from the torque applied in the finger joints, as can be confirmed by the plots in Figs. 5.4 and 5.5.

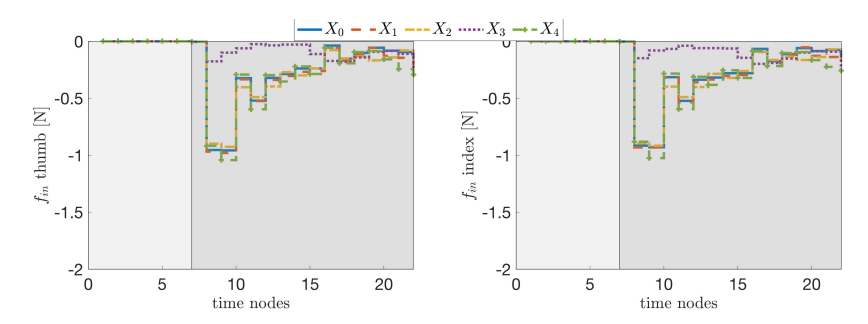


Figure 5.5: Time evolution for the contact forces applied by the finger digits, thumb (left) and index finger (right) on the object for different objectives while performing tip pinch grasp with hard contacts.

Table 5.4: The table shows the grasp quality measures for the different objectives while performing tip pinch grasp.

quality solution	X_0	X_1	X_2	X_3	X_4
Q_1	0.0031	0.0031	0.0031	0.0031	0.0031
Q_2	0.0687	0.0620	0.0645	0.0557	0.0626

5.3 Tip pinch soft contact model

The simulations in this section are performed with the exact same parameters as Section 5.2, except for the fact that the soft contact model is used between the fingers and the cylinder during the manipulation phase. The analysis here would be to compare the results between the different objectives, along with the results from the grasp maneuver with the hard contact model. 5.6 for the feasible initial guess X_0 for the lifting action.

The function values $J_{i,j}$ for the different objectives and solutions are provided in Table 5.5. The values here again indicate a fair amount of independence in that the $J_{i,i}$ is lower for every objective compared to the initial guess, however for solution X_2 and X_4 , we observe that $J_{1,2} = 2.35e^{-5}$ m² and

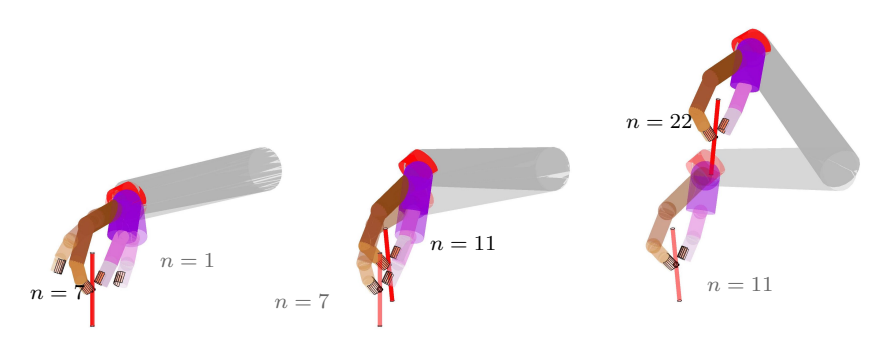


Figure 5.6: Snapshots tip pinch grasping maneuver with soft contacts at different time nodes. Two configurations at different time nodes are superimposed in each of the three pictures. The hand starts from an open posture at n=1 with grasp closure obtained at $n=N_k=7$. Thereafter, a lifting task is performed with postures shown for time nodes n=11,22.

 $J_{1,4} = 1.71e^{-6} \text{m}^2$ are lower that the minima value obtained by minimising J_1 , which is $J_{1,1} = 2.73e^{-5} \text{m}^2$. This anomaly can be either due to the possibility that the optimiser did not either search for a lower minima with J_1 , or that with the additional contact constraint the optimiser found the contact points on the object closer to its centroid as a by-product for X_2 and X_4 .

Table 5.5: The table shows the evaluation of the different objective functions at the different optimal solutions $J_{i,j}$ while performing tip pinch grasp with soft contacts.

objective solution	X_0	X_1	X_2	X_3	X_4
J_1	$6.04e^{-5}$	$2.73e^{-5}$	$2.35e^{-5}$	$6.73e^{-5}$	$1.71e^{-6}$
J_2	$1.14e^{4}$	$1.15e^{4}$	8.43	$1.13e^{4}$	$2.43e^{4}$
J_3	2.26	2.24	2.69	$5.53e^{-1}$	$4.56e^{1}$
J_4	6.17	6.36	5.78	6.06	$4.81e^{-2}$

Objective J_1

The contact point locations for the different solutions are shown in Figure 5.7. As observed from the values in Table 5.5 for row J_1 , the contact points for all but X_3 have moved closer to the centroid. However, only from solution X_1 , we see that the contact points on the fingers have moved with respect to the initial guess. With this movement of the contact points, the optimiser was able to arrive at the minima for J_1 .

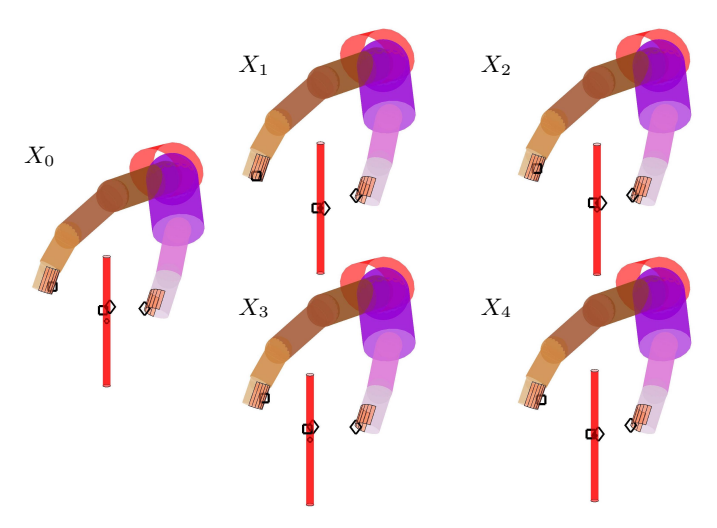


Figure 5.7: Location of the contact points on the finger digits and the object for the different solutions for tip pinch with soft contacts, along with the initial guess.

Objective J_2

Here, we compare the torque profiles, as shown in Figure 5.8. The decrease in torque magnitudes and increase in phase durations (Table 5.3) for solution X_2 with respect to the other objectives is a similar observation that can be made when compared with Figure 5.4. However, we see that torque values for solution X_4 is at least twice compared to the initial guess. This is also seen with the objective value $J_{2,4} = 2430 \text{ N}^2\text{m}^2 \text{ s}^{-1}$ compared to

 $J_{2,0} = 1140 \text{ N}^2 \text{m}^2 \text{s}^{-1}$. This may indicate that the objective J_4 generates disturbed and noisy trajectories with the soft contact model and is perhaps unsuitable in this example.

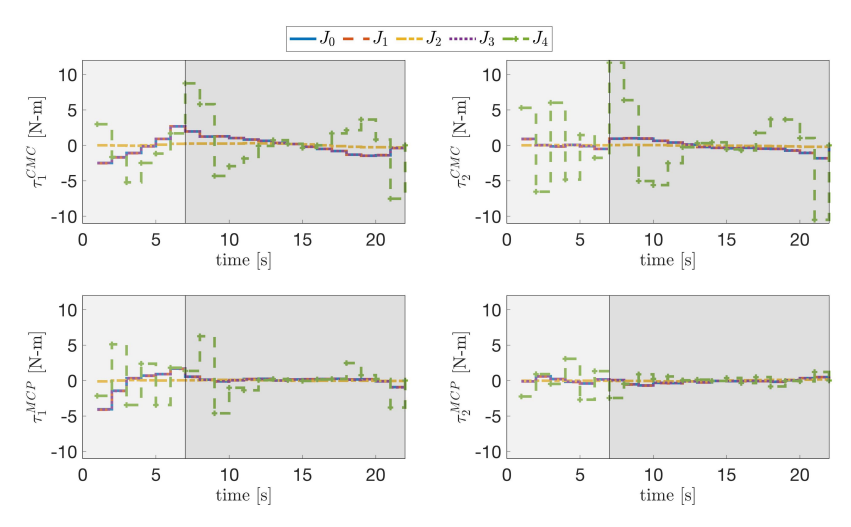


Figure 5.8: Time evolution of the control torques for the different solutions while performing tip pinch grasp with soft contacts, for the thumb CMC joint τ_1^{CMC} (top-left), τ_2^{CMC} (top-right) and the finger MCP joint τ_1^{MCP} (bottom-left), τ_2^{MCP} (bottom-right).

Table 5.6: The table provides the phase durations in seconds for the different objectives while performing tip pinch grasp with soft contacts.

time	X_0	X_1	X_2	X_3	X_4
reaching phase	0.0142	0.0146	0.1163	0.0142	0.0345
manipulation phase	0.0302	0.0304	0.1160	0.0308	0.0474

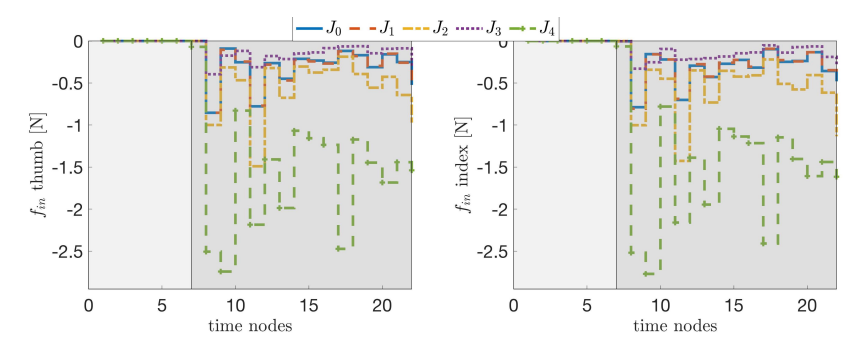


Figure 5.9: Time evolution for the contact forces applied by the finger digits, thumb (left) and index finger (right) on the object for different objectives while performing tip pinch grasp with soft contacts.

Objectives J_3 and J_4

Next, we compare the contact force for the different objectives through the profiles in Figure 5.9. Similar to the observation in Figure 5.5, the solution X_3 shows a remarkable decrease in the contact force profile. However, we observe that the contact forces have increased by an order of 2 for the X_4 solution with respect to the initial guess X_0 complementary to the torque profiles. This further cements the idea that a comfortable hand posture may not be the ideal objective while simulating grasps with the soft contact model. Additionally, we also see that the force profile for solution X_2 is also higher, though not as significantly as X_4 .

The quality measures for all solutions is summarised in Table 5.7. For the grasp isotropy index Q_1 , the values for the different solutions have not improved either when compared to the initial guess X_0 or even with respect to the values in Table 5.4. This indicates that the contact model, whether hard or soft, either does not improve the grasp stability, or perhaps a more complex measure must be used to judge the improvement due to the use of a more complex contact model, provided there is any improvement. The value uniformity of transformation index Q_2 , however, show a marked decrease with the soft contact model, when compared with the values for the hard one. This implies that the overall control is reduced when a contact model with

more friction is used for grasping simulation. Parenthetically, we see that the Q_2 value for solution X_4 has improved compared to X_0 and the lowest value is observed for X_3 , as seen in the hard contact example.

Table 5.7: The table shows the g	rasp quality measure	s for the different
objectives while performing tip pin	ch grasp with soft con	tacts.

quality solution	X_0	X_1	X_2	X_3	X_4
Q_1	0.0031	0.0031	0.0029	0.0031	0.0031
Q_2	0.0117	0.0118	0.0117	0.0116	0.0133

5.4 Lateral pinch

In the lateral pinch grasp, the object is modelled as a key, whose square surfaces are grasped, lifted to a particular height and then a small twist is applied to perform a turning motion, as shown in Figure 5.10.

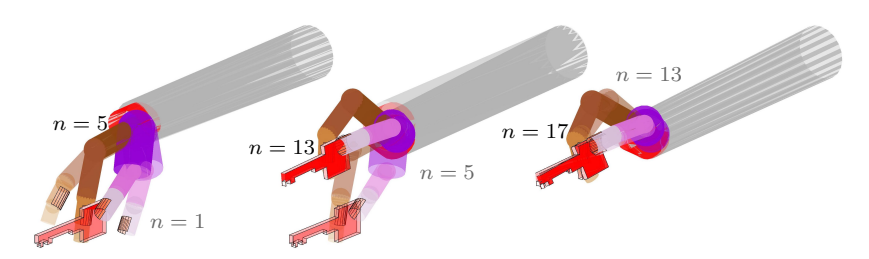


Figure 5.10: Snapshots of the lateral pinch grasping maneuver at different time nodes. Two configurations at different time nodes are superimposed in each of the three pictures. The hand starts from an open posture at n = 1 to hold the sides of the key at $n = N_k = 5$. Thereafter, the key is lifted to a predefined height and orientation at n = 13, after which a clockwise rotation is performed to end the manipulation phase at n = 17.

The function values $J_{i,j}$ for the different optimal solutions are provided in Table 5.8. As in the tip pinch grasp with hard contact model, the objective function values for their $J_{i,i}$ show that the respective minima have been achieved. The independence of the objective functions is observed for all solutions, except for solution X_4 . The $J_{3,4}=10.91~\mathrm{N}^2$ value is much higher compared to the initial guess $J_{3,0}=1.81e^{-3}~\mathrm{N}^2$. This anomaly is reflected in the choice of the contact points, as shown in Figure 5.11 and is further explained below.

Table 5.8: The table shows the evaluation of the different objective functions
at the different optimal solutions $J_{i,j}$ while performing lateral pinch grasp.

objective solution	X_0	X_1	X_2	X_3	X_4
J_1	$1.73e^{-5}$	$4.38e^{-7}$	$3.41e^{-4}$	$2.48e^{-5}$	$1.63e^{-4}$
J_2	$1.01e^{3}$	$1.00e^{3}$	$4.91e^{-2}$	$5.78e^2$	$3.53e^{3}$
J_3	$1.81e^{-3}$	$4.71e^{-3}$	$2.14e^{-2}$	4.55e - 6	$1.09e^{1}$
J_4	6.23	6.18	6.07	6.85	$3.36e^{-1}$

Objective J_1

The contact points for solution X_1 are closer to the object centroid with respect to the initial guess and correspondingly, the finger contact points have moved distally, as shown in Figure 5.11. For X_3 , all the contact points are nearly the same as in the initial guess. For X_2 and X_4 , the finger contact points have moved towards the finger pulp and away from the pulp, respectively. Correspondingly, the object contact points for X_2 and X_4 are in the forward-lower and backward-lower corners, respectively, of the defined square area in the key.

Objective J_2

The solution X_2 for the lateral pinch shows similar behaviour to the tip pinch, in so far as reducing the magnitude of applied torque along with extending the two phase durations, as can be seen in Figure 5.12 and Table 5.9, respectively. For the X_1 and X_3 solutions, the torque profiles follow the initial guess, while for X_4 , the profile is peculiar across all the four joint motions presented, with particular higher values for the thumb CMC joint.

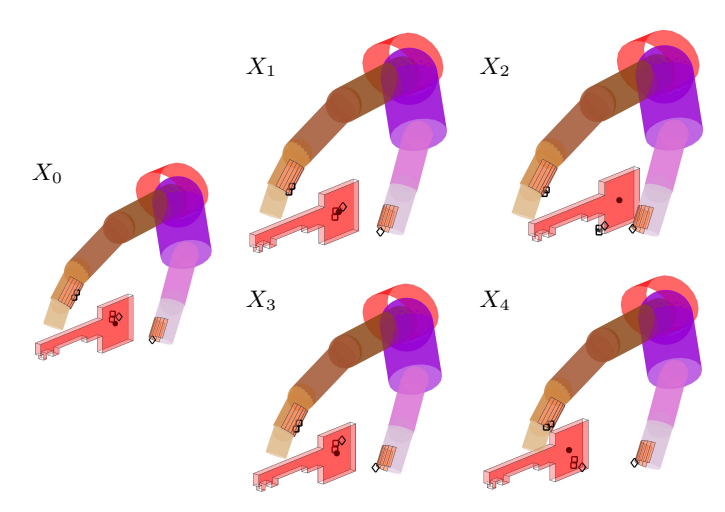


Figure 5.11: Location of the contact points on the finger digits and the object for the different solutions for lateral pinch, along with the initial guess.

Table 5.9: The table provides the phase durations in seconds for the different objectives while performing lateral pinch grasp.

solution	X_0	X_1	X_2	X_3	X_4
reaching phase	0.0216	0.0216	0.1665	0.0204	0.0818
manipulation phase	0.0861	0.0859	0.5522	0.3042	0.1488

Objective J_3 and J_4

The plots in Figure 5.13 show the contact forces for different solutions. They are presented with two separate axes. For X_0 , X_1 , X_2 , and X_3 , we use the left-side vertical axis, while for X_4 , we use the right-side axis. This is due to the fact the contact force values for X_4 , see $J_{3,4}$, are orders of magnitude higher, compared to all other solutions. For solution, X_3 , the decrease in contact force is large, as in the tip pinch. Additionally, we see a

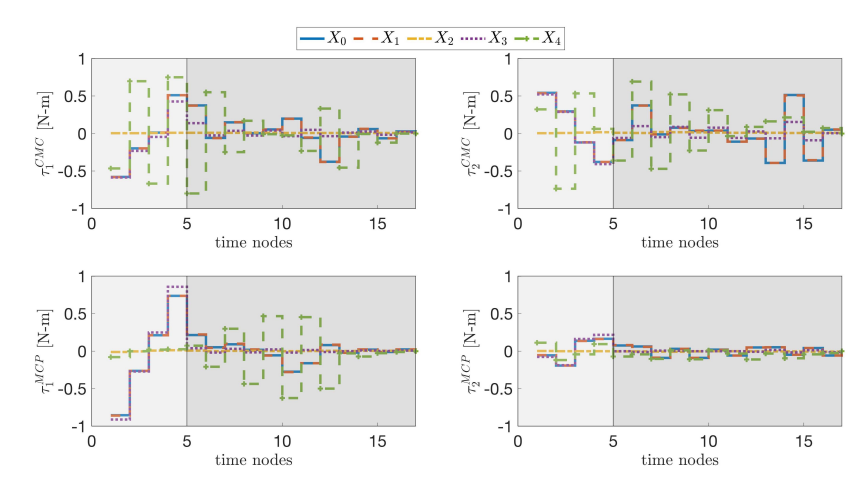


Figure 5.12: Time evolution of the control torques for the different solutions while performing lateral pinch grasp, for the thumb CMC joint τ_1^{CMC} (topleft), τ_2^{CMC} (top-right) and the finger MCP joint τ_1^{MCP} (bottom-left), τ_2^{MCP} (bottom-right).

longer manipulation phase with $T_m = 0.304$ s, compared to the initial guess with $T_m = 0.0861$ s, as seen in Table 5.9. Eventually, we compare the grasp quality values for all the solutions from Table 5.10. For the Q_1 measure, X_1 , X_2 and X_3 solutions values are similar to the initial guess. The X_4 solution has a stark reduction, which can be attributed to the a non-human like grasp due to the contact points in the backward-lower corner of the object. This may explain the uncharacteristic behaviour observed in the contact forces and control torques. The Q_2 quality measure shows a slight improvement for the X_2 solution, i.e. for the minimum torque change objective, suggesting a hand posture is obtained for better transfer of control torques from the fingers joint to perform the grasping action.

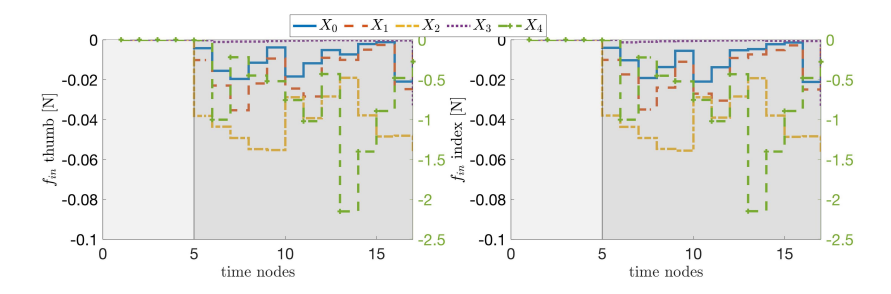


Figure 5.13: Time evolution for the contact forces applied by the finger digits, thumb (left) and index finger (right) on the object for different objectives while performing lateral pinch grasp. For each plot, the force value for solution X_4 is shown with respect to the right-side vertical axis limits.

Table 5.10: The table shows the grasp quality measures for the different objectives while performing lateral pinch grasp.

quality solution	X_0	X_1	X_2	X_3	X_4
Q_1	0.0020	0.0020	0.0018	0.0019	0.0003
Q_2	0.0383	0.0388	0.0500	0.0390	0.0376

5.5 Palmar pinch

The palmar pinch is performed on a cube, whose side surfaces are grasped and then the cube is placed at a specified depth. The motion is shown in Figure 5.14 for solution X_0 .

The function values for the different solutions are provided in Table 5.11. Here again, the minimum values have been obtained for every objective compared to the initial guess. As for the lateral pinch, the $J_{3,4}=360~{\rm N}^2$ value is an aberration, as it is much higher than the other solutions.

Objective J_1

The contact points for solution X_1 are not located around the centres of

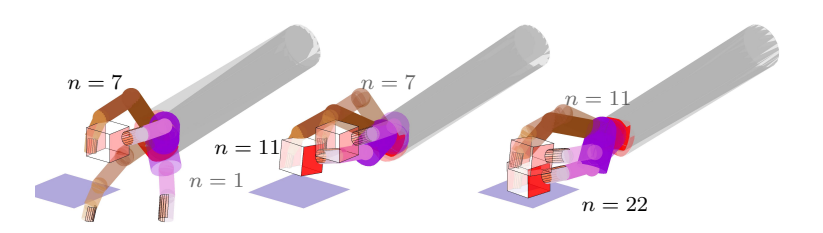


Figure 5.14: Snapshots for the palmar pinch grasping maneuver at different time nodes. Two configurations at different time nodes are superimposed in each of the three pictures. The task is to pick and place a cube from predefined initial and final positions. The hand starts from an open posture n = 1 and closes the grasp at $n = N_k = 7$. The manipulation phase shows the placing motion with time nodes n = 11, 22.

Table 5.11: The table shows the evaluation of the different objective functions at the different optimal solutions $J_{i,j}$ while performing palmar pinch grasp.

1		-,,,		, ,	0 1
objective	X_0	X_1	X_2	X_3	X_4
J_1	$1.55e^{-5}$	$1.04e^{-16}$	$6.27e^{-4}$	$2.43e^{-4}$	$2.08e^{-4}$
J_2	1.13	1.13	$4.35e^{-5}$	1.12	$9.07e^{-1}$
J_3	$4.43e^{-2}$	$4.82e^{-2}$	$3.88e^{-2}$	$1.44e^{-4}$	$3.60e^{2}$
J_4	$7.89e^{-3}$	$7.91e^{-3}$	$6.88e^{-3}$	$5.08e^{-3}$	$1.06e^{-4}$

the object surfaces, unlike the other grasps, as shown in Figure 5.15. For other solutions, the object contact points are very similar to those in the initial guess, except for the thumb-side contact points in X_3 solution. The finger contact points are very close to their initial guess for all solutions. In particular for X_4 , the contact points on the finger and object have overlapped. It's influences on the control torques and contact forces are remarked in the observations below.

Objective J_2

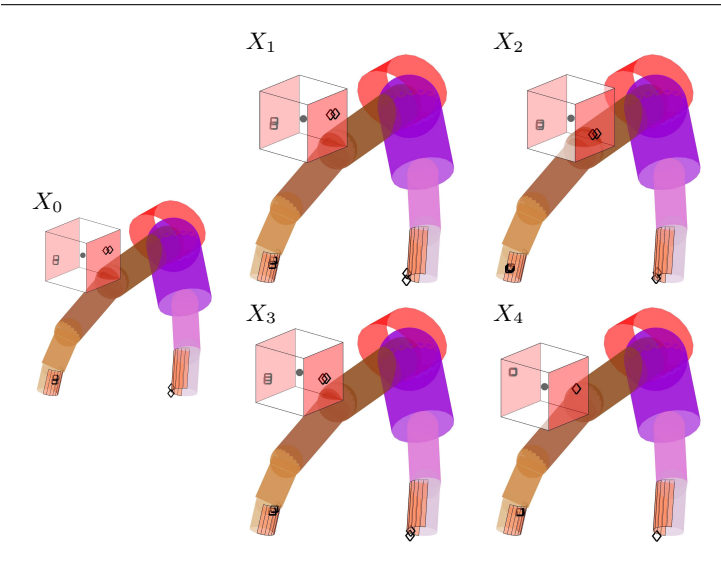


Figure 5.15: Location of the contact points on the finger digits and the object for the different solutions for palmar pinch, along with the initial guess.

Table 5.12: The table shows the grasp quality measures for the different objectives while performing palmar pinch grasp.

solution	X_0	X_1	X_2	X_3	X_4
reaching phase	0.0735	0.0735	0.5000	0.0729	0.3367
manipulation phase	0.1111	0.1108	0.4989	0.1862	0.4870

For the X_2 solution, the control torque profile follow the characteristics from the other two grasps, in terms of reduced magnitude, as shown in Figure 5.16, and higher phase durations, as shown in Table 5.12. The profiles for X_1 and X_4 largely follow the initial guess, while for X_4 , the magnitude is comparatively higher, while not following the torque change profile, compared to the initial guess.

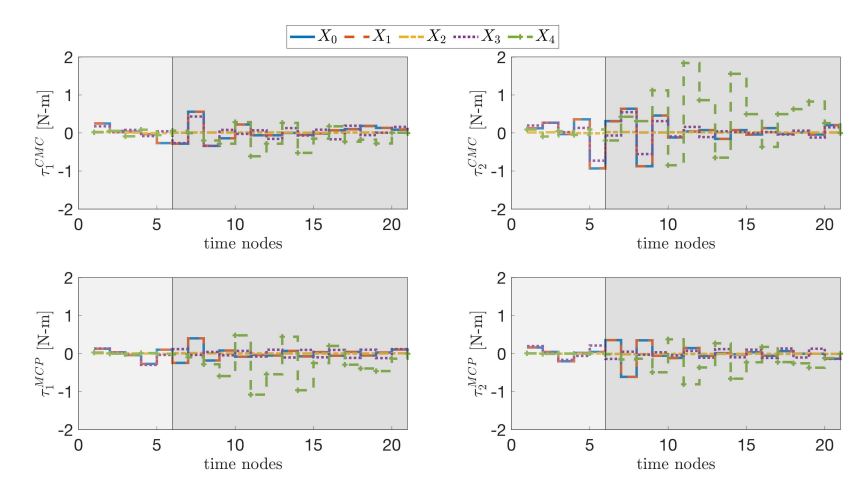


Figure 5.16: Time evolution of the control torques for the different solutions while performing palmar pinch grasp, for the thumb CMC joint τ_1^{CMC} (top-left), τ_2^{CMC} (top-right) and the finger MCP joint τ_1^{MCP} (bottom-left), τ_2^{MCP} (bottom-right).

Objective J_3 and J_4

The contact force profiles are similar to the lateral pinch grasp, as shown in Figure 5.17. The force magnitude for X_4 is a number of magnitudes higher compared to the other solutions, and is shown with respect to the right-side vertical axis in the plots in Figure 5.17. This is irrespective of the location of object contact points which are very close to the initial guess, and can be therefore suggested to be depending on the finger joint angle orientation and contact point locations. In other words, a comfortable hand pose requires higher contact forces to perform the same manipulation action, when compared to the other objectives. The quality measure Q_1 shows good consistency for all the solutions with respect to the initial guess, as can be seen in Table 5.13. For the Q_2 measure, the values show a small reduction column-wise from X_1 to X_3 , while for X_4 , the reduction is relatively higher.

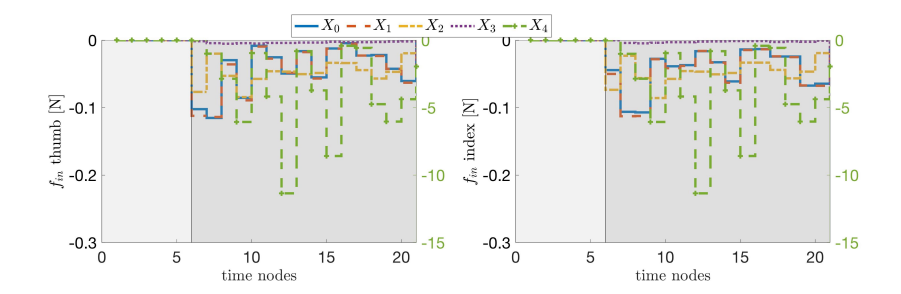


Figure 5.17: Time evolution for the contact forces applied by the finger digits, thumb (left) and index finger (right) on the object for different objectives while performing palmar pinch grasp. For each plot, the force value for solution X_4 is shown with respect to the right-side y-axis limits.

Table 5.13: The table compares the grasp quality measures for the different objectives while performing palmar pinch grasp.

quality solution	X_0	X_1	X_2	X_3	X_4
Q_1	0.0020	0.0020	0.0020	0.0020	0.0019
Q_2	0.0609	0.0606	0.0593	0.0519	0.0378

5.5.1 Overall observations

Here, we summarise the observations across the different grasps and contact models for the same objective functions. For instance, while minimising the polygon contact centroid or J_1 function, the contact points need neither give a configuration with least possible minimum from an initial guess, as seen in the tip pinch soft contact model, nor be necessarily close to the object centroid even with the minimum possible value, as seen in palmar pinch. The latter especially indicates that with higher number of contact points, their spread will not necessarily be better. At the same time, there is no improvement in either of the quality measures to suggest better control. While minimising the rate of torque change with objective J_2 , the torque magnitude also reduces

with an increase in the phase durations. The contact force is unaffected for simulations with hard contact model with a marked increase for simulation with the soft contact model, while the hand singularity quality measure Q_2 shows improvement, except for tip pinch. While minimising the J_3 objective, only the contact forces, through the Lagrange multipliers, is affected, while keeping all the other observed attributes similar to the initial guess. The solutions obtained by minimising J_4 objective are most peculiar. The torque profiles show a noticeable disturbance when compared to the initial guess, while the contact forces are a few magnitudes of order higher than for all other solutions. The Q_1 and Q_2 quality measures for lateral and palmar pinches, respectively, are much lower compared to all other respective values, as shown in Figure 5.18. For the tip pinch in particular, we observe that while Q_1 values are the same across all objectives and contact models, the Q_2 values are quite lower for the grasp with soft contacts when compared with hard contacts. The normal force required in the soft contact model is higher and the hand configuration to obtain such high forces results in far from ideal hand postures that accompany high Q_2 values.

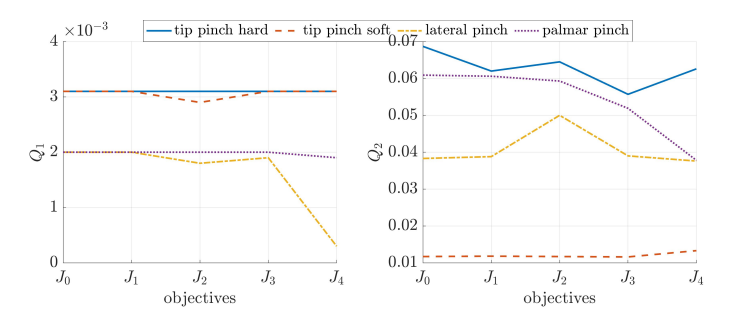


Figure 5.18: The grasp quality measures Q_1 (left) and Q_2 (right) for the different objectives J_1, \ldots, J_4 and the initial guess J_0 .

In general, we can say that while the minimisation of individual objectives fairly result in solutions which are their local minimum with their minima values lower than their respective initial guess, the use of an individual objective will not necessarily replicate the actual human grasping motion. This suggests the move to using a combination of the J_1 objective with

either J_2 or J_3 to obtain appropriate contact point locations along with smoother dynamic characteristics. While the objective J_4 can be considered a good kinematic measure while performing static postures, in case of dynamic manuevers it is not an ideal objective as seen from the torque and contact force profiles. Also, the inclusion of soft contact models, while imparting complete force closure to the tip pinch grasp, does not improve the grasp quality measures.

5.6 Summary

The chapter presented the results from the nonlinear optimisation for the grasping OCP across three distinct precision grasps, four objective functions and two contact models. For different grasps with the hard contact model, the individual objective functions generate solutions with local minimum signifying their independence. On the other hand, with the soft contact model, the results are not as consistent and therefore do not indicate suitability and robustness for grasps where force closure is achieved through hard contacts. The grasp isotropy index quality values does not indicate a change in grasp stability for different objectives as they remain fairly the same with respect to the initial guess, while the uniformity of transformation index shows variation across grasps, suggesting either the use of object-related objectives or a different quality measure to capture grasp stability behaviour in a better way.

As a future work, the objectives may be used in combination in series or parallel to achieve composite characteristics of the underlying individual objectives. While a parallel combination requires the use of appropriate weighting factors to scale the objectives so that the objective function values are of similar order, the series combination is better suited since the objectives have demonstrated independence and the estimation of weights for a parallel setup is non-trivial and tedious.

6 Synergy Effectiveness

We have demonstrated two-finger precision grasp examples in Chapter 5 with the discrete mechanics and optimal control with constraints (DMOCC, see [LOBMO10]) approach in Chapters 4 and 5. While it is logical to extend the biomechanical model to the full hand, the size of the overall optimisation problem increases tremendously. This imposes an enormous computational challenge on the optimiser. Fortunately, the human hand exhibits a highly coordinated motion due to its complicated underlying musculoskeletal network, see [Kap81]. The coordinated motion has been quantified into eigen modes, referred to as synergies [SFS98] or eigen grasps [CA09]. The concept of synergies arose from a neuroscience perspective where it was observed that the hand motion can be expressed as a linear combination of a basis of a fairly reduced configuration space. Overall, it was observed that the hand can be kinematically operated through a relatively reduced number of degrees of freedom (DoFs). The objective in this chapter is to implement the kinematic synergies into our multibody grasping framework. Here, we concentrate only on the reaching or prehension phase, so as to only see the viability of using the synergies to be able to close contact as well as possible.

The procedure to integrate synergies in the multibody formulation is done in two ways. Firstly, we perform prehension by varying the number of synergies and minimising objectives to achieve contact closure and compare the grasp performance with a hand model without synergies. Secondly, we control the hand movement in a hybrid way, i.e. through a combination of synergy and non-synergy based model. The chapter begins with the description of the multibody model and the inclusion of synergies in Section 6.1 and the grasp closure objectives minimised to obtain grasp closure in Section 6.2. It is followed by the first set of results in Section 6.3. Thereafter, we discuss the hybrid kinematic actuation and the results thereof in Section 6.4 and Section 6.5, respectively. This chapter uses and extends the work published in [PRBL20].

6.1 Synergy actuated hand model

We describe a rigid body in the director formulation as in Chapters 2 and 3. In short, a body is represented with twelve DoFs with configuration $q = \begin{bmatrix} \varphi^T, d_1^T, d_2^T, d_3^T \end{bmatrix}^T$, with center of mass φ and an orthonomal director triad $\{d_I\}_{I=1,2,3}$. The hand is composed of twenty such rigid bodies connected in a tree like structure through a combination of revolute, cardan and joints with two rotation axes that are non-intersecting and non-orthogonal (nino). With rigid body internal constraints and joint constraints, the model comprises of twenty-six DoFs. These include six DoFs for the wrist such that it is free to move in space and twenty degrees of freedom for the finger joint angles. The complete structure is depicted in Figure 6.1. The motion of the hand in time is approximated by through discrete configuration $q_n \approx q(t_n)$, i.e. the approximate configuration at time node t_n . To update the configuration from time node n to n+1, we apply a discrete nodal reparameterisation

$$\boldsymbol{q}_{n+1} = \boldsymbol{F}_d \left(\boldsymbol{u}_{n+1}, \boldsymbol{q}_n \right) \tag{6.1}$$

Here, u_{n+1} represents the increment in the minimal coordinates from time nodes n to n+1. The finger digit geometries are modelled as cylinders.

Although there are multiple ways to obtain these eigen grasps, see [VPP+14], we focus briefly on the one by Santello, see [SFS98]. Herein, five subjects were made to visualise and mime hand postures for fifty-seven different objects. The joint angles in these poses were captured and a covariance matrix for the captured data was created. Using singular value decomposition, the eigen vectors form the required reduced configuration space or the principal components (PCs), while the corresponding eigen values represented the amount of variance. As per Santello, more than 80% of the posture variance was accounted by the first two PCs. Nevertheless, the study prescribed fifteen PCs, where the fifteenth eigen value or amplitude was approximately zero. The MATLAB Toolbox Syngrasp, see [MGSP15], provides a function SGsantelloSynergies(), which provides the eigen grasps extracted by Santello in the forms of a matrix $S \in \mathbb{R}^{20 \times 15}$. Here, the twenty rows prescribe the joint angles while 15 columns represent the eigen vectors or synergies. The matrix S is ordered column-wise, as per their eigen values in the decreasing order. Using a discrete change in the synergies, say $\boldsymbol{z}_{n+1} \in \mathbb{R}^{n_z}$, the increment in the joint angles u_{n+1} can be be calculated using

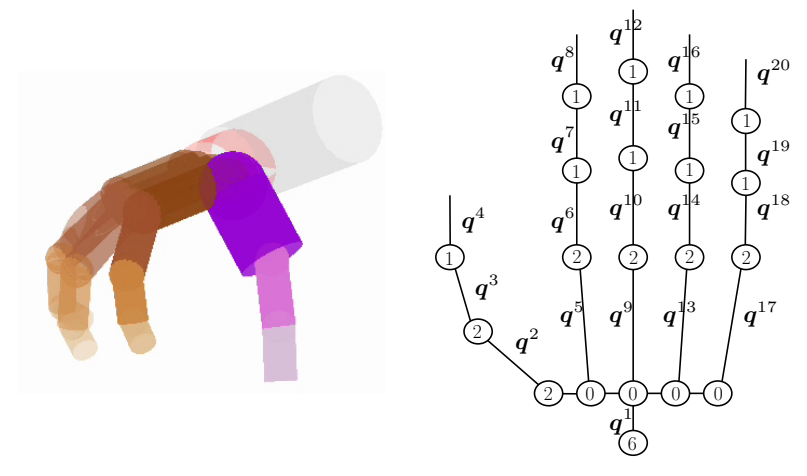


Figure 6.1: The multibody hand model. Left: the modelling of the digits as cylindrical geometries. Right: the tree structure with the number of DoFs in the circles. The one and two DoF joints are modelled as revolute and cardan (fingers) / nino (thumb), respectively.

$$\boldsymbol{u}_{n+1} = \boldsymbol{S} \boldsymbol{z}_{n+1} \tag{6.2}$$

Consequently, Equation 6.1 can now be written as,

$$\mathbf{q}_{n+1} = \mathbf{F}_d \left(\mathbf{S} \mathbf{z}_{n+1}, \mathbf{q}_n \right) \tag{6.3}$$

6.2 Grasp closure objectives

A grasp can be simply described through closure properties, namely form and force closures. While form closure would imply as many contact points as degrees of freedom, force closure would suggest lesser contact points, but maintaining the grasp through friction. The object to be grasped is described with the configuration $\boldsymbol{q}^O = \left[\boldsymbol{\varphi}^{O,T}, \, \boldsymbol{d}_1^{O,T}, \, \boldsymbol{d}_2^{O,T}, \, \boldsymbol{d}_3^{O,T} \right]^T$. The object surface depends on the configuration \boldsymbol{q}^O and certain dimensions such

as radius, length etc. We use a contact point ϱ which is constrained to lie on the finger digit cylindrical surface. These are defined in the digit coordinate system. To close the contact, we define contact closure functions g between the contact point ϱ and the object surface, as shown in Figure 6.2 for a spherical object. For n_c such contact points, we can define an objective

$$J_1 = \sum_{i=1}^{n_c} \left(\boldsymbol{g}_i^T \boldsymbol{g}_i \right), \qquad \boldsymbol{g}_i = \boldsymbol{g}_i \left(\boldsymbol{q}, \boldsymbol{q}^O, \boldsymbol{\rho}_i \right)$$
 (6.4)

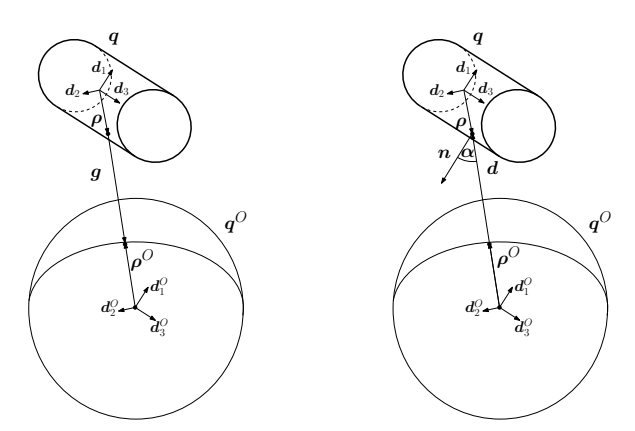


Figure 6.2: Left: the contact closure condition expressed in Equation 6.4. Right: the tangential contact condition expressed in Equation 6.5

The minimisation of J_1 Equation 6.4 will result in grasp closure with no requirement on relative positional orientation and may also result in partial penetrations. To improve the contact, we calculate the cosine of the angle α between the shortest distance \boldsymbol{d} , between the contact point and the object centre, and the normal \boldsymbol{n} to the finger surface at the contact point, see [CA09]. Similar to the contact closure condition, we can write the tangential contact objective as

$$J_2 = \sum_{i=1}^{n_c} (J_{nd_i})^2, \quad \text{where} \quad J_{nd_i} = \left(1 + \frac{\boldsymbol{d}_i^T \boldsymbol{n}_i}{|\boldsymbol{d}_i| \cdot |\boldsymbol{n}_i|}\right)$$
(6.5)

To achieve gap closure which may lead to proper force closure, it is essential to minimise both objectives J_1 and J_2 .

6.3 Synergy kinematics results

We perform a two-fold analysis to determine the synergy effectiveness for grasping. Firstly, the grasping simulation is done for the complete hand model. In this model, we impose coordination between the finger interphalangeal joints and the metacarpophalangeal joints among the fingers through constraints, as described in [LK95]. The posture obtained here is treated as the basis for comparison with the synergy based model. Secondly, we perform grasping with the synergy based model, wherein the simulation is performed with a varying number of synergies. Assuming, we prescribe N time nodes for the optimisation, for n_z synergy optimisation variables, the number of variables reduces by $(26 - n_z) \cdot N$. The main goal here is to determine the minimum number of synergies that needs to be applied to obtain a good grasp in the sense of minimising J_1 or $J_1 + J_2$ objectives. The grasping simulation is performed for two grasps, namely the prismatic 2-finger grasp, i.e. grasping a cylinder, and the tripod grasp, i.e. grasping a sphere. Both grasps are performed with three contact points, one each on the distal phalanges of the thumb, index and middle fingers.

We implement our grasping simulation framework in the MATLAB environment, by firstly optimising the objective

$$J = J_1 \tag{6.6}$$

and thereafter.

$$J = J_1 + J_2 \tag{6.7}$$

subject to the kinematic path constraints, specifically Equation 6.1 for the complete hand model and Equation 6.3 for the synergy based model. The list of optimisation variables include the configuration time history for the hand for N time nodes the location of the contact points with respect to the finger digits. Furthermore, the radius of the object, either cylinder or sphere is provided as an optimisation variable, with bounds, within the range of $\pm 20\%$ of the initial values. As a hand which is constrained to move with respect to a synergy matrix, it is not possible to grasp a single cylinder, the radius

as an optimisation variable provides a degree of flexibility to the optimiser. The optimisation is performed with the interior-point optimiser, IPOPT, see [WB06], with CasADi as a automatic differentiation tool, see [AGH⁺19].



Figure 6.3: Synergy actuated model ($n_z = 15$) with prismatic 2-finger grasp by minimising $J_1 + J_2$ objective. The contact points are shown with (\bullet) symbol.

For the prismatic 2-finger example, the resulting grasp posture is shown in Figure 6.3, with a model actuated through $n_z = 15$ synergies by minimising $J_1 + J_2$ objective. Though the contact is defined for the first three fingers only, we see a coordinated posture for the ring and little fingers as well. We can compare this posture with other models, as shown in Figure 6.4. In Figure 6.4 left, we present a grasp posture for a non-synergy actuated model by minimising $J_1 + J_2$ objective. Here, only the index and middle fingers are flexing to close the contact. The ring and little fingers show little flexion at the metacarpophalangeal and interphalangeal joints due to the behaviour of the optimiser, IPOPT. In Figure 6.4 middle, the grasp posture is obtained by only minimising the J_1 objective for a synergy actuated model with $n_z = 15$, due to which we see clear penetration of the three distal phalanges. This posture explains the need of the tangential contact objective J_2 . We also present the grasp posture obtained with a synergy actuated model with $n_z = 5$ synergies by minimising both $J_1 + J_2$ objectives in Figure 6.4 right. When comparing the different grasp postures, we can clearly observe a variety of contact points. In particular, the inclusion of the tangential contact objective leads to an increased contact area.

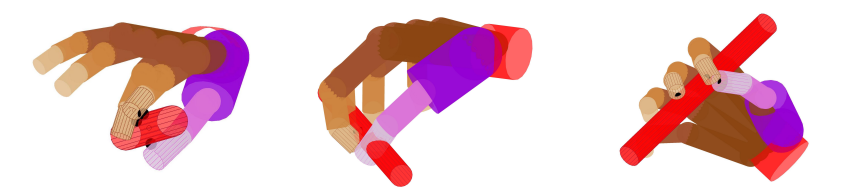


Figure 6.4: From left to right, we see the grasp posture for prismatic 2-finger grasp with (left) non-synergy actuated model while minimising $J_1 + J_2$ objectives, (middle) synergy actuated model with $n_z = 15$ synergies and only J_1 objective to be minimised and (right) synergy actuated model with $n_z = 5$ synergies while minimising $J_1 + J_2$ objectives. The contact points are shown with (\bullet) symbol.

The objective values for the synergy analysis is shown in Table 6.1. It can be observed that the objective value stays at the same order (10^{-12}) when performing the grasp from 15 synergies to 5 synergies. The values, thereafter till 3 synergies, are still acceptable though higher than 10^{-12} . The optimiser could not obtain solutions with lesser number of synergies. It can be comfortably asserted that this grasping simulation can be performed with 5 synergies while minimising $J_1 + J_2$ objectives. However, when solved with only J_1 objective, we can see that it is possible to obtain gap closure from the last column in Table 6.1 even with a single synergy.

For the tripod grasp we see a similar grasp performance when the model is actuated with $n_z=15$ and $n_z=5$ synergies in Figure 6.5, left and right respectively, while minimising J_1+J_2 objective. With $n_z=15$, the index and ring fingers are closer to each other as compared to the posture obtained with $n_z=5$ synergies, which also lead to different contact points. The objective values retains a similar order $\left(10^{-11}\right)$ with even 3 synergies, as seen in Table 6.2, exhibiting a substantial reduction in the number of actuated DoFs. Thereafter, it is still possible to obtain solutions with slightly higher objective values while using even a single synergy. As with the previous grasp, it is possible to obtain grasp postures while minimising only J_1 objective for all possible synergy combinations.

Table 6.1: Objective values for synergy actuated model with prismatic 2-finger grasp. The $J_1 + J_2$ column shows objective function values by minimising function in Equation (6.7), with J_1 and J_2 columns showing the component values. The column only J_1 shows objective function values while minimising Equation (6.6).

•					
	number of synergies	$J_1 + J_2$	J_1	J_2	only J_1
	15	$-6.06e^{-14}$	$2.10e^{-12}$	$-2.16e^{-12}$	$1.46e^{-13}$
	14	$-2.87e^{-12}$	$1.04e^{-12}$	$-3.92e^{-12}$	$7.01e^{-14}$
	13	$1.31e^{-11}$	$2.41e^{-12}$	$-1.55e^{-11}$	$7.83e^{-14}$
	12	$-1.56e^{-12}$	$2.23e^{-12}$	$-3.79e^{-12}$	$2.17e^{-13}$
	11	$2.00e^{-12}$	$2.00e^{-12}$	$-2.11e^{-15}$	$1.70e^{-13}$
	10	$5.82e^{-10}$	$2.92e^{-12}$	$5.79e^{-10}$	$2.21e^{-13}$
	9	$-1.67e^{-13}$	$2.79e^{-12}$	$-2.96e^{-12}$	$3.01e^{-13}$
	8	$9.89e^{-12}$	$9.96e^{-12}$	$-7.04e^{-14}$	$1.24e^{-13}$
	7	$-4.21e^{-12}$	$2.91e^{-12}$	$-7.12e^{-12}$	$1.29e^{-13}$
	6	$4.63e^{-12}$	$5.80e^{-12}$	$-1.17e^{-12}$	$1.02e^{-13}$
	5	$3.32e^{-12}$	$6.09e^{-12}$	$-2.77e^{-12}$	$4.85e^{-13}$
	4	$8.64e^{-09}$	$8.65e^{-09}$	$-1.57e^{-11}$	$2.40e^{-12}$
	3	$1.06e^{-05}$	$1.06e^{-05}$	$2.72e^{-10}$	$1.29e^{-13}$
	2				$8.93e^{-14}$
	1				$1.18e^{-13}$

6.4 Hybrid kinematics

The optimal control grasping simulations are performed with contact closure as holonomic constraints. An acceptable closure is considered to be with an objective value of the order of approximately 10^{-12} , which is close to the order of constraint tolerance in the optimal control problem. Also, as seen in the

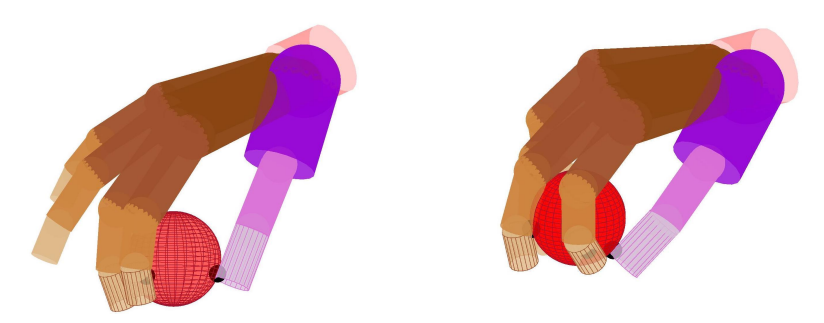


Figure 6.5: Synergy actuated model with tripod grasp, see [FRS⁺16], with $n_z=15$ (left) and $n_z=5$ synergies. The contact points are shown with (\bullet) symbol.

previous section, it is not straightforward to use the same number of synergies to close grasp for different object shapes. To overcome the limitations on the choice of number of synergies to use along with better non-penetration between fingers and object, it is viable to couple the synergy based model with the constraint based model. This is done such that for a majority of the time, the synergy based model from Equation (6.3) is applied while avoiding object penetration, while for the last few time nodes individual joint angles are calculated from Equation (6.1) to close the grasp.

The optimisation problem is expressed as minimisation of the tangential contact function

$$J = J_2 \tag{6.8}$$

as compared to Equation (6.7) as gap functions in Equation (6.4) are included in the optimisation problem as equality constraints. Additionally, it is ensured that at the end of the synergy phase, the gap between the finger and object surfaces is in the range of less than $1\ mm$. This makes it certain that the synergy actuation performs majority of the reaching movement. The other constraints used in this setup are position of contact points on the fingers as equality constraints, and joint angle limits as inequality constraints. The configuration evolution for the synergy and constraint based actuation is,

Table 6.2: Objective values for synergy actuated model with tripod grasp. The columns description follows from Table 6.1.

number of synergies	$J_1 + J_2$	J_1	J_2	only J_1
15	$1.42e^{-11}$	$2.71e^{-12}$	$1.14e^{-11}$	$4.13e^{-13}$
14	$1.41e^{-11}$	$2.52e^{-12}$	$1.15e^{-11}$	$2.06e^{-12}$
13	$3.38e^{-12}$	$2.59e^{-13}$	$3.12e^{-12}$	$1.32e^{-14}$
12	$4.60e^{-12}$	$4.41e^{-13}$	$4.16e^{-12}$	$3.75e^{-13}$
11	$4.32e^{-12}$	$3.08e^{-13}$	$4.01e^{-12}$	$4.76e^{-12}$
10	$5.68e^{-12}$	$3.93e^{-13}$	$5.21e^{-12}$	$7.70e^{-17}$
9	$6.39e^{-11}$	$7.51e^{-12}$	$5.6e^{-11}$	$3.38e^{-13}$
8	$1.51e^{-11}$	$7.69e^{-13}$	$1.44e^{-11}$	$1.38e^{-12}$
7	$7.07e^{-12}$	$7.60e^{-13}$	$6.31e^{-12}$	$9.56e^{-12}$
6	$5.65e^{-11}$	$3.01e^{-12}$	$5.35e^{-11}$	$3.75e^{-11}$
5	$1.55e^{-11}$	$3.38e^{-13}$	$1.52e^{-11}$	$4.56e^{-13}$
4	$5.38e^{-11}$	$9.57e^{-12}$	$4.43e^{-11}$	$7.12e^{-13}$
3	$4.54e^{-08}$	$4.51e^{-08}$	$2.88e^{-10}$	$2.78e^{-22}$
2	$5.13e^{-06}$	$4.25e^{-06}$	$8.86e^{-07}$	$2.51e^{-10}$
1	$1.59e^{-05}$	$1.35e^{-05}$	$2.44e^{-06}$	$6.99e^{-13}$

therefore, evaluated as

$$q_{i} = \begin{cases} F_{d}(Sz_{i}, q_{0}) & i = 1 \\ F_{d}(Sz_{i}, q_{i-1}) & i = 2, \dots, N - 2 \\ F_{d}(u_{i}, q_{i-1}) & i = N - 1, N \end{cases}$$
(6.9)

6.5 Hybrid kinematics results

We present results for the two grasps introduced in the previous sections, i.e. the prismatic-2-finger and the tripod grasp. Firstly we compare the number of optimisation variables required for the three kinematic update methods in Table 6.3. The grasps are performed with 10 and 2 time steps for the synergy and constraint kinematic phases, respectively. It is executed with the first two i.e., $n_z=2$ synergies with the same bounds on all the optimisation variables as in the previous simulations.

Table 6.3: The table provides the information about the problem size for the optimisation variable X to perform either prismatic-2-finger or tripod grasp simulations, with 3 contact points with 10 time nodes. The number of contact points and object radius is excluded as it is common in the constraint based, synergy based and hybrid kinematic cases. With these exclusions, we get reduced optimisation vector $X_{\rm red}$

kinematics	size (X_{red})
constraint based	$(6+20)\times N$
synergy based	$(6+n_z)\times N$
hybrid	$(6+n_z) \times (N-2) + (6+20) \times 2$

The results for the grasp postures for the prismatic 2-finger grasps are shown in Figure 6.6. In the left, the result for the synergy based grasp is shown, for a simulation for which an acceptable solution was not possible with IPOPT. With the hybrid configuration evolution, the results are shown on the right with an objective value of 3.17×10^{-14} with a smaller radius. To improve the final grasp posture visually, we constrained the thumb contact point to lie in between the index and ring finger contact points along the cylinder axis.

Similarly, the results for the tripod grasp is shown in Figure 6.7. It is again clear that a converged solution with full grasp closure is obtained with the hybrid kinematics (right), as compared to the synergy based model (left), for a slightly larger radius. The objective value for the synergy case is as per the values in Table 6.2, i.e. gap closure value of $5.13e^{-06}$ and tangential contact

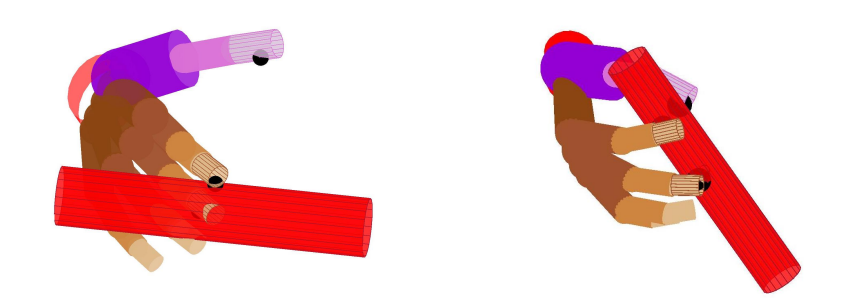


Figure 6.6: Comparison of the grasp postures for Prismatic 2-Finger grasp with the synergy (left) and hybrid (right) kinematic model. Both simulations have been executed with $n_z = 2$ synergies.

value of $4.25e^{-06}$, while for the hybrid case, it is $-4.36e^{-10}$

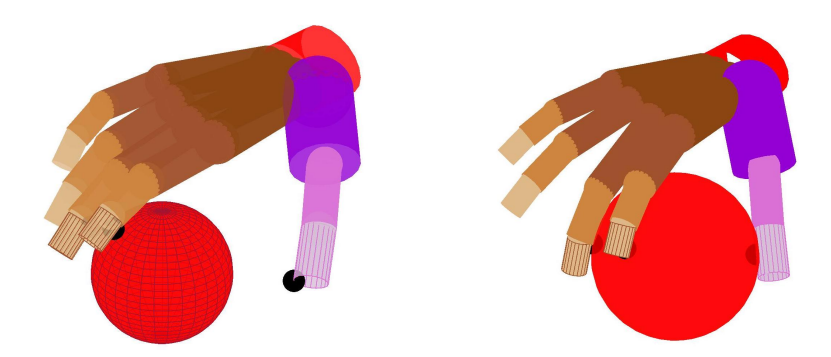


Figure 6.7: Comparison of the grasp postures for tripod grasp with the synergy (left) and hybrid (right) kinematic model. Both simulations have been executed with $n_z = 2$ synergies.

6.6 Conclusions

We have demonstrated a kinematic grasping methodology with coordinated hand motion achieved through synergies. The grasping performance of the synergy based model has been compared with an independent joint model. The synergy analysis shows the possibility of a significant reduction in the number of independent joint angle DoFs. It also enables the formulation of synergistic actuation torques, as per [GBPM11]. This will result in a considerable reduction in problem size when the method is ported to optimal control simulations for grasping where the number of optimisation variables, i.e. DoFs and controls, are multiplied by the number of discrete time nodes. It was further extended to obtain a hybrid kinematic configuration evolution, by augmenting the synergy based model with the constraint based one. This allowed for a further reduction in the model size since the final postures were possible to generate with only 2 synergies.

The method, however, is not free from certain drawbacks. In particular, the kinematic hand model is dependent on the description of the synergy matrix and hence is not readily subject to change. For example, the synergy matrix used in this work from *Syngrasp*, does not allow flexion motion for the ring and little finger CMC joints. Also, the thumb CMC joint is modelled as a universal joint in the synergy matrix. Thus, the thumb cannot perform the passive internal rotation motion as observed in human beings. Thus, to add more realism to the grasps, a kinematically appropriate synergy matrix must be used. The grasps obtained therein will be analysed for force closure properties and their performance will be compared as per grasp quality metrics, as given in [RS14].

7 Conclusions

Summary In this work, an optimal control framework to perform grasping simulations with a human hand is presented. It begins with the examination of the anatomy of the human thumb and its influence in the kinematic modelling of the human hand. It follows with the description of three types of contact models used in grasping simulations. The constraint equations for the contact models form the basis for developing expressions for contact forces and thereafter, the grasp matrix and hand Jacobian. Using discrete mechanics and optimal control with constraints (DMOCC), the aforementioned hand and contact models are utilized with non-smooth dynamics to formulate a nonlinear optimisation problem to describe a grasping action with two phases. The minimisation of this problem through different objective functions demonstrates the robustness of the DMOCC methodology to simulate biomechanical systems.

Relevance The simulation of composite grasping action of reaching and manipulation as a single optimisation problem while describing the dynamics of the object and the hand through structure preserving time-stepping scheme is a new formulation, to the best of the author's knowledge. The inclusion of dynamics through variational integrators avoids the artificial drift in the energy of the system which arise from the black-box commercial time integrators. This gives a heightened sense of confidence in the solutions from minimisation, especially with respect to the controls and contact forces. The OCP methodology to simulate grasping is advantageous when compared to simulators such as OpenGrasp [LUD $^+$ 10], as the simulation environment remains integrated, or the methodology from [ZHZ $^+$ 20] where a multi-level optimisation was used to calculate grasping locations and collision-free trajectories separately.

Findings The use of DMOCC to simulate human grasping is a promising approach. The different objectives used for minimisation provide local minima

with strong independence, though not always with the expected outcome. For instance the contact point locations on the object in the palmar grasp obtained with minimising the grasp contact polygon centroid objective appear near the object corners, which from visual inspection is not the ideal location for the holding an object such as a cube. In the case of the rate of change of control torques objective, the lengthening of the phase durations is an unexpected outcome along with the smoothing of the joint torque profiles. A common consensus can be built towards rejecting the comfortable joint flexion objective across all grasps due to the introduction of disturbances in the contact forces and joint torque profiles. This suggests that the grasp posture is very often far away from the kinematic mean positions at least when performing precision grasps. With respect to the grasp quality measures, the uniformity of transformation index can be leveraged to better understand the hand posture while grasping as the quality values showed marked differences across grasp types and objectives used.

The notion to reduce the grasping optimal control problem size by including kinematic synergies is encouraging, especially through a hybrid kinematic formulation. In path planning problems with long reaching phases, the computational effort can be significantly made lower if the hand is controlled through a reduced number of degrees of freedom for a majority of the time. The kinematic synergy matrix from Santello forms a good starting point and should be improved by developing and testing geometry-based synergy matrices, preferably with the non-intersecting and non-orthogonal axes joint model for the thumb.

Outlook The methodology presented in this thesis can be extended to simulate the complete human model, as demonstrated in [BDC⁺16, XA20] for planning of assembly tasks. Also, in tune with the recent trends of using machine learning techniques to simulate grasping, see [OPN18, KBKH20], grasping optimal control can also be extended to include reinforcement learning, as shown for an upper extremity model in [GB19]. However, the methodology also poses a number of challenges, which form the basis for future work. Notably, the computation time for the optimiser in the current MATLAB environment is very high, suggesting a change of platform to perhaps C++ will be favorable. The inclusion of muscles is desirable to make the biomechanical model more *human*. On the other hand, their utility is debatable due to high

increase in modelling complexity, namely, with respect to the anatomically correct muscle parameters, and their origin and insertion points. Furthermore, the evaluation of other grasp quality measures, such as the Grasp Wrench Space (GWS), see [LMSB14], measure can be used to include a force-based quality metric in the analysis.

Bibliography

- [ACCL79] K N An, E Y Chao, W P Cooney, and R L Linscheid. Normative model of human hand for biomechanical analysis. *Journal of Biomechanics*, 12:775–788, 1979.
- [AGH⁺19] Joel A E Andersson, Joris Gillis, Greg Horn, James B Rawlings, and Moritz Diehl. Casadi: a software framework for nonlinear optimization and optimal control. *Mathematical Programming Computation*, 11:1–36, 2019.
- [AHK⁺09] Minoru Asada, Koh Hosoda, Yasuo Kuniyoshi, Hiroshi Ishiguro, Toshio Inui, Yuichiro Yoshikawa, Masaki Ogino, and Chisato Yoshida. Cognitive developmental robotics: A survey. *IEEE transactions on autonomous mental development*, 1:12–34, 2009.
- [AL20] Ahmad Ali and Ji Yeong Lee. Integrated motion planning for assembly task with part manipulation using re-grasping. Applied Sciences, 10:749, 2020.
- [Ang13] Jorge Angeles. Fundamentals of Robotic Mechanical Systems: Theory, Methods, and Algorithms. Springer Publishing Company, Incorporated, 4th ed. 2014 edition, 2013.
- [BA92] Bryan Buchholz and Thomas J. Armstrong. A kinematic model of the human hand to evaluate its prehensile capabilities. *Journal of Biomechanics*, 25:149–162, 1992.
- [BAG92] Bryan Buchholz, Thomas J. Armstrong, and Steven A. Goldstein. Anthropometric data for describing the kinematics of the human hand. *Ergonomics*, 35:261–273, 1992.

- [BBH11] Antonie J. Van Den Bogert, Dimitra Blana, and Dieter Heinrich. Implicit methods for efficient musculoskeletal simulation and optimal control. *IUTAM Symposium on Human Body Dynamics*, 2:297–316, 2011.
- [BBPB05] Gabriel Baud-Bovy, Domenico Prattichizzo, and Nadia Brogi.

 Does torque minimization yield a stable human grasp?

 Springer Tracts in Advanced Robotics, 18:21–40, 2005.
- [BDC⁺16] Staffan Björkenstam, Niclas Delfs, Johan S Carlson, Robert Bohlin, and Bengt Lennartson. Enhancing digital human motion planning of assembly tasks through dynamics and optimal control. *Procedia CIRP*, 44:20–25, 2016.
- [Bet98] John T Betts. Survey of numerical methods for trajectory optimization. *Journal of guidance, control, and dynamics*, 21:193–207, 1998.
- [BFH99] Ch. Borst, M. Fischer, and G. Hirzinger. A fast and robust grasp planner for arbitrary 3d objects. In *Proceedings 1999 IEEE International Conference on Robotics and Automation*, volume 3, pages 1890–1896 vol.3, 1999.
- [BFH03] C. Borst, M. Fischer, and G. Hirzinger. Grasping the dice by dicing the grasp. In Proceedings 2003 IEEE/RSJ International Conference on Intelligent Robots and Systems (IROS 2003) (Cat. No.03CH37453), volume 4, pages 3692–3697 vol.3, 2003.
- [Bic92] Antonio Bicchi. Optimal control of robotic grasping. In 1992 American Control Conference, pages 778–779, 1992.
- [Bic94] Antonio Bicchi. On the problem of decomposing grasp and manipulation forces in multiple whole-limb manipulation. Robotics and Autonomous Systems, 13:127–147, 1994.
- [Bic00] Antonio Bicchi. Hands for dexterous manipulation and robust grasping: A difficult road toward simplicity. *IEEE Transactions on Robotics and Automation*, 16:652–662, 2000.

- [BK19] Aude Billard and Danica Kragic. Trends and challenges in robot manipulation. *Science*, 364, 2019.
- [BL06] Peter Betsch and Sigrid Leyendecker. The discrete null space method for the energy consistent integration of constrained mechanical systems. part ii: Multibody dynamics. *International Journal for Numerical Methods in Engineering*, 67:499–552, 2006.
- [BLL+18] Staffan Björkenstam, Sigrid Leyendecker, Joachim Linn, Johan S Carlson, and Bengt Lennartson. Inverse dynamics for discrete geometric mechanics of multibody systems with application to direct optimal control. *Journal of Computational and Nonlinear Dynamics*, 13:101001, 7 2018.
- [BMM20] Colin Brown, William McNally, and John McPhee. Optimal control of joint torques using direct collocation to maximize ball carry distance in a golf swing. *Multibody System Dynamics*, 50:323–333, 2020.
- [BNC+17] Staffan Björkenstam, Johan Nyström, Johan S Carlson, Michael Roller, Joachim Linn, Lars Hanson, Dan Högberg, and Sigrid Leyendecker. A framework for motion planning of digital humans using discrete mechanics and optimal control. pages 64–71. Federal Institute for Occupational Safety and Health, 2017.
- [BS01] P. Betsch and P. Steinmann. Constrained integration of rigid body dynamics. Computer Methods in Applied Mechanics and Engineering, 191:467–488, 2001.
- [CA09] Matei T. Ciocarlie and Peter K. Allen. Hand posture subspaces for dexterous robotic grasping. *International Journal* of Robotics Research, 28:851–867, 2009.
- [Cay46] Arthur Cayley. Sur quelques propriétés des déterminants gauches. Journal für die reine und angewandte Mathematik, 1846:119–123, 1846.

- [CB81] Roy D Crowninshield and Richard A Brand. A physiologically based criterion of muscle force prediction in locomotion. *Journal of Biomechanics*, 14:793–801, 1981.
- [CFMP03] Eris Chinellato, Robert B Fisher, Antonio Morales, and Angel P Del Pobil. Ranking planar grasp configurations for a three-finger hand. volume 1, pages 1133–1138. IEEE, 2003.
- [Cha08] Don B Chaffin. Digital human modeling for workspace design.

 Reviews of human factors and ergonomics, 4:41–74, 2008.
- [Che06] Jae-Sook Cheong. Immobilizing grasps for two-and threedimensional objects. PhD thesis, Utrecht University, 2006.
- [CHM⁺15] Joseph J. Crisco, Eni Halilaj, Douglas C. Moore, Tarpit Patel, Arnold Peter C Weiss, and Amy L. Ladd. In vivo kinematics of the trapeziometacarpal joint during thumb extension-flexion and abduction-adduction. *Journal of Hand Surgery*, 40:289– 296, 2015.
- [CLA07] Matei Ciocarlie, Claire Lackner, and Peter Allen. Soft finger model with adaptive contact geometry for grasping and manipulation tasks. In Second Joint EuroHaptics Conference and Symposium on Haptic Interfaces for Virtual Environment and Teleoperator Systems (WHC'07), pages 219–224, 2007.
- [CLCL81] W. P. Cooney, M. J. Lucca, E. Y.S. Chao, and R. L. Linscheid. The kinesiology of the thumb trapeziometacarpal joint. *Journal of Bone and Joint Surgery - Series A*, 63:1371–1381, 1981.
- [CM06] L.Y. Chang and Y. Matsuoka. A kinematic thumb model for the act hand. In Proceedings 2006 IEEE International Conference on Robotics and Automation, 2006. ICRA 2006., pages 1000–1005, 2006.
- [CMA05] Matei Ciocarlie, Andrew Miller, and Peter Allen. Grasp analysis using deformable fingers. 2005 IEEE/RSJ International

Conference on Intelligent Robots and Systems, IROS, pages 3579–3585, 2005.

- [CMFdP05] Eris Chinellato, Antonio Morales, Robert B. Fisher, and Angel P. del Pobil. Visual quality measures for characterizing planar robot grasps. IEEE Transactions on Systems, Man and Cybernetics Part C: Applications and Reviews, 35:30–41, 2005.
- [CMM⁺08] P. Cerveri, E. De Momi, M. Marchente, N. Lopomo, G. Baud-Bovy, R. M.L. Barros, and G. Ferrigno. In vivo validation of a realistic kinematic model for the trapezio-metacarpal joint using an optoelectronic system. *Annals of Biomedical Engineering*, 36:1268–1280, 2008.
- [CMM⁺10] P. Cerveri, E. De Momi, M. Marchente, G. Baud-Bovy, P. Scifoc, R. M.L. Barros, and G. Ferrigno. Method for the estimation of a double hinge kinematic model for the trapeziometacarpal joint using mr imaging. Computer Methods in Biomechanics and Biomedical Engineering, 13:387–396, 2010.
- [COA76] E Y Chao, J D Opgrande, and F E Axmear. Three-dimensional force analysis of finger joints in selected isometric hand functions. *Journal of Biomechanics*, 9:387–IN2, 1976.
- [Cra09] John J Craig. Introduction to robotics: mechanics and control, 3/E. Pearson Education India, 3rd edition, 2009.
- [Cut89] Mark R Cutkosky. On grasp choice, grasp models, and the design of hands for manufacturing tasks. IEEE Transactions on Robotics and Automation, 5:269–279, 1989.
- [DBF⁺20] Christopher L Dembia, Nicholas A Bianco, Antoine Falisse, Jennifer L Hicks, and Scott L Delp. Opensim moco: musculoskeletal optimal control. PLOS Computational Biology, 16:e1008493, 2020.

- [DIL13] Konstantinos Dermitzakis, Andreas Ioannides, and Hwai-ting Lin. Robotic thumb grasp-based range of motion optimisation. In 2013 35th Annual International Conference of the IEEE Engineering in Medicine and Biology Society (EMBC), pages 3163–3166, 2013.
- [dJB94] Javier García de Jalón and Eduardo Bayo. Kinematic and Dynamic Simulation of Multibody Systems. Springer, 1 edition, 1994.
- [DLW01] Dan Ding, Yun-Hui Lee, and Shuguo Wang. Computation of 3-d form-closure grasps. *IEEE Transactions on Robotics and Automation*, 17:515–522, 2001.
- [Duf08] Vincent G Duffy. Handbook of digital human modeling: research for applied ergonomics and human factors engineering. CRC press, 2008.
- [EKS83] Herbert Edelsbrunner, David Kirkpatrick, and Raimund Seidel. On the shape of a set of points in the plane. *IEEE Transactions on information theory*, 29:551–559, 1983.
- [FC92] Carlo Ferrari and John Canny. Planning optimal grasps. volume 3, pages 2290–2295, 1992.
- [Fla13] Kathrin Flaßkamp. On the Optimal Control of Mechanical Systems - Hybrid Control Strategies and Hybrid Dynamics. PhD thesis, University of Paderborn, 2013.
- [FRS⁺16] Thomas Feix, Javier Romero, Heinz-Bodo Schmiedmayer, Aaron M Dollar, and Danica Kragic. The grasp taxonomy of human grasp types. *IEEE Transactions on Human-Machine* Systems, 46:66–77, 2016.
- [GAI19] Manuel Graña, Marcos Alonso, and Alberto Izaguirre. A panoramic survey on grasping research trends and topics. *Cybernetics and Systems*, 50:40–57, 2019.

- [GB19] Simon Gottschalk and Michael Burger. Reinforcement learning in order to control biomechanical models. In *Progress in Industrial Mathematics at ECMI 2018*, pages 521–527. Springer, 2019.
- [GBPM11] M. Gabiccini, A. Bicchi, D. Prattichizzo, and M. Malvezzi. On the role of hand synergies in the optimal choice of grasping forces. Autonomous Robots, 31:235–252, 2011.
- [GCH⁺21] Caelan Reed Garrett, Rohan Chitnis, Rachel Holladay, Beomjoon Kim, Tom Silver, Leslie Pack Kaelbling, and Tomás Lozano-Pérez. Integrated task and motion planning. *Annual review of control, robotics, and autonomous systems*, 4:265–293, 2021.
- [GHB+95] D. J. Giurintano, A. M. Hollister, W. L. Buford, D. E. Thompson, and L. M. Myers. A virtual five-link model of the thumb. Medical Engineering and Physics, 17:297–303, 1995.
- [GHRZ19] Michael Görner, Robert Haschke, Helge Ritter, and Jianwei Zhang. Moveit! task constructor for task-level motion planning. In 2019 International Conference on Robotics and Automation (ICRA), pages 190–196, 2019.
- [GL19] Daniel Glaas and Sigrid Leyendecker. Variational integrator based optimal feedback control for constrained mechanical systems. ZAMM Journal of Applied Mathematics and Mechanics / Zeitschrift für Angewandte Mathematik und Mechanik, 99:e201700221, 1 2019. https://doi.org/10.1002/zamm.201700221.
- [GM10] Craig M. Goehler and Wendy M. Murray. The sensitivity of endpoint forces produced by the extrinsic muscles of the thumb to posture. *Journal of Biomechanics*, 43:1553–1559, 2010.
- [HBM⁺92] Anne Hollister, William L. Buford, Loyd M. Myers, David J. Giurintano, and Andrew Novick. The axes of rotation of

the thumb carpometacarpal joint. Journal of Orthopaedic Research, 10:454–460, 1992.

- [HD64] Richard Hartenberg and Jacques Danavit. Kinematic synthesis of linkages. New York: McGraw-Hill, 1964.
- [HGB⁺95] Anne Hollister, David J. Giurintano, William L. Buford, Loyd M. Myers, and Andrew Novick. The axes of rotation of the thumb interphalangeal and metacarpophalangeal joints. Clinical Orthopaedics and Related Research, 320:188– 193, 1995.
- [IDX+20] Jeffrey Ichnowski, Michael Danielczuk, Jingyi Xu, Vishal Satish, and Ken Goldberg. Gomp: Grasp-optimized motion planning for bin picking. pages 5270–5277. IEEE, 2020.
- [JBAM20] Néstor J. Jarque-Bou, Manfredo Atzori, and Henning Müller. A large calibrated database of hand movements and grasps kinematics. Scientific Data, 7, 12 2020.
- [JM20] Conor Jansen and John McPhee. Predictive dynamic simulation of olympic track cycling standing start using direct collocation optimal control. *Multibody System Dynamics*, 49:53–70, 2020.
- [JMOB05] Oliver Junge, Jerrold E Marsden, and Sina Ober-Blöbaum. Discrete mechanics and optimal control. *IFAC Proceedings Volumes*, 38:538–543, 2005.
- [Joh13] Gwen Johnson. Modeling, Simulation, and Design of Self-Assembling Space Systems. PhD thesis, California Institute of Technology, 2013.
- [Kap81] I A Kapandji. Biomechanics of the thumb, pages 404–422. Saunders Philadelphia, 1981.
- [KBKH20] Kilian Kleeberger, Richard Bormann, Werner Kraus, and Marco F Huber. A survey on learning-based robotic grasping. Current Robotics Reports, 1:239–249, 2020.

- [Ker84] A D Kerr. On the formal development of elastic foundation models. *Ingenieur-Archiv*, 54:455–464, 1984.
- [KL16] Michael W Koch and Sigrid Leyendecker. Structure preserving optimal control of a three-dimensional upright gait. Multibody Dynamics: Computational Methods in Applied Sciences, pages 115–146, 2016.
- [KLB16] Imin Kao, Kevin M Lynch, and Joel W Burdick. Contact modeling and manipulation, pages 931–954. Springer, 2016.
- [Koc16] Michael Koch. Structure preserving simulation of nonsmooth dynamics and optimal control. PhD thesis, Friedrich-Alexander-Universität Erlangen-Nürnberg (FAU), 2016.
- [KOYS01] Byoung Ho Kim, Sang Rok Oh, Byung Ju Yi, and Il Hong Suh. Optimal grasping based on non-dimensionalized performance indices. volume 2, pages 949–956, 2001.
- [KRL17] M W Koch, M Ringkamp, and S Leyendecker. Discrete mechanics and optimal control of walking gaits. Journal of Computational and Nonlinear Dynamics, 12, 2017.
- [Lan62] J. M. Landsmeer. Power grip and precision handling. *Annals of the rheumatic diseases*, 21:164–170, 1962.
- [LBR00] Qiao Lin, Joel W Burdick, and Elon Rimon. A stiffness-based quality measure for compliant grasps and fixtures. *IEEE Transactions on Robotics and Automation*, 16:675–688, 2000.
- [Ley08] Sigrid Leyendecker. Mechanical integrators for constrained dynamical systems in flexible multibody dynamics. PhD thesis, Technische Universität Kaiserslautern, 2008.
- [Ley11] Sigrid Leyendecker. On optimal control simulations for mechanical systems. Habilitation, Technische Universität Kaiserslautern, 2011.

- [LHK12] Sigrid Leyendecker, Carsten Hartmann, and Michael Koch. Variational collision integrator for polymer chains. *Journal of Computational Physics*, 231:3896–3911, 2012.
- [Lie77] Alain Liegeois. Automatic supervisory control of the configuration and behavior of multibody mechanisms. IEEE Transactions on Systems, Man and Cybernetics, SMC-7:868–871, 1977.
- [LK95] Jintae Lee and Tosiyasu L Kunii. Model-based analysis of hand posture. IEEE Computer Graphics and applications, 15:77–86, 1995.
- [LKL⁺11] Hwai Ting Lin, Li Chieh Kuo, Hsin Yi Liu, Wen Lan Wu, and Fong Chin Su. The three-dimensional analysis of three thumb joints coordination in activities of daily living. Clinical Biomechanics, 26:371–376, 2011.
- [LMO08] S. Leyendecker, J.E. Marsden, and M. Ortiz. Variational integrators for constrained dynamical systems. ZAMM - Journal of Applied Mathematics and Mechanics / Zeitschrift für Angewandte Mathematik und Mechanik, 88:677-708, 2008.
- [LMSB14] Beatriz León, Antonio Morales, and Joaquín Sancho-Bru. From robot to human grasping simulation, volume 19. Springer, Cham, 2014.
- [LOBMO10] S. Leyendecker, Sina Ober-Blöbaum, Jerrold E. Marsden, and M. Ortiz. Discrete mechanics and optimal control for constrained systems. Optimal Control Applications and Methods, 31:505-528, 2010.
- [LRSBM14] Beatriz León, Carlos Rubert, Joaquín Sancho-Bru, and Antonio Morales. Characterization of grasp quality measures for evaluating robotic hands prehension. pages 3688–3693, 2014.
- [LS88] Zexiang Li and S. Shankar Sastry. Task-oriented optimal grasping by multifingered robot hands. *IEEE Journal on Robotics and Automation*, 4:32–44, 1988.

- [LSBJB+12] Beatriz León, Joaquín L. Sancho-Bru, Néstor J. Jarque-Bou, Antonio Morales, and Máximo A. Roa. Evaluation of human prehension using grasp quality measures. *International Journal of Advanced Robotic Systems*, 9, 2012.
- [LUD+10] Beatriz León, Stefan Ulbrich, Rosen Diankov, Gustavo Puche, Markus Przybylski, Antonio Morales, Tamim Asfour, Sami Moisio, Jeannette Bohg, and James Kuffner. Opengrasp: a toolkit for robot grasping simulation. pages 109–120. Springer, 2010.
- [LXWL04] Guanfeng Liu, Jijie Xu, Xin Wang, and Zexiang Li. On quality functions for grasp synthesis, fixture planning, and coordinated manipulation. *IEEE Transactions on Automation* Science and Engineering, 1:146–162, 2004.
- [MA04] Andrew T Miller and Peter K Allen. Graspit! a versatile simulator for robotic grasping. *IEEE Robotics & Automation Magazine*, 11:110–122, 2004.
- [Maa14] Ramona Maas. Biomechanics and optimal control simulations of the human upper extremity. PhD thesis, Friedrich-Alexander-Universität Erlangen-Nürnberg (FAU), 2014.
- [MASV05] Andrew Miller, P Allen, V Santos, and F Valero-Cuevas. From robotic hands to human hands: A visualization and simulation engine for grasping research. *Industrial Robot: An International Journal*, 2005.
- [MC94] B. Mirtich and J. Canny. Easily computable optimum grasps in 2-d and 3-d. In Proceedings of the 1994 IEEE International Conference on Robotics and Automation, pages 739–747 vol.1, 1994.
- [MGS⁺13] Monica Malvezzi, Guido Gioioso, Gionata Salvietti, Domenico Prattichizzo, and Antonio Bicchi. Syngrasp: A MATLAB toolbox for grasp analysis of human and robotic hands. In 2013 IEEE International Conference on Robotics and Automation, pages 1088–1093, 2013.

- [MGSP15] Monica Malvezzi, Guido Gioioso, Gionata Salvietti, and Domenico Prattichizzo. Syngrasp: A MATLAB toolbox for underactuated and compliant hands. IEEE Robotics and Automation Magazine, 2015.
- [MJ85] Matthew T Mason and J Kenneth Salisbury Jr. Robot hands and the mechanics of manipulation. The MIT Press, Cambridge, MA, 1985.
- [MK92] Anil Mital and Asa Kilbom. Design, selection and use of hand tools to alleviate trauma of the upper extremities: Part II—the scientific basis (knowledge base) for the guide. *International Journal of Industrial Ergonomics*, 10:7–21, 1992.
- [MK16] Claudio Melchiorri and Makoto Kaneko. *Robot Hands*, pages 463–480. Springer, 2016.
- [ML13] R. Maas and S. Leyendecker. Biomechanical optimal control of human arm motion. Proceedings of the Institution of Mechanical Engineers, Part K: Journal of Multi-body Dynamics, 227:375–389, 2013.
- [MSL12] Ramona Maas, Tobias Siebert, and Sigrid Leyendecker. On the relevance of structure preservation to simulations of muscle actuated movements. *Biomechanics and modeling in mechanobiology*, 11:543–556, 2012.
- [MSM17] Matthew Millard, Manish Sreenivasa, and Katja Mombaur. Predicting the motions and forces of wearable robotic systems using optimal control. Frontiers Robotics AI, 4:1–12, 2017.
- [MTL10] Katja Mombaur, Anh Truong, and Jean-Paul Laumond. From human to humanoid locomotion—an inverse optimal control approach. *Autonomous robots*, 28:369–383, 2010.
- [MW01] J. E. Marsden and M. West. Discrete mechanics and variational integrators. *Acta Numerica*, 10:357–514, 2001.

- [Nap56] J. R. Napier. The prehensile movements of the human hand. The Journal of bone and joint surgery. British volume, 38 B:902-913, 1956.
- [NDH+20] Marlies Nitschke, Eva Dorschky, Dieter Heinrich, Heiko Schlarb, Bjoern M Eskofier, Anne D Koelewijn, and Antonie J van den Bogert. Efficient trajectory optimization for curved running using a 3D musculoskeletal model with implicit dynamics. Scientific Reports, 10:17655, 2020.
- [Ngu88] Van Duc Nguyen. Constructing force-closure grasps. The International Journal of Robotics Research, 7:3–16, 1988.
- [NL15] Raviraj Nataraj and Zong Ming Li. Integration of marker and force data to compute three-dimensional joint moments of the thumb and index finger digits during pinch. Computer Methods in Biomechanics and Biomedical Engineering, 18:592–606, 2015.
- [OB08] Sina Ober-Blöbaum. Discrete mechanics and optimal control. PhD thesis, University of Paderborn, 2008.
- [oD89] Department of Defence. Human engineering design criteria for military systems, equipment and facilities (mil-std-1472d).

 US Department of Defense Washington, DC, 1989.
- [OPN18] T Osa, Jan Peters, and G Neumann. Hierarchical reinforcement learning of multiple grasping strategies with human instructions. *Advanced Robotics*, 32:955–968, 9 2018. doi: 10.1080/01691864.2018.1509018.
- [ORB⁺20] Marius Obentheuer, Michael Roller, Staffan Björkenstam, Karsten Berns, and Joachim Linn. Comparison of measured emg data with simulated muscle actuations of a biomechanical human arm model in an optimal control framework direct vs. muscle synergy actuation. In Andrés Kecskeméthy and Francisco Geu Flores, editors, *Multibody Dynamics 2019*, pages 26–33, Cham, 2020. Springer International Publishing.

- [PAF94] P D Panagiotopoulos and A M Al-Fahed. Robot hand grasping and related problems: Optimal control and identification. The International Journal of Robotics Research, 13:127–136, 1994.
- [PGFESB+08] Antonio Pérez-González, Carlos Fenollosa-Esteve, Joaquín L Sancho-Bru, Francisco T Sánchez-Marín, Margarita Vergara, and Pablo J Rodríguez-Cervantes. A modified elastic foundation contact model for application in 3d models of the prosthetic knee. Medical Engineering & Physics, 30:387–398, 2008.
- [Pol94] Nancy S. Pollard. Parallel Methods for Synthesizing Whole-Hand Grasps from Generalized Prototypes. PhD thesis, Massachusetts Institute of Technology, 1994.
- [Pol04] Nancy S Pollard. Closure and quality equivalence for efficient synthesis of grasps from examples. *The International Journal of Robotics Research*, 23:595–613, 6 2004. doi: 10.1177/0278364904044402.
- [PRB+17] Uday D Phutane, Michael Roller, Staffan Björkenstam, Joachim Linn, and Sigrid Leyendecker. Kinematic validation of a human thumb model. In ECCOMAS Thematic Conference on Multibody Dynamics, pages 857–866, 2017.
- [PRBL20] Uday Phutane, Michael Roller, Anja Boebel, and Sigrid Leyendecker. Optimal control of grasping problem using postural synergies. In Lars Hanson, Dan Högberg, and Erik Brolin Brolin, editors, DHM2020: Proceedings of the 6th International Digital Human Modeling Symposium, August 31-September 2, 2020, volume 11, pages 206 213. Volume 11: DHM2020, 2020.
- [PRL22] Uday Phutane, Michael Roller, and Sigrid Leyendecker. Optimal control simulations of two-finger grasps. *Mechanism and Machine Theory*, 167:104508, 2022.

[PS92] Young C Park and Gregory P Starr. Grasp synthesis of polygonal objects using a three-fingered robot hand. International journal of robotics research, 11:163–184, 1992. [PSL17] Johann Penner, Tristan Schlögl, and Sigrid Levendecker. Optimal control of a slot car racer. volume 17, pages 537–538. Wiley Online Library, 2017. [PSS⁺97] Jean Ponce, Steve Sullivan, Attawith Sudsang, Jean Daniel Boissonnat, and Jean Pierre Merlet. Computing four-finger equilibrium and force-closure grasps of polyhedral objects. International Journal of Robotics Research, 16:11–35, 1997. [PT16] Domenico Prattichizzo and Jeffrey C Trinkle. Grasping, pages 955–988. Springer, 2016. Elon Rimon and Joel Burdick. On force and form closure [RB96] for multiple finger grasps. Proceedings - IEEE International Conference on Robotics and Automation, 2:1795–1800, 1996. [rC77] W P Cooney 3rd and E Y Chao. Biomechanical analysis of static forces in the thumb during hand function. The Journal of bone and joint surgery. American volume, 59:27–36, 1977. [Reu76] F Reuleaux. The kinematics of machinery (ABW Kennedy, Trans.). Macmilan and Company, Ltd, 1876. [Rod40] O Rodriguez. Des lois geometriques qui regissent les desplacements d'un systeme solide dans l'espace et de la variation des coordonnees provenant de deplacements consideres independamment des causes qui peuvent les produire. J Mathematiques Pures Appliquees, 5:380-440, 1840. [RS14] Máximo A. Roa and Raúl Suárez. Grasp quality measures: review and performance. Autonomous Robots, 38:65–88, 2014. [RSGD19] Jan Rosell, Raúl Suárez, Néstor García, and Muhayy Ud Din. Planning grasping motions for humanoid robots. *International* Journal of Humanoid Robotics, 16:1950041, 12 2019. doi: 10.1142/S0219843619500415.

- [Sac19] Prashant Sachdeva. 3D biomechanical simulation and control of the human hand. PhD thesis, University of British Columbia, 2019.
- [SB00] Joaquin L. Sancho Bru. Model biomecànic de la má orientat al disseny d'eines manuals. PhD thesis, Universitat Jaume I, 2000.
- [SBML⁺14] Joaquín L. Sancho-Bru, Marta C. Mora, Beatriz León, Antonio Pérez-González, José L. Iserte, and Antonio Morales. Grasp modelling with a biomechanical model of the hand. *Computer Methods in Biomechanics and Biomedical Engineering*, 17:297–310, 2014.
- [SC82] J. Kenneth Salisbury and John J. Craig. Articulated hands: Force control and kinematic issues. *The International Journal of Robotics Research*, 1:4–17, 1982.
- [Sch18] Tristan Schlögl. Modelling, simulation and optimal control of dielectric elastomer actuated systems. PhD thesis, Friedrich-Alexander-Universität Erlangen-Nürnberg (FAU), 2018.
- [SEKB12] A. Sahbani, S. El-Khoury, and P. Bidaud. An overview of 3d object grasp synthesis algorithms. *Robotics and Autonomous Systems*, 60:326–336, 2012.
- [SFS98] Marco Santello, Martha Flanders, and John F. Soechting. Postural hand synergies for tool use. *Journal of Neuroscience*, 18:10105–10115, 1998.
- [Shi96] K B Shimoga. Robot grasp synthesis algorithms: A survey. International Journal of Robotics Research, 15:230–266, 1996.
- [SHSvdS14] Georg Stillfried, Ulrich Hillenbrand, Marcus Settles, and Patrick van der Smagt. MRI-based skeletal hand movement model, 2014.
- [Sie12] Ralf Siebert. Mechanical integrators for the optimal control in multibody dynamics. PhD thesis, Universität Siegen, 2012.

- [SKG12] Ali Akbar Samadani, Dana Kulić, and Rob Gorbet. Multi-constrained inverse kinematics for the human hand. pages 6780–6784, 2012.
- [SLZ08] Adriana V Savescu, Mark L Latash, and Vladimir M Zatsiorsky. A technique to determine friction at the fingertips. Journal of applied biomechanics, 24:43–50, 2008.
- [SMF⁺17] Manish Sreenivasa, Matthew Millard, Martin Felis, Katja Mombaur, and Sebastian I Wolf. Optimal control based stiffness identification of an ankle-foot orthosis using a predictive walking model. Frontiers in computational neuroscience, 11:23, 2017.
- [Som00] P Somov. Uber gebiete von schraubengeschwindigkeiten eines starren korpers bie verschiedener zahl von stutzflachen. Z. Mathematik Physik, 45:245–306, 1900.
- [Sou01] P N Soucacos. Indications and selection for digital amputation and replantation. *Journal of Hand Surgery*, 26(6):572–581, 2001.
- [SP19] Sofia Scataglini and Gunther Paul. Chapter 1 from greek sculpture to the digital human model a history of "human equilibrium". In Sofia Scataglini and Gunther Paul, editors, *DHM and Posturography*, pages 3–5. Academic Press, 2019.
- [SS21] Asma Seddaoui and Chakravarthini M Saaj. Collision-free optimal trajectory generation for a space robot using genetic algorithm. *Acta Astronautica*, 179:311–321, 2021.
- [Str98] Oskar Von Stryk. Optimal control of multibody systems in minimal coordinates. ZAMM-Journal of Applied Mathematics and Mechanics/Zeitschrift für Angewandte Mathematik und Mechanik, 78:1117–1120, 1998.
- [SVC06] Veronica J. Santos and Francisco J. Valero-Cuevas. Reported anatomical variability naturally leads to multimodal distributions of denavit-hartenberg parameters for the human thumb.

IEEE Transactions on Biomedical Engineering, 53:155–163, 2006.

- [VCJT03] Francisco J. Valero-Cuevas, M. Elise Johanson, and Joseph D. Towles. Towards a realistic biomechanical model of the thumb: The choice of kinematic description may be more critical than the solution method or the variability/uncertainty of musculoskeletal parameters. *Journal of Biomechanics*, 36:1019–1030, 2003.
- [VDAD10] Nikolaus Vahrenkamp, Martin Do, Tamim Asfour, and Rüdiger Dillmann. Integrated grasp and motion planning. In 2010 IEEE International Conference on Robotics and Automation, pages 2883–2888, 2010.
- [VPP⁺14] Ramana Vinjamuri, Vrajeshri Patel, Michael Powell, Zhi-Hong Mao, and Nathan Crone. Candidates for synergies: Linear discriminants versus principal components. *Computational Intelligence and Neuroscience*, 2014:373957, 2014.
- [WAC+09] John Z. Wu, Kai Nan An, Robert G. Cutlip, Michael E. Andrew, and Ren G. Dong. Modeling of the muscle/tendon excursions and moment arms in the thumb using the commercial software anybody. *Journal of Biomechanics*, 42:383–388, 2009.
- [WB06] Andreas Wächter and Lorenz T Biegler. On the implementation of an interior-point filter line-search algorithm for large-scale nonlinear programming. *Mathematical Programming*, 106:25–57, 2006.
- [WMW20] Alexander Wolf, Jörg Miehling, and Sandro Wartzack. Challenges in interaction modelling with digital human models—a systematic literature review of interaction modelling approaches. *Ergonomics*, 63:1442–1458, 2020.
- [XA20] Yujiang Xiang and Asif Arefeen. Two-dimensional team lifting prediction with floating-base box dynamics and grasping force coupling. *Multibody System Dynamics*, 50:211–231, 2020.

- [YSY⁺15] Xuyao Yu, Yao Shi, Hui Yu, Tao Liu, Jiabao An, Lixin Zhang, Yijin Su, and Kexin Xu. Digital human modeling and its applications: Review and future prospects. *Journal of X-ray Science and Technology*, 23:385–400, 2015.
- [ZBP+17] Andrea Zignoli, Francesco Biral, Barbara Pellegrini, Azim Jinha, Walter Herzog, and Federico Schena. An optimal control solution to the predictive dynamics of cycling. Sport Sciences for Health, 13:381–393, 2017.
- [Zhe19] Yu Zheng. Computing the best grasp in a discrete point set with wrench-oriented grasp quality measures. *Autonomous Robots*, 43:1041–1062, 2019.
- [ZHZ⁺20] Simon Zimmermann, Ghazal Hakimifard, Miguel Zamora, Roi Poranne, and Stelian Coros. A multi-level optimization framework for simultaneous grasping and motion planning. *IEEE Robotics and Automation Letters*, 5:2966–2972, 2020.
- [ZQ06] Yu Zheng and Wen Han Qian. Limiting and minimizing the contact forces in multifingered grasping. *Mechanism and Machine Theory*, 41:1243–1257, 2006.
- [ZW03] Xiangyang Zhu and Jun Wang. Synthesis of force-closure grasps on 3-d objects based on the q distance. *IEEE Transactions on Robotics and Automation*, 19:669–679, 2003.
- [ZXZ⁺20] Baohua Zhang, Yuanxin Xie, Jun Zhou, Kai Wang, and Zhen Zhang. State-of-the-art robotic grippers, grasping and control strategies, as well as their applications in agricultural robots: A review. Computers and Electronics in Agriculture, 177:105694, 2020.